UNIVERSIDADE DO VALE DO PARAÍBA
INSTITUTO DE PESQUISA E DESENVOLVIMENTO
PROGRAMA DE PÓS-GRADUAÇÃO EM FÍSICA E ASTRONOMIA

Paulo Fabrício Macário

Evaluation of Mechanical, Spectroscopic, and Morphological Properties of DLC Coatings with TiO2 Integration via PECVD and ALD on 316L Stainless Steel for Applications in UV Radiation-Prone and Saline Environments

Avaliação das Propriedades Mecânicas, Espectroscópicas e Morfológicas de Revestimentos DLC com Integração de TiO2 via PECVD e ALD em Aço Inoxidável 316L para Aplicações em Ambientes Propensos à Radiação UV e com Salinidade

São José dos Campos – SP
2024

Paulo Fabrício Macário

Evaluation of Mechanical, Spectroscopic, and Morphological Properties of DLC Coatings with TiO2 Integration via PECVD and ALD on 316L Stainless Steel for Applications in UV Radiation-Prone and Saline Environments

Thesis presented to the Graduate Program in Physics and Astronomy at the Research and Development Institute of the University of Vale do Paraíba, in partial fulfillment of the requirements for the degree of Doctor in Physics and Astronomy.

Advisor: Prof. Dr. Lúcia Vieira.

São José dos Campos – SP
2024

Fundação Valeparaibana de Ensino

BIBLIOTECA

TERMO DE AUTORIZAÇÃO DE DIVULGAÇÃO DA OBRA

Ficha catalográfica

Macário, Paulo Fabrício
Evaluation of Mechanical, Spectroscopic, and Morphological Properties of DLC Coatings with TiO2 Integration via PECVD and ALD on 316L Stainless Steel for Applications in UV Radiation-Prone and Saline Environments / Paulo Fabrício Macário; orientador, Lúcia Vieira. - São José dos Campos, SP, 2024.
112 p.

Tese (Doutorado) - Universidade do Vale do Paraíba, São José dos Campos. Programa de Pós-Graduação em Física e Astronomia.

Inclui referências

1. Física e Astronomia. 2. diamond-like carbon (DLC). 3. titanium dioxide (TiO2). 4. saline environment. 5. UV radiation-prone environments. I. Vieira, Lúcia, orient. II. Universidade do Vale do Paraíba. Programa de Pós-Graduação em Física e Astronomia. III. Título.

Eu, Paulo Fabrício Macário, autor(a) da obra acima referenciada:

Autorizo a divulgação total ou parcial da obra impressa, digital ou fixada em outro tipo de mídia, bem como, a sua reprodução total ou parcial, devendo o usuário da reprodução atribuir os créditos ao autor da obra, citando a fonte.

Declaro, para todos os fins e efeitos de direito, que o Trabalho foi elaborado respeitando os princípios da moral e da ética e não violou qualquer direito de propriedade intelectual sob pena de responder civil, criminal, ética e profissionalmente por meus atos.

São José dos Campos, 3 de Outubro de 2024.

Autor(a) da Obra

Data da defesa: 08 / 08 / 2024

Universidade do Vale do Paraíba

Instituto de Pesquisa e Desenvolvimento

PAULO FABRÍCIO MACÁRIO

"Evaluation of Mechanical Spectroscopic and Morphological Properties of DLC Coatings with TiO_2 integration via PECVD and ALD on 316L Stainless Steel for Applications in UV Radiation Prone and Saline Environments".

Tese aprovada como requisito parcial à obtenção do grau de Doutor, do Programa de Pós-Graduação em Física e Astronomia, do Instituto de Pesquisa e Desenvolvimento da Universidade do Vale do Paraíba, São José dos Campos, SP, pela seguinte banca examinadora:

Prof.ª Dr.ª Virginia Klausner de Oliveira	Virginia K. de Oliveira
Prof.ª Dr.ª Lucia Vieira	Lucia Vieira
Prof. Dr. Irapuan Rodrigues de Oliveira Filho	Irapuan R. de O. Filho
Prof. Dr. Cesar Aguzzoli- UCS	Cesar Aguzzoli
Prof. Dr. Newton Kiyoshi Fukumasu - USP	Newton K. Fukumasu

Prof.ª Dr.ª Juliana Ferreira Strixino

Diretora do IP&D – Univap

São José dos Campos, 08 de agosto de 2024.

ACKNOWLEDGMENTS

I would like to express my deepest gratitude to my wife and daughter for their unwavering support and encouragement throughout this journey. I am immensely grateful to my advisor, Dr. Lúcia Vieira, for her invaluable guidance and mentorship. Special thanks go to my colleagues and friends at the Nanotecplasma Laboratory, particularly Alessandro and Dr. Carolina Hahn, for their collaboration and camaraderie. I also want to thank Patrícia and Natália from the Graphene and Nanotechnology Research Laboratory (MackGraphe) at Universidade Presbiteriana Mackenzie for their assistance with the UVA tests and RAMAN characterizations.

My sincere appreciation goes to Dr. Angela Vieira and Dr. Lucas Manfroi for their help and support during the PECVD and ALD depositions. I am grateful to MSc. Priscila for her assistance with SEM and EDS characterizations and analyses. I also want to extend my thanks to Dr. André Ricardo Marcondes for his help in conducting the nano hardness tests, and to Dr. Gislene Martins for her support with the optical profilometry equipment for roughness analysis. Lastly, I would like to thank Prof. Dr. Francisco das Chagas Marques for his continuous support and assistance at Unicamp and in conducting the contact profilometry tests.

I am deeply grateful to the *Coordenação de Aperfeiçoamento de Pessoal de Nível Superior* (CAPES) for the scholarship and financial support. I also extend my heartfelt thanks to the *Universidade do Vale do Paraíba (Univap)* for all the support, equipment's, laboratories and personnel provided.

I am also thankful to all those who have assisted me along the way but whom I may not have mentioned by name. Your contributions, no matter how small, were vital to the completion of this thesis.

To everyone who played a part in this work, your support and encouragement were essential, and I am deeply appreciative. Thank you.

RESUMO

Este estudo apresenta uma abordagem inovadora de revestimento duplo, integrando carbono tipo diamante (DLC) com dióxido de titânio (TiO_2) em aço inoxidável 316L. A combinação de DLC depositado por *Plasma Enhanced Chemical Vapor Deposition* (PECVD) e TiO_2 depositado por *Atomic Layer Deposition* (ALD) visa preservar as propriedades tribológicas inerentes do DLC enquanto mitiga a degradação induzida por radiação UV. Aproveitando a capacidade do TiO_2 de absorver, refletir e dispersar a luz UV, esta estratégia de dupla camada melhorou, de forma significa, a durabilidade dos revestimentos de DLC em ambientes propensos à radiação UV. Os efeitos do envelhecimento acelerado por exposição UV em filmes de DLC e DLC/TiO_2 foram avaliados usando o equipamento QUV *Accelerated Weathering Tester*. O teste de spray salino e o teste de Ferroxyl foram empregados para verificar a resistência à corrosão e a permeabilidade do filme. Análises abrangentes foram realizadas para avaliar as propriedades estruturais e mecânicas antes e depois da exposição UV, incluindo espectroscopia Raman, perfilometria, MEV, EDS, nanoindentação e tribometria. Os resultados demonstram que a camada de TiO_2 mitiga efetivamente os danos induzidos por UV, preservando a integridade e o desempenho tribológico do filme de DLC mesmo após 408 horas de envelhecimento UV. Especificamente, os revestimentos de DLC/TiO_2 mantiveram menor rugosidade, maior dureza e melhor adesão do que os revestimentos apenas de DLC sob condições idênticas. Além disso, os testes em condições atmosféricas marinhas mostraram que os filmes revestidos com DLC e DLC/TiO_2 exibiram alta resistência à corrosão em comparação com o aço inoxidável 316L não revestido, mantendo a integridade do revestimento mesmo sob exposição prolongada a ambiente adverso. Esta pesquisa avança significativamente a tecnologia de revestimentos protetores, melhorando a durabilidade e o desempenho dos filmes de DLC, particularmente nas indústrias aeroespacial e outras indústrias exigentes onde a exposição à radiação UV é uma preocupação crítica.

Palavras-chave: carbono tipo diamante (DLC); ambiente salino; dióxido de titânio (TiO_2); ambientes propensos à radiação UV.

ABSTRACT

This study presents an innovative dual-layer coating approach integrating titanium dioxide (TiO_2) onto diamond-like carbon (DLC)-coated 316L stainless steel. The combination of PECVD-deposited DLC and ALD-deposited TiO_2 aims to preserve the inherent tribological properties of DLC while mitigating UV-induced degradation. By leveraging the ability of TiO_2 to absorb, reflect, and scatter UV light, this dual-layer strategy significantly enhances the durability of DLC coatings in radiation-prone environments. The effects of accelerated aging through UV exposure on DLC and DLC/TiO_2 films were evaluated using an Accelerated Weathering Tester. The Salt Spray test, and Ferroxyl test were employed to verify corrosion resistance, and film's permeability. Comprehensive analyses were conducted to assess the structural and mechanical properties before and after UV exposure, including Raman spectroscopy, profilometry, SEM, EDS, nanoindentation, and tribometry. The results demonstrate that the TiO_2 layer effectively mitigates UV-induced damage, preserving the DLC film's integrity and tribological performance even after 408 h of UV aging. Specifically, the DLC/TiO_2 coatings maintained lower roughness, higher hardness, and better adhesion than DLC-only coatings under identical conditions. Additionally, the films' behavior in marine atmospheric conditions showed that the DLC and DLC/TiO_2-coated films exhibited significantly enhanced corrosion resistance compared to the bare 316L stainless steel, maintaining the integrity of the coating even under prolonged exposure to adverse environments. This research significantly advances protective coating technology by enhancing the durability and performance of DLC films, particularly in aerospace and other demanding industries where exposure to UV radiation is a critical concern.

Keywords: diamond-like carbon (DLC); saline environment; titanium dioxide (TiO_2); UV radiation-prone environments.

LIST OF ILLUSTRATIONS

LIST OF TABLES

LIST OF ABBREVIATIONS AND SYMBOLS

a-C	Amorphous Carbon
a-C:H	Amorphous Hydrogenated Carbon
ALD	Atomic Layer Deposition
ASTM	American Society for Testing and Materials
CAPES	*Coordenação de Aperfeiçoamento de Pessoal de Nível Superior*
CCD	Charge-Coupled Device
DLC	Diamond-like carbon
ECR	Electron Cyclotron Resonance
EDS	Energy Dispersive Spectroscopy
FWHM	Full Width at Half Maximum
HF	Hydrofluoric Acid
IBAD	Ion Beam Assisted Deposition
ID/IG	Intensity Ratio of D to G Bands
INPE	*Instituto Nacional de Pesquisas Espaciais*
IP&D	*Instituto de Pesquisa e Desenvolvimento*
PECVD	Plasma Enhanced Chemical Vapor Deposition
R.F	Radio Frequency
Ra	Roughness Average
Rq	Root Mean Square Roughness
SEM	Scanning Electron Microscopy
ta-C	Tetrahedral Amorphous Carbon
ta-C:H	Tetrahedral Amorphous Hydrogenated Carbon
TiO_2	Titanium Dioxide
Univap	*Universidade do Vale do Paraíba*
UV	Ultraviolet
UVR	Ultraviolet Radiation

TABLE OF CONTENTS

1 INTRODUCTION

Diamond-like carbon (DLC) is renowned for its exceptional hardness and resistance [1], but it is not impervious to challenges. Vulnerabilities may arise in environments characterized by ultraviolet radiation, high altitude, exposure to atomic oxygen, and wide temperature ranges, such as those encountered in high atmospheres or space [2,3,4]. Understanding these challenges is crucial when designing materials for radiation-prone environments, as radiation can cause structural damage to DLC [5].This is especially true in environments with high radiation doses, where it can lead to hydrogen loss, changes in the concentration of sp^3 and sp^2 bonded sites, alterations in bond angle disorder, and other effects [6]. These changes compromise the tribological properties of DLC, reducing its wear resistance and increasing friction. The adhesion of DLC to the underlying surface may also be compromised, potentially leading to its flaking or delamination.

Radiation interference can increase wear in scenarios where DLC is a lubricating coating. Additionally, radiation can further induce the formation of structural defects, such as gaps and vacancies in the DLC network, altering its hardness and toughness and increasing roughness [6]. This heightened roughness may render the surface more susceptible to wear and fracture, reducing effectiveness in applications where a smooth surface is crucial [2].

Mitigation strategies, such as using protective layers similar to TiO_2, can help preserve DLC properties and enhance its robustness [7]. When applied as an additional layer over DLC, TiO_2 plays a significant role in mitigating the effects of ultraviolet radiation [8,9]. This combination creates a more resilient system, preserving the structural integrity of the coating even under prolonged exposure to UV radiation, thereby reducing the direct impact on DLC. This protection was attributed to the absorption properties of TiO_2 within the UV spectrum [10], which helps to prevent direct damage to the DLC. It also offers protection against undesirable chemical reactions induced by radiation and enhances tribological properties, providing an additional layer of protection against wear and corrosion [9,11,12], contributed to the overall durability and resistance of the composite coating.

There are many ways to deposit DLC films. However, given the specific requirements of the study at hand, PECVD is particularly advantageous for depositing high-quality DLC coatings. This technique excels in depositing coatings at relatively low temperatures, with precise control over the coating composition and properties [13,14]. Additionally, PECVD is well-suited for depositing coatings in large areas, providing a practical solution for the diverse requirements of emerging markets [14,15].

In this context, the combination of PECVD and ALD techniques aims to preserve the inherent tribological properties of DLC while achieving highly uniform, adherent, and conformal dual-layer coatings. This research delves into the synergistic effects of DLC and TiO_2, aiming to provide insights into the structural and tribological responses of this composite coating under challenging conditions. By elucidating the vulnerabilities of DLC in UV environments and assessing how TiO_2 can serve as a mitigating agent, the work aims to significantly contribute to the advancement of protective coatings with enhanced durability, particularly in aerospace and other demanding industries.

Furthermore, the behavior of the DLC/TiO_2 composite coating was also examined in marine atmospheric conditions. Given the harsh nature of marine environments, which are characterized by high salinity and humidity, resistance to corrosion becomes a critical factor for many applications. Salt spray tests and porosity assessments were employed to evaluate the coating's performance in these conditions. By examining the protective efficacy of the DLC and TiO_2 layers against salt-induced corrosion, the research aims to enhance the longevity and reliability of DLC coatings even in marine environment applications, broadening insights into their applicability.

Moreover, these findings have significant implications for specific applications, particularly in the deployment of high-altitude drones operating above 60,000 feet [16], especially when hovering over ocean areas. In such environments, prolonged exposure to UV radiation and corrosive marine conditions presents considerable challenges [17]. The enhanced durability and UV resistance offered by the DLC/TiO_2 coatings could greatly benefit these drones, which are constantly exposed to intense UV radiation and extreme temperature fluctuations, making the protection of critical components essential. Additionally, the improved corrosion resistance and durability of the DLC/TiO_2 coatings can be advantageous for offshore operations, such as those in the oil and gas industry,

where equipment is regularly subjected to harsh marine environments[1,18]. These results broaden the potential applications of DLC/TiO_2 composite coatings, making them valuable assets not only in aerospace and high-altitude operations but also in maritime and offshore industries[19], where the protection and performance of vital components in demanding conditions are critical.

2 OBJECTIVES

This study aims to verify the effectiveness of using TiO_2 as an overlayer on DLC film to improve its resistance to ultraviolet radiation degradation and to assess its behavior in marine atmospheric conditions.

2.1 SPECIFIC OBJECTIVES

To accomplish the primary objective, several specific goals have been delineated. These aims are centered on optimizing the deposition processes for both DLC and TiO_2 films, ensuring the quality and performance of the combined coating, and assessing its effectiveness under harsh environmental conditions. The specific objectives are as follows:

- Establish PECVD deposition parameters that result in a film with low roughness, high hardness, high homogeneity, good substrate adhesion, and low porosity.
- Establish ALD deposition parameters to obtain a thin film over the DLC coating with high adhesion, low roughness, high homogeneity, low porosity, and minimal impact on the properties of the DLC film.
- Test the effectiveness of the DLC/TiO_2 film in increasing the UV radiation resistance of the DLC film and compare its behavior in a saline atmosphere environment.

2.2 EXPECTED RESULTS

Some expected results include increased resistance to UV radiation and enhanced durability of the dual-layer film in saline environments, attributed to the addition of the TiO_2 layer.

3 LITERATURE REVIEW

For this work, industry consensus standards, government regulations, and major research databases were consulted, including Scopus, Web of Science, SciELO, PubMed, IEEE Xplore, Google Scholar, ScienceDirect, JSTOR, SpringerLink, Wiley Online Library, ProQuest, and the ACM Digital Library. The goal was to find relevant, current, and authoritative articles, documents, and publications related to the topics developed in this study.

3.1 CARBON STRUCTURES

The carbon atom can arrange itself in three different hybridizations: sp^3, sp^2, and sp^1, allowing it to form a wide variety of structures with both crystalline and disordered characteristics [20]. It is truly remarkable for its extraordinary ability of catenation to combine with itself and other chemical elements in different ways and thereby form the basis of organic chemistry [21].

For example, graphite is formed by a series of sp^2 bonded carbon forming planes, consisting of stacked parallel layers. In this structure, each carbon atom is bonded to three others, forming a series of continuous hexagons. The bonding between the three atoms in the same plane is covalent, short in length, and highly resistant. The fourth possible bond is formed with another electron from an adjacent plane through a van der Waals bond, which has lower energy compared to the covalent bond [22].

When pure, graphite is chemically very inert, making it highly resistant to most degrading and corrosive elements. However, there is always some degree of impurity, which results in increased chemical reactivity [22].

Another possible structure is DLC, characterized by being a non-crystalline, metastable formation of carbon that does not exhibit long-range order. It may have some regions with medium or short-range ordered structures and contains a significant fraction of sp^3 bonds. This provides DLC with strength and hardness characteristics close to those of diamond due to its tetrahedral-type structure [20].

Diamond, by far the material with the greatest known hardness, has a well-defined tetrahedral crystalline structure. Each diamond tetrahedron combines with four other tetrahedrons, forming three-dimensional, entirely covalent crystalline structures. These structures can have cubic or hexagonal symmetry, with the former being the most common and stable. Due to its high molar density compared to other materials, diamond is the stiffest, hardest, and least compressible of all substances [22].

In addition to sp^3 and sp^2, carbon can also form sp^1 hybridized bonds. This type of hybridization is less common but can be observed in molecules like acetylene (C_2H_2), where carbon atoms form a linear structure with a triple bond. The linear geometry results from the overlap of one sp hybrid orbital with another, forming a sigma (σ) bond, while the remaining two *p* orbitals form two pi (π) bonds.

Table 1 highlights a comparison among the properties of graphite, DLC, and diamond, such as hardness, electrical conductivity, thermal conductivity, and chemical reactivity. This table serves as a quick reference for understanding the distinct characteristics of these materials [21,22,23,24,25].

Table 1 – Properties of graphite, DLC, and diamond.

Property	**Graphite**	**Diamond**	**DLC**
Hardness	Low	Very High	High
Electrical Conductivity	High	Insulator	Variable
Thermal Conductivity	High	Very High	Moderate
Chemical Reactivity	Low (Pure)	Low	Low

For example, Graphite is widely used as a lubricant and in batteries due to its electrical conductivity [26]. DLC's exceptional hardness and low friction make it ideal for protective coatings in the medical and automotive industries. Diamond, with its unparalleled hardness and thermal conductivity, is essential in cutting tools and high-performance electronic devices.

DLC has a variable electrical conductivity, which is a function of hydrogen content. It may not be a suitable semiconductor material since it has a relatively low bandgap, generally low resistivity, and low operating temperature, although semiconducting properties have been reported [22,23].

3.2 DLC FILMS

DLC films have been extensively employed across numerous industries because of their superior attributes as protective layers for mechanical parts. The wide range of applications of this material type stems from its remarkable properties, such as low friction, high wear resistance, chemical inertness, nano-smoothness, and even antibacterial properties [27,28,29].

These films have been deposited using a variety of methods, often diverging from the DLC regions depicted in the ternary diagrams for sp^3 covalent carbon, sp^2 covalent carbon, and hydrogen content [30]. The allotropy of carbon enables the creation of a wide range of multi-atomic crystalline and amorphous structures with varying contents based on the types of hybridizations present (sp, sp^2, and sp^3) [13]. In detail, sp^3 hybridization involves the mixing of one *s* orbital and three *p* orbitals, leading to a tetrahedral structure where carbon atoms form four strong covalent bonds. This hybridization confers many of the beneficial properties of diamond itself, such high hardness, chemical and electrochemical inertness [20]. On the other hand, sp^2 hybridization occurs when one *s* orbital and two *p* orbitals combine, resulting in a trigonal planar structure with carbon atoms bonded in flat sheets[20,21], as seen in graphite. Materials with sp^2 hybridization exhibit good electrical conductivity due to the delocalized electrons in the structure. Lastly, sp hybridization involves the mixing of one *s* orbital and one *p* orbital, creating a linear structure where carbon atoms form two strong bonds [20,22]. This type of hybridization is typical in compounds like acetylene and contributes to distinct chemical reactivity. Figure 1 shows the ternary diagram illustrating the possible types of carbon films based on the concentrations of sp^2 bonds, sp^3 bonds, and the amount of hydrogen present in the composition and the three forms of carbon hybridization.

Similarly, the range of disordered carbons is extensive, encompassing coal, carbon fibers, glassy carbon, and evaporated amorphous carbon, which primarily feature sp^2 type bonds [31]. Amorphous carbon (a-C) and hydrogenated amorphous carbon (a-C:H), which are mechanically hard, infrared-transparent, and chemically inert, have portions of their bonds in the sp^3 configuration [31,32]. Their beneficial properties arise precisely from the sp^3 component of their bonds.

Figure 1 – Ternary phase diagram featuring various types of carbon films and representation of sp^1, sp^2, and sp^3 hybridizations.

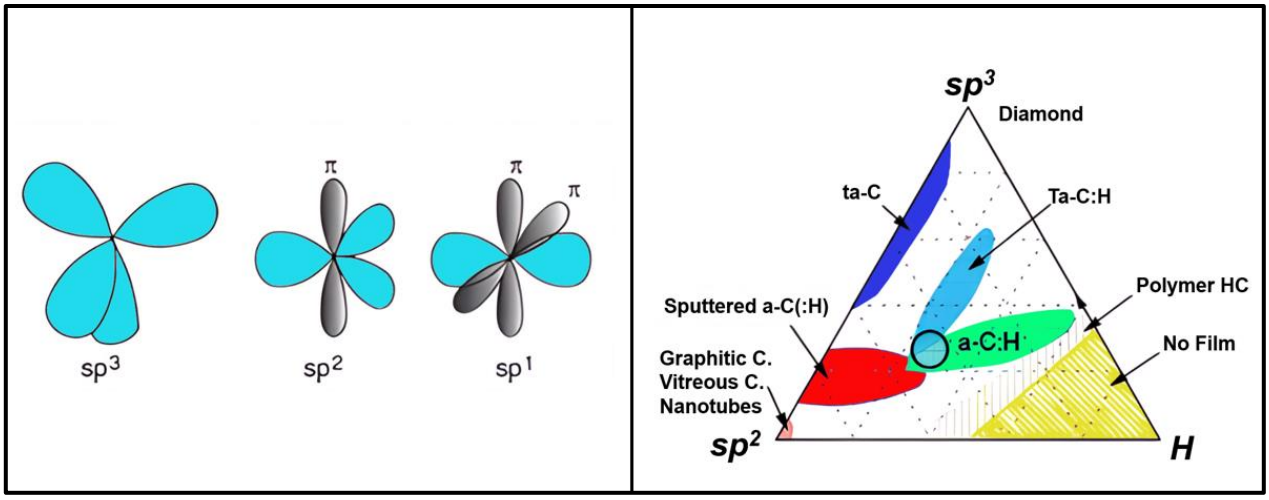

Source: Adapted from Robertson [20].

In general, these carbons can be entirely amorphous or contain crystalline inclusions [31] and are distinguished by their tribological properties [33]. DLC is not as good an optical material as single crystal diamond but, it has many advantages as a thin coating and is satisfactory in many applications [22].

The hydrogen content is the primary independent variable which determines the structure, and hence the properties of the DLC. It is possible to classify DLC films according to their hydrogen content and the variation in the ratio of sp^3 (diamond-like carbon) to sp^2 (graphite-like carbon) bonds. Generally, a-C films have a hydrogen content between 20 and 60% and up to 40% of the sp^3 C–C phase [13] and the atomic percent hydrogen is very low in the non-hydrogenated DLC, nominally less than one atomic percent. The compressive stress level in hydrogenated DLC increases with increasing hydrogen content [34].

The sp^2 hybridized atoms present in the amorphous network of DLC films control electronic properties such as band gap distance. Meanwhile, atoms with sp^3 hybridization govern mechanical aspects, tribological properties, and corrosion resistance [35]. The sp^3/sp^2 ratio in DLC films is primarily responsible for regulating their overall performance, including mechanical properties, tribological characteristics, and corrosion performance in various aggressive environments [35].

These coatings also have some limitations that hinder their broader application, such as low thermal stability and dependence on sliding environment or adhesion strength. As the ambient temperature rises, these coatings undergo a transformation in their sp^2 configuration, where existing olefinic bonds become aromatic [29,36]. Additionally, a reduction in hardness and sp^3 fraction, along with an increase in wear rate, has been reported in parallel with temperature increase [29,37].

DLC converts to graphite at a relatively lower temperature. An initial transformation has been observed starting at 250°C. The transformation occurs rapidly at 400°C, driven by hydrogen loss followed by graphitization. The maximum long-term operating temperature for DLC is between 250 and 300°C [22].

The sliding environment has been noted to significantly affect the surface chemistry of these films, with substantial differences reported in the coefficient of friction (COF) between dry and wet environments, as well as between coatings deposited with hydrogenated and non-hydrogenated precursors [29]. In essence, non-hydrogenated DLC coatings exhibit a higher friction coefficient compared to hydrogenated DLC coatings in inert environments due to the absence of hydrogen, which results in a lack of passivation on the surface [38]. In an inert environment, where external species are unavailable to interact with the surface, fresh C–C bonds are exposed during sliding, leading to increased adhesion and a higher COF. On the other hand, hydrogenated DLC coatings have surface hydrogen atoms that reduce the formation of these C–C bonds, thus leading to a lower COF. This effect is primarily driven by tribo-chemical interactions between the solid surfaces, where the presence of hydrogen plays a crucial role. The hydrogen-bonded molecules on the surface of hydrogenated DLC coatings inhibit the formation of C–C bonds at the friction interface, resulting in weaker surface contacts and significantly reducing wear. Additionally, carbon atoms terminated with hydrogen, including di-hydrated carbon atoms, which have two hydrogen atoms bonded to them, further enhance passivation on the DLC surface. This higher degree of passivation is one of the key factors contributing to the super-lubricity of hydrogenated DLC coatings [38,39].

However, under ambient conditions, the friction coefficient of hydrogenated DLC coatings decreases, while that of non-hydrogenated DLC coatings significantly increases. This is because, at high operating temperatures and humidity levels, chemical reactions

occur, and water molecules are absorbed onto the surface, leading to the formation of tribo-chemical layers such as C–O–O, C–O, and C–OH bonds. These layers reduce friction in non-hydrogenated DLC. Conversely, in hydrogenated DLC, the presence of water molecules, under ambient conditions, increases hydrogen bonds forces, providing slide graphite layer around the contact area, resulting in an decrease in the friction coefficient [40,41]. The DLC-coated surface interactions for different sliding situations are schematically represented in Figure 2.

Figure 2 – Schematic of tribological performance of H-free and H-DLC coatings as a function of humidity and temperature.

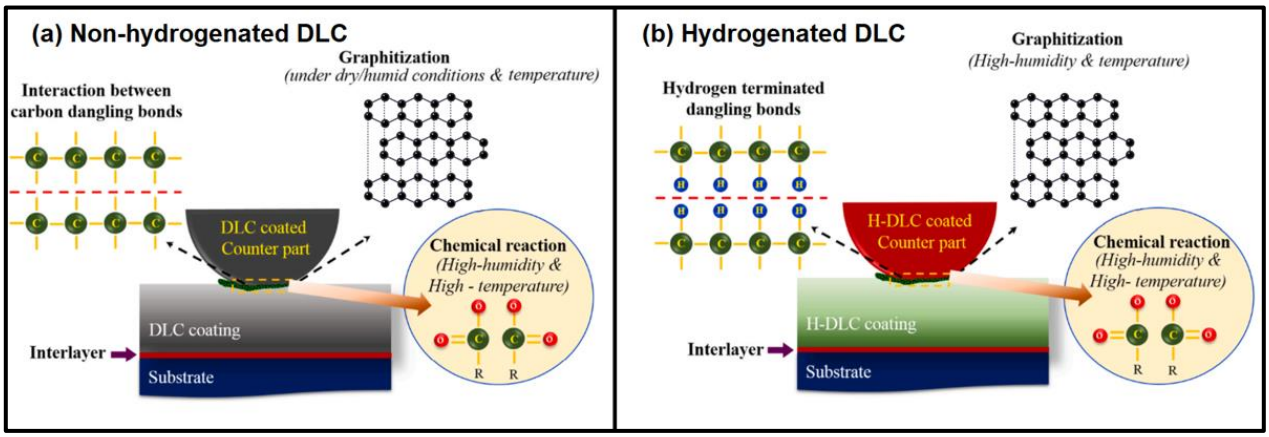

Source: Adapted from O. Sharifahmadian *et al.* [42]

The high residual stress in DLC results in low adhesion force between the film and the substrate. The use of interlayers or doping with heterogeneous elements can modify the microstructure and properties of DLC to better suit the application environment [43,44].

According to J. C. Sánchez-López and A. Fernández [45], the use of a gradual transition from metal to ceramic and then to DLC is a way to improve the stress caused by residual tension and enhance adhesion. The interlayer provides a thermal expansion coefficient gradient that reduces tensile and compressive stress on the films and improves the adhesion of the coating on the substrate.

Doping elements can reduce residual stress and improve DLC coating properties. Figure 3 illustrates a representation of typical doping elements that can be added to DLC to achieve enhanced properties.

Elements such as nitrogen (N) and silicon (Si) can improve thermal stability [18,29]. Si doping can also significantly alter the microstructure of DLC films. In hydrogenated DLC films, Si–C bonds are considerably longer than C–C bonds, which allows Si-doped DLC films to accommodate greater structural disorder [46], thereby increasing the likelihood of sp^3 carbon bond formation. As silicon content in the DLC coating increases, the average size of sp^2-bonded clusters decreases, and the fraction of sp^3 carbon bonds rises [47]. However, due to the increased density of voids at higher Si concentrations, the hardness of Si-DLC coatings may be reduced. Conversely, Si-DLC films exhibit significantly lower internal stress compared to pure DLC films, owing to the relaxation of highly distorted bond angles [48,49].

Figure 3 – DLC doping elements scheme.

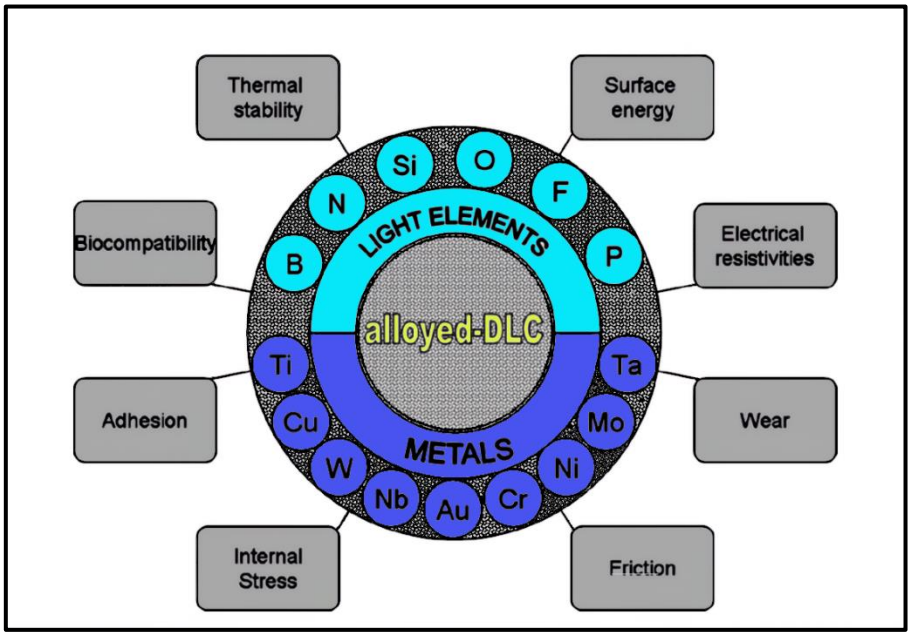

Source: Adapted from J. C. Sánchez-López and A. Fernández [45].

The use of nitrogen as a dopant in DLC coatings change its structure by forming strong bonds such as C–N, C–N–C, and C=N [50,51], which favors formation of sp^2 carbon hybridization and subsequently reduces sp^3 carbon bonding [52,53,54]. The hardness of the DLC coating can be reduced by doping nitrogen into the carbon matrix

[55], and it improves the toughness and coating adhesion to the substrate, resulting in higher stability in the tribological behavior of the DLC coating [42].

B. Zhou *et al.* [56] reported that Cu doping increases the size, ordering and content of the sp^2 -C clusters for Cu-DLC composite films. High DC current led to the decrease of the size and ordering degree of carbon clusters (whether sp^2 -C or sp^3 -C) due to intense collision of Cu with carbon particles and high mobility of carbon atoms on the substrate and the Cu doping can reduce the roughness of DLC films under certain fabrication conditions. Additionally, Cu can also be an effective way to reduce residual internal stress into the DLC structure [57] by forming ductile phases with can improve the toughness of the coating, [58] and enhance corrosion resistance [18].

The incorporation of Ti can reduce residual stresses, improve adhesion, and enhance mechanical properties [18]. Aluminum in DLC films containing hydrogen can reduce residual stress and improve film tribological performance [43].

Fluorine-doped DLC coatings significantly impact the structure of DLC. Due to fluorine's high electronegativity, it forms only single bonds with carbon, which does not prevent the formation of –C=C– bonds. Additionally, the C–F bonds formed can shorten the chains and rings within the DLC structure by extending out of the carbon network [59]. This reduces the amount of sp^3 carbon hybridizations, with $–CF_2$ and $–CF_3$ groups forming within the network [60]. This reduction in sp^3 carbon hybridizations also leads to a decrease in the ratio of hydrogenated carbon compounds, subsequently lowering the sp^3/sp^2 ratio, as well as Young’s modulus and hardness. Despite these changes in mechanical properties, fluorine has a notable effect on reducing the surface energy of DLC coatings by decreasing residual stress and improving adhesion strength [42].

3.3 DLC DEPOSITION PROCESSES

There are several deposition methods to produce DLC coatings. Among the most commonly employed are Physical Vapor Deposition (PVD), Chemical Vapor Deposition (CVD) and Plasma-Enhanced Chemical Vapor Deposition (PECVD) [1,61,62]. PVD techniques, which include sputtering, plasma beam source, pulsed filtered cathodic vacuum arc deposition (PFCVAD) and cathodic vacuum arc, among others [13,63], are

renowned for producing high-quality coatings with superior mechanical and tribological performance [61,64]. However, these techniques necessitate high vacuum environments and elevated temperatures, potentially limiting their applicability to certain substrates and complex geometries [61,65].

The CVD methods are widely used for the deposition of DLC films due to their ability to produce high-quality coatings with specific properties. However, they typically require higher substrate temperatures (often above 600°C) compared to other methods, which limit the range of substrates that can be coated. The high temperatures required for CVD processes can lead to increased energy consumption and longer processing times, making the process costly and less energy-efficient compared to lower-temperature PECVD methods. Examples of CVD processes include atmospheric pressure chemical vapor deposition (APCVD), low-pressure chemical vapor deposition (LPCVD), thermal evaporation, laser ablation, and many others [63,66].

In contrast, PECVD offers significant advantages, such as lower deposition temperatures and the capability to coat complex shapes, making it more suitable for a broader range of applications, including those involving flexible and temperature-sensitive substrates [13]. PECVD processes also allow the incorporation of various dopants to fine-tune the properties of DLC coatings, enhancing attributes such as wear resistance, biocompatibility, and corrosion resistance [61,64,65].

Beyond these conventional methods, several non-conventional techniques are gaining traction, driven by the need to meet new market demands in areas such as electronics, biomedical applications, additive manufacturing, and textiles. These techniques, including micro-plasma, dielectric-barrier-discharge (DBD), and electrospray-assisted plasma jet coating, facilitate low-temperature deposition, localized coating, and the ability to coat complex and internal surfaces [61,64].

For example, DBD systems can effectively coat the inner surfaces of narrow tubes, which is challenging with conventional PVD methods. Furthermore, these non-conventional approaches offer scalability for large-area deposition and the integration of nanomaterials for enhanced surface functionalities [61].

Given the specific requirements of this study, PECVD is particularly advantageous. This technique excels in depositing high-quality DLC coatings at relatively low

temperatures, allowing for the growth of films without altering the microstructure of the substrates [63]. It also provides precise control over the coating composition and properties through the use of different precursors and process parameters [13,14]. PECVD can operate at relatively lower temperatures compared to other deposition processes, which further supports the integrity of the substrate microstructure [63]. Moreover, PECVD is well-suited for depositing coatings over large areas, making it a practical solution for the diverse needs of emerging markets [14,15]. With advancements in PECVD, such as high-density plasmas including electron cyclotron resonance (ECR) and inductively coupled plasma (ICP), it is now possible to produce denser a-C:Hs type films, known as highly tetrahedral hydrogenated amorphous carbon or ta-C:H [31,67]. These high-density plasmas are achieved at lower pressures than conventional PECVD and use magnetic fields to extend electron paths, resulting in high plasma ionization.

While traditional PECVD requires vacuum conditions, innovations like Atmospheric Pressure PECVD (AP-PECVD) have enabled operations at atmospheric pressures, further simplifying the process and reducing costs. These advancements make PECVD a cost-effective and versatile method for producing high-performance DLC coatings [61,68]. As conventional PECVD processes improve, the domains of a-C:H and ta-C:H begin to merge, enhancing the versatility and application potential of PECVD.

3.4 OPTIMIZATION OF DEPOSITION PARAMETERS AND THEIR INFLUENCE ON DLC FILM PROPERTIES VIA THE PECVD METHOD

In general, the properties of a-C:H films deposited using the PECVD technique depend on process parameters such as pressure, bias voltage, temperature, and the composition and chemical nature of precursor gases [13,66]. It is necessary to control these deposition parameters and, in general, predict the influence of each parameter on the properties of the deposited coating. The non-linear behavior and the need to perform a large number of experiments make this process challenging [13].

One of the problems that can occur with this type of coating is the lack of adhesion of the DLC film, which results from an incompatibility of mechanical characteristics and thermal expansion coefficients between the film and the substrate due to the high level of

internal residual stress [14]. Consequently, the higher intrinsic stresses of DLC films are one of the contributing factors to their limited use in aggressive environments [63].

Good adhesion is fundamental to achieving greater film durability, and limitations generally occur due to high residual compressive stress in the film's microstructure, inherent to the deposition process [3,33]. The literature reports that the incorporation of an amorphous silicon interlayer improves the adhesion between the substrate surface and DLC coatings on metal substrates [13]. Additionally, adhesion can also be associated with preparatory factors that precede the film deposition process, such as cleaning, surface roughness, and impurities [69].

The corrosion stability of the DLC film can be improved by increasing the thickness of the coating film [14]. One possible method is to produce multilayer DLC films, which increase film thickness and improve the renucleation of the coating [35]. The interfaces can add different desirable properties to the film and reduce the porosity and continuity of the pores, thus preventing aggressive environmental media from contacting the substrate [63].

The type of molecular structure formed by the film also depends on the energy provided to the ions contained in the plasma and the free path between these ions and the substrate. Therefore, it is important to control the power source (self-bias voltage), the current used for plasma generation, the background pressure, and the partial pressures of the precursor gases. These parameters influence the processes of dehydrogenation, ion subimplantation, and chemical interactions involving neutral species.

According to Robertson [20], the subimplantation process induces a metastable increase in density, which helps the formation of sp^3 bonds.

3.5 INTRINSIC FACTORS AFFECTING DLC COATING DEPOSITION

In the deposition of DLC coatings, the physical processes of ion subimplantation, dehydrogenation, and chemical processes involving neutral species are critical factors in determining the type of carbon film that will be obtained [20]. According to Robertson [20], the dynamics of subimplantation provide a metastable increase in the density of the

affected region within a limited volume, allowing for the formation of sp^3 bonds located in the subsurface region.

During densification by subimplantation, ions from the incident beam, lacking the energy to penetrate the coating, stabilize on the surface through sp^2 bonds. Ion beams with sufficiently high energy to pass through the coating surface settle in interstitial voids, increasing local atomic density and promoting the formation of sp^3 bonds. Ions that do not contribute to densification, due to insufficient energy to occupy interstitial spaces, assist in increasing the deposition rate through relaxation processes [20]. Direct penetration, indirect penetration through recoil atoms from the surface, and relaxation of the densified region can be better understood through Figure 4.

Figure 4 – Schematic diagram of the basic subimplantation process.

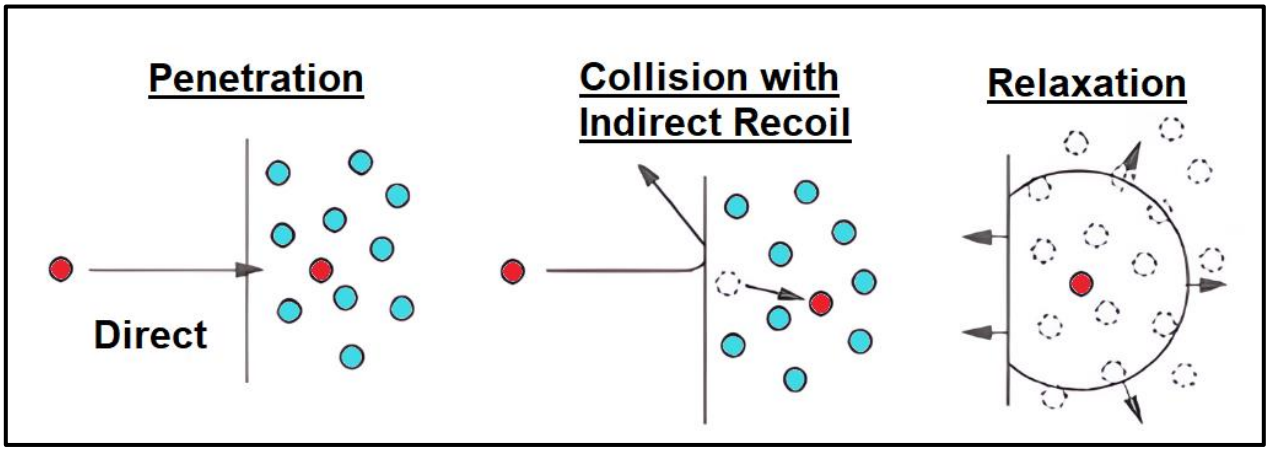

Source: Adapted from Robertson [20].

The coating growth rate is balanced by the equilibrium established between the angle of incidence and the energy of the incident ion beams, which will dictate whether the deposition rate will be greater than the removal rate, as both processes occur simultaneously [70,71].

3.6 TITANIUM DIOXIDE (TIO_2)

Titanium dioxide naturally occurs in three main crystallographic forms: anatase (tetragonal), rutile (tetragonal), and brookite (orthorhombic) [72,73]. The most stable form

of TiO_2 is rutile. However, all three forms can be synthesized in the laboratory. Anatase (metastable) and brookite (unstable) transform into thermodynamically stable rutile when subjected to calcination processes at temperatures above 600°C [72,74]. This transformation does not have a single temperature, and the involved processes have not been fully described to date [9]. The brookite crystalline phase requires special conditions, which limits its use in applications [75]. Thus, anatase and rutile forms have been more widely used and studied.

TiO_2 is a semiconductor with various interesting characteristics and properties, such as its photocatalytic effect and UV radiation blocking capability. It is biocompatible and has chemically stable properties [8]. It is low-cost, non-toxic, and abundant in nature. TiO_2 can be used as a solid lubricant [76], but its broad usage is in photocatalytic reactions, as a UV radiation blocker; in contaminated water treatment, in the decomposition of organic pollutants; in biomedicine, for the photocatalytic inactivation of pathogenic bacteria; in the energy sector, in dye-sensitized solar cells as a semiconductor material due to its semiconductor characteristics, among other applications.

TiO_2 photoactivation occurs in the range of 300 to 388 nm [12,77]. Both anatase-rutile (A-R) phases absorb wavelengths in the ultraviolet region [77], with different UV absorption and reflection capacities due to differences in electronic structure, with energy band gaps of 3.00 eV for rutile and 3.23 eV for anatase. The rutile phase can absorb wavelengths slightly closer to the visible light region [77], while the anatase phase has the best combination of photoactivity and photostability [12].

To further enhance the photoelectric properties of TiO_2 and extend its activation into the visible light spectrum, various modifications have been explored. Studies have demonstrated that doping TiO_2 films with metal and non-metal elements can significantly improve photocatalytic activity. Metal dopants function as electron traps at the semiconductor interface, helping to reduce electron-hole recombination, while non-metal dopants replace oxygen atoms in the TiO_2 lattice, enhancing light absorption in the visible spectrum. Additionally, non-metal doping has been shown to increase the thermal stability of the anatase phase. These modifications, along with careful control of several critical parameters, play a crucial role in optimizing the overall photocatalytic performance of TiO_2 thin films [78].

Table 2 presents a summary of the main properties of the anatase and rutile crystallographic forms of TiO_2.

Table 2 – Main Properties of Anatase and Rutile Crystallographic Forms of TiO_2.

Properties	Anatase	Rutile
Crystal Structure	Tetragonal	Tetragonal
Atoms per Unit Cell	4	2
Unit Cell Volume (nm^3)	0.1363	0.0624
Lattice Parameters (nm)	a = 0.3785 c = 0.9514	a = 0.4594 c = 0.29589
Density (kg m^{-3})	3894	4250
Hardness (Mohs)	5.5 - 6	6 – 6.5
Refractive Index	2.49/2.54	2.790/2.903
Solubility in HF	Soluble	Insoluble
Solubility in H_2O	Insoluble	Insoluble
Bulk Modulus (GPa)	183	206
Band Gap (Experimental)	3.2	3.0

Source: Adapted from Hanaor, Dorian A.H. & Sorrell, Charles C.[9]

3.7 TIO_2 DEPOSITION TECHNIQUES

Various deposition techniques have been developed to produce TiO_2 coatings, each with its own set of advantages and challenges. For example, sputtering is a widely used physical vapor deposition technique that offers high adhesion and good control over film thickness and composition. However, it requires sophisticated equipment and can potentially damage the DLC film due to high-energy ion bombardment [10,68]. In addition, sputtering presents other challenges, particularly in producing TiO_2 coatings with the correct stoichiometry. Reactive sputtering, which involves the introduction of oxygen, can lead to non-stoichiometric films that affect the desired optical and photocatalytic properties. The control of the TiO_2 crystalline phase (e.g., anatase or rutile) is also critical, as it influences the film's functional properties, yet it requires precise tuning of deposition conditions such as substrate temperature and power. Another significant challenge is managing the internal stress within the deposited films, which can cause cracking or delamination, particularly in thicker layers [78,79].

Chemical Vapor Deposition (CVD) is known for producing uniform films with excellent adhesion, capable of covering complex geometries. It is extensively used in the microelectronics industry. Nevertheless, CVD processes often require high temperatures [14], which limits their application to temperature-sensitive substrates. Furthermore, the use of hazardous precursor gases raises safety concerns and complicates the deposition process. Achieving uniformity over large areas and controlling the growth rate can also be challenging in CVD processes, especially in industrial-scale applications.

Sol-gel techniques are cost-effective, making them suitable for large-area coatings and complex shapes. However, this process may result in films with porosity or cracks, involve long curing times, and require high-temperature annealing to achieve the desired crystalline phases [80].

In contrast to these methods, Atomic Layer Deposition (ALD) stands out for its ability to produce high-quality, uniform thin films with exceptional precision. One of the key advantages of ALD is its capacity to deposit films at relatively low temperatures, making it particularly advantageous for temperature-sensitive materials. This method's self-limiting nature ensures controlled growth for each layer, resulting in excellent film uniformity that is pinhole-free, with controllable thickness and reproducibility [81]. ALD enables atomic-level control over film thickness and composition, ensuring high conformity even on substrates with complex geometries [82,83].

3.8 ATOMIC LAYER DEPOSITION

ALD is an advanced technique that enables the deposition of thin films in layers of individual atoms with thickness control at the Angstrom scale (Å). This method ensures high quality, high uniformity, and efficient control over chemical composition, unwanted impurity contamination, and the stacking of each deposited layer. However, the production volume is limited and low, making it unsuitable for products requiring large-scale production [84,85].

In the ALD process, selected reactive gases are sequentially introduced into a reaction chamber. The core principle of the ALD process involves the self-saturation of available bonds on the exposed surface with a reactive material, allowing for the

sequential deposition of layers of the same or different compositions. Once the available surface bonds are filled, the reaction ceases with surface saturation. An inert gas purge, such as nitrogen, is then performed to remove possible reaction products and any excess reactant molecules from the chamber [85].

Subsequently, the second reactant is introduced, which reacts with the first reactant until all available sites on the substrate have reacted, followed by another purge. By repeating this cycle, the desired product molecules are deposited layer by layer onto the substrate surface until the desired thickness is achieved [85].

3.9 APPLICATIONS OF DLC AND TIO_2 COATINGS

There are numerous potential applications for the combination of DLC and TiO_2 across various fields due to their unique physicochemical properties. Particularly for DLC, its resistance to corrosion, wear, and chemical inertness makes it a potential material for applications in the healthcare sector, such as the manufacturing of prostheses, implants, and tools, whose coatings inhibit the proliferation of pathogens while being biocompatible.

In this context, an interesting article by Nikolas De Meurechy [86], published in 2022, presents a study on temporomandibular joint (TMJ) prostheses. These prostheses were partially coated with diamond-like carbon, and their wear resistance and performance parameters were evaluated. The wear resistance was deemed acceptable, and a significant improvement was observed in the smoothness of the condylar surface, resulting in reduced friction and improved sliding of one surface over another. Additionally, a study on the protein biofilm formation mechanism on DLC-Ag coatings for joint implant applications elucidates the biofilm formation mechanism at the friction interface with the coating [87].

In the field of engineering, there are numerous applications in aerospace, oil and gas, tribology, machining, and cutting tools. A recent article proposes the use of super-hard DLC coatings as an alternative to polycrystalline diamond for cutting tools, typically employed in high-speed cutting tools for lightweight materials with high mechanical strength [88]. Another approach to utilizing DLC coatings was explored by Leal [89], who conducted a study with promising results for the use of tungsten doped DLC thin films as

piezoresistive sensing materials for the development of measurement and control sensors. This has potential applications across a wide range of sectors, including automotive, aerospace, industrial, and biomedical industries.

In the same way, a study by Zhang *et al.* [90] demonstrated the potential of Ti-doped DLC coatings, specifically Ti/TiN/TiCN/Ti-DLC composite films, for enhancing both wear and corrosion resistance, especially in harsh marine environments. Using medium-frequency magnetron sputtering, these coatings were applied to 316L stainless steel, significantly improving its performance. Tribological tests revealed that the coatings reduced friction and wear, with friction coefficients ranging from 0.24 to 0.32, far superior to untreated 316L stainless steel. Additionally, electrochemical testing showed that the multilayer structure of Ti-DLC films provided excellent corrosion resistance, with a substantial reduction in current density under passivation conditions, particularly at a substrate bias voltage of −120V. The introduction of titanium elements contributed to both the mechanical and chemical stability of the films, making them particularly promising for both aerospace and marine environments.

In line with DLC and TiO_2 applications, research conducted by Wicher *et al.* [91] presents results on the deposition of DLC films on glass substrates using the cathodic sputtering method with gas injection. The studies demonstrated that varying the proportions of Ne-Argon (Ne-Ar) gases during pulsed injections promoted the synthesis of DLC films with a significant sp^3 (C–C) phase content, reaching up to 45% with 40% Ne gas injections. This increase in the sp^3 fraction resulted in a 25% gain in hardness and crack resistance, making these films promising for applications in nanomechanical systems. Additionally, to minimize the parasitic reflectance of sp^2 (C=C) domains, thin layers of titanium dioxide (TiO_2) were deposited on the DLC, resulting in an anti-reflective effect and increased visible and infrared transmittance, reaching up to 87%. These results highlight the potential of DLC/TiO_2 bilayer structures to enhance the durability of glass in harsh environments, with broad applications in functional coatings.

Regardless DLC is a potential tribological material for aerospace use [3,92], there is no validated data to date showing that any lubricants and solid coatings alone can meet the tribological conditions of space [76]. For example, under high vacuum conditions, DLC coatings have been reported to often adhere and form cold welding with the contacting

counterpart, resulting in a high coefficient of friction, especially for films with low or no hydrogen content [25,38,93,94]. Atomic oxygen (AO) also poses a problem for DLC, as it degrades by reacting with AO to form CO or CO_2, as explained by J. Rao, K.J. Lawson, and J.R. Nicholls [4].

In this context, incorporating an additional TiO_2 layer over the DLC film can provide several advantages. TiO_2 may protect the underlying DLC layer from the detrimental effects of ultraviolet radiation since the TiO_2 absorption wavelength is located in the UV region [10], thereby reducing the direct impact on DLC. This effect is attributable to the absorption properties of TiO_2 within the UV spectrum, which helps to prevent direct damage to DLC. It also offers protection against undesirable chemical reactions induced by radiation and enhances tribological properties, providing an additional layer of protection against wear and corrosion [9,11,12].

Radiation interference can increase wear in scenarios where DLC is a lubricating coating. Additionally, radiation can further induce the formation of structural defects, such as gaps and vacancies in the DLC network, altering its hardness and toughness and increasing roughness [6]. This heightened roughness may render the surface more susceptible to wear and fracture, reducing effectiveness in applications where a smooth surface is essential [2].

This absorption not only prevents the degradation of the DLC structure but also helps maintain its tribological properties by reducing hydrogen loss and preserving the sp^3 and sp^2 hybridized carbon sites. Additionally, TiO_2 acts as a barrier against atomic oxygen, which is prevalent in low Earth orbit environments. The interaction between TiO_2 and atomic oxygen primarily results in the formation of titanium oxides, which do not degrade the DLC layer underneath. Furthermore, TiO_2's high hardness and chemical stability contribute to the overall durability and wear resistance of the composite coating, making it more suitable for the harsh conditions of space. By enhancing the structural integrity and resilience of DLC films, TiO_2 coatings extend the operational lifespan and reliability of components in aerospace applications.

Thus, researchers have made significant strides in exploring the potential properties and applications of DLC coatings in feasible engineering and market

applications. Current DLC coatings are increasingly meeting the stringent application requirements of advanced multipurpose systems [95].

3.10 CHARACTERIZATION OF DLC AND TIO_2 BY RAMAN SPECTROSCOPY

The Raman effect, first predicted by Smekal in 1923 and later experimentally confirmed by Raman in 1928 [96], is a photonic technique that delivers structural and chemical insights about materials. This method does not require any sample preparation, making it a highly effective and non-destructive approach for the structural characterization of carbon films.

In this process, a laser with a certain power emits photons that travel through a series of mirrors, lenses, and filters before colliding with the sample in a collimated manner. The scattered radiation is then directed to a high-resolution spectrometer and finally to a CCD camera or detector, where the signal from the sample is captured [97].

It is a widely used characterization technique for any carbon compound. According to Ferrari and Robertson [98], all carbon compounds exhibit common features in their Raman spectra in the region between 800 and 2000 cm^{-1} of Raman shift. By identifying the peaks at 1360 and 1560 cm^{-1}, corresponding to the D and G bands, respectively, one can obtain the ratio of intensities I_D/I_G, which indicates the degree of disorder. This can be described within a three-stage model of increasing disorder, as illustrated in Figure 5.

Thus, we can observe that graphite has an ordered, crystalline structure with predominantly sp^2 bonds. As the structure of graphite begins to change, moving from stage 1 towards stage 2, the crystalline clusters rearrange into a nanocrystalline structure. As it approaches stage 2, the structure continues to transform until the entire crystalline structure becomes amorphous. This process is called the amorphization trajectory, where the structure transforms from graphite to diamond.

Figure 6 shows the relationship between the G-band position and the ratio of intensities I_D/I_G during the stages of the amorphization trajectory. At the position of 1580 cm^{-1}, the structure is purely graphite, exhibiting an ordered, crystalline structure with sp^2 bonds, without the presence of sp^3 hybridization.

Figure 5 – Three Stages of Increasing Disorder Amorphization.

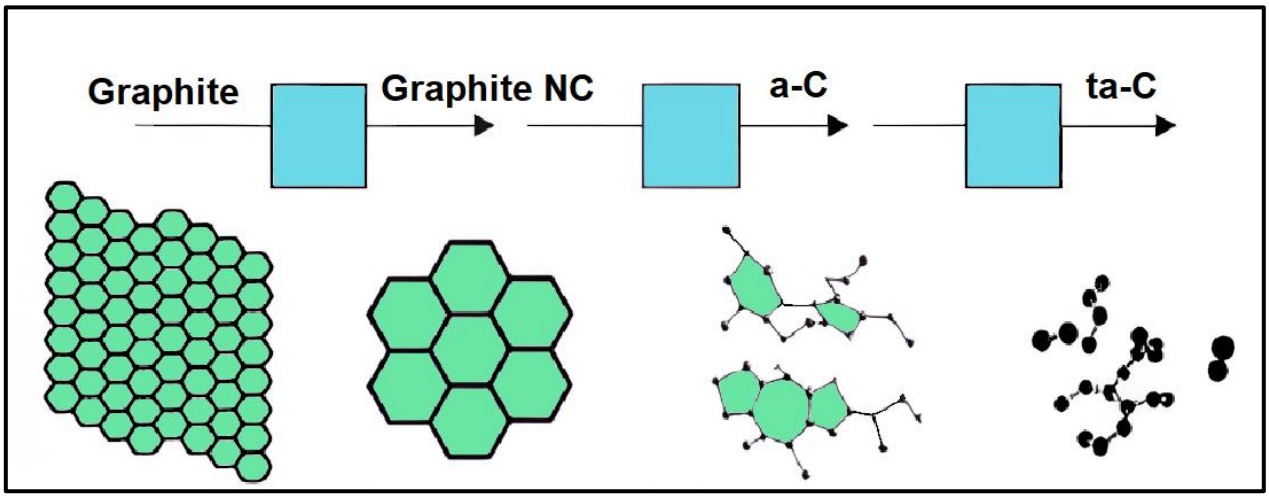

Source: Adapted from Ferrari & Robertson [98,99]

As the trajectory progresses towards ordering, the I_D/I_G ratio reaches its highest value (two) at the beginning of stage 2, when the crystalline structure transforms into nanographite. From this point, the structure progressively transitions from crystalline to amorphous, leading to the formation of clusters with sp^3 bonds. The percentage of sp^3 bonds increases relative to sp^2 bonds as it approaches the end of stage 2. At a G band position of approximately 1515 cm^{-1}, the sp^3 bond content is around 20%, resulting in a carbon coating with an a-C structure.

In stage 3, the structure continues to become more amorphous, increasing the percentage of sp^3 bonds until the G band position reaches 1515 cm^{-1} and the sp^3 bond content is around 85%. At this point, the structure is designated as ta-C. Thus, it is possible to determine the type of coating formed by examining the positions of the D and G bands and the I_D/I_G ratio.

In summary, Raman spectra fundamentally depend on four factors: (1) clustering of the sp^2 phase, (2) disorder in bond length and bond angle, (3) the presence of sp^2 hybridizations in rings or chains, and (4) the sp^2/sp^3 ratio. Combinations of these factors act as competing forces that shape the resulting Raman spectra [36].

Figure 7 provides a schematic illustration of the factors influencing the Raman G and D bands of DLC films when using either a 532 nm or 514 nm laser. Robertson J. outlined a method for obtaining detailed bonding structures of DLC films using different

laser wavelengths and identified specific polarizable and scattering sites crucial for Raman analysis [20].

Figure 6 – I_D/I_G Ratio in the amorphization trajectory and sp^3 bond fractions.

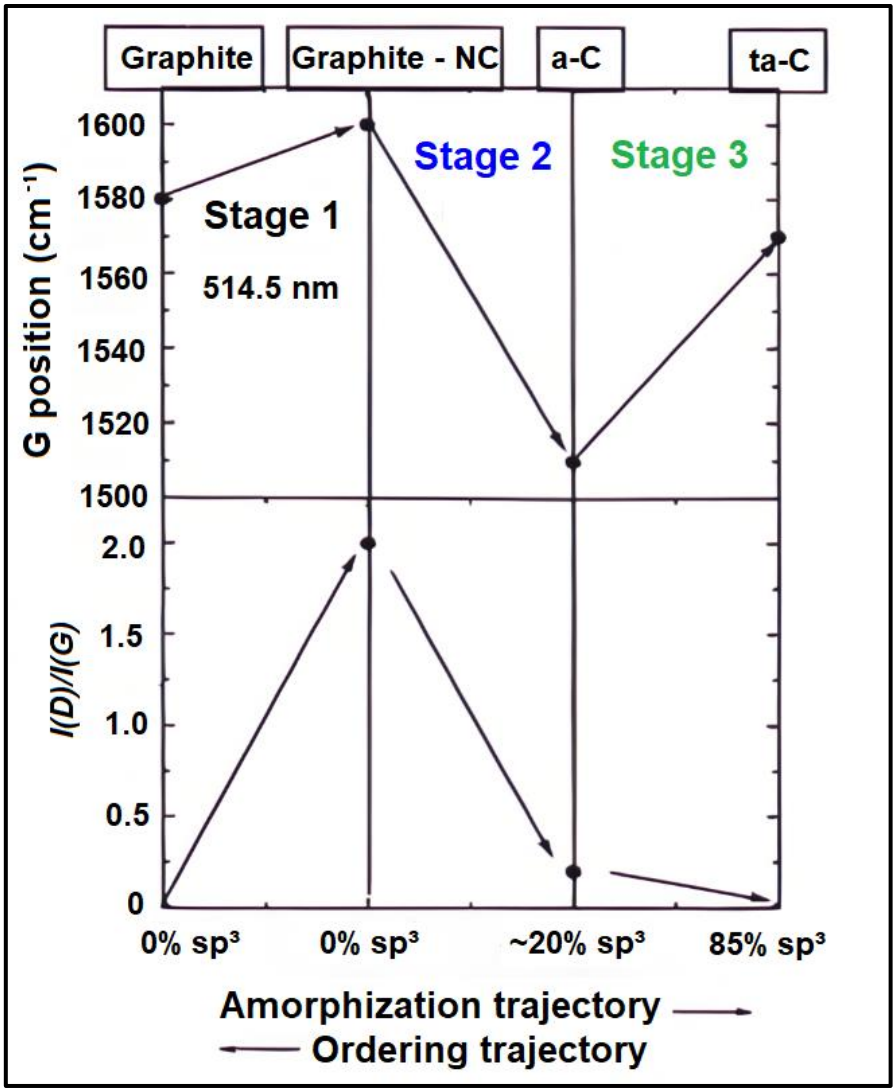

Source: Adapted from Ferrari & Robertson [98,99]

Raman spectroscopy has also proven to be an effective method for distinguishing between anatase and rutile [100]. The distinct Raman spectra of these titania polymorphs facilitate both qualitative and quantitative analyses with several notable advantages. Raman spectroscopy requires minimal or no sample preparation, is nondestructive, and allows for both local and broader phase analyses with a beam diameter of approximately

1 µm. Additionally, it offers mapping capabilities and rapid analysis, typically completed within one minute. Unlike X-ray diffraction (XRD), Raman spectroscopy does not suffer from preferred orientation effects, is more sensitive, and can detect nanoscale phases.

Figure 7 – Schematic plot of factors that affect the Raman G and D bands of DLC films using a laser of 532 nm or 514 nm.

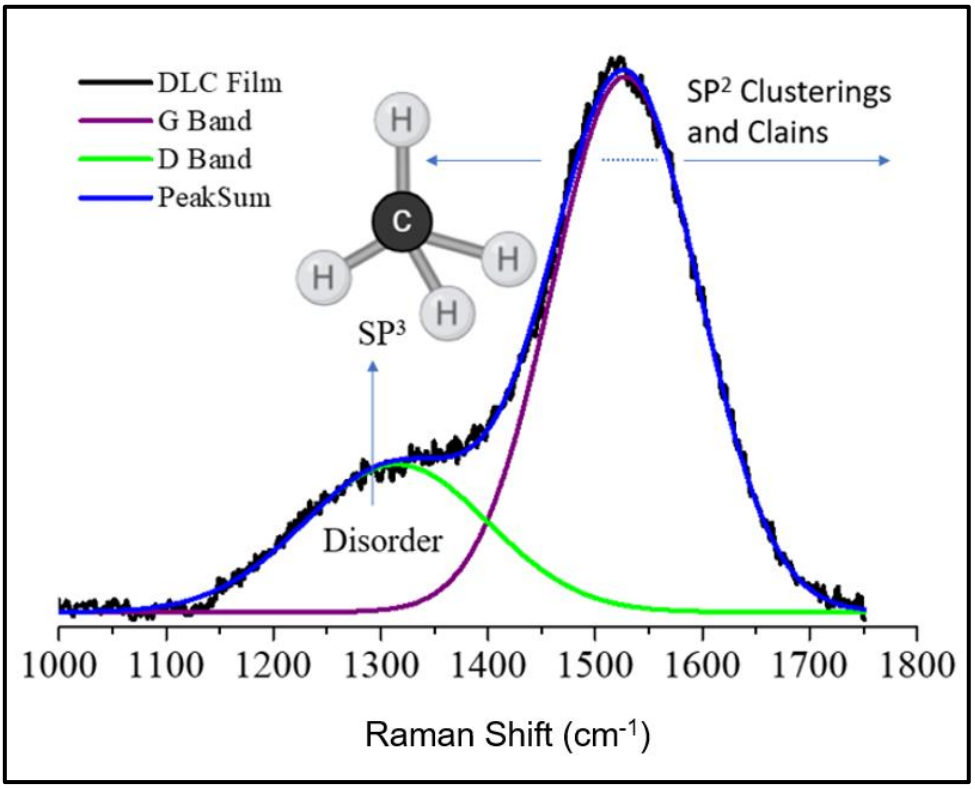

Source: Adapted from Ferrari & Robertson [101].

One of the key strengths of Raman spectroscopy lies in its effectiveness for analyzing nanoscale thin films. In contrast, glancing-angle XRD requires significant calibration, often produces diffuse peaks, and suffers from a background that makes it difficult to detect any amorphous phases. Raman spectroscopy avoids these issues, resulting in more efficient and sensitive analyses. Figure 8 presents the reference patterns and characteristic spectra of Raman modes for anatase and rutile phases.

The active characteristic Raman modes of the anatase phase of TiO_2 were observed at 143, 399, 519, and 639 cm^{-1}, while those of the rutile phase were detected at 250, 446, and 606 cm^{-1}. Furthermore, according to Zanatta [96], it is possible to

estimate the concentration of rutile or anatase phases in thin films by correlating the rutile concentrations with the Raman data obtained from the analysis of the specific phonon modes associated with each phase.

Figure 8 – Raman spectra of rutile and anatase powders.

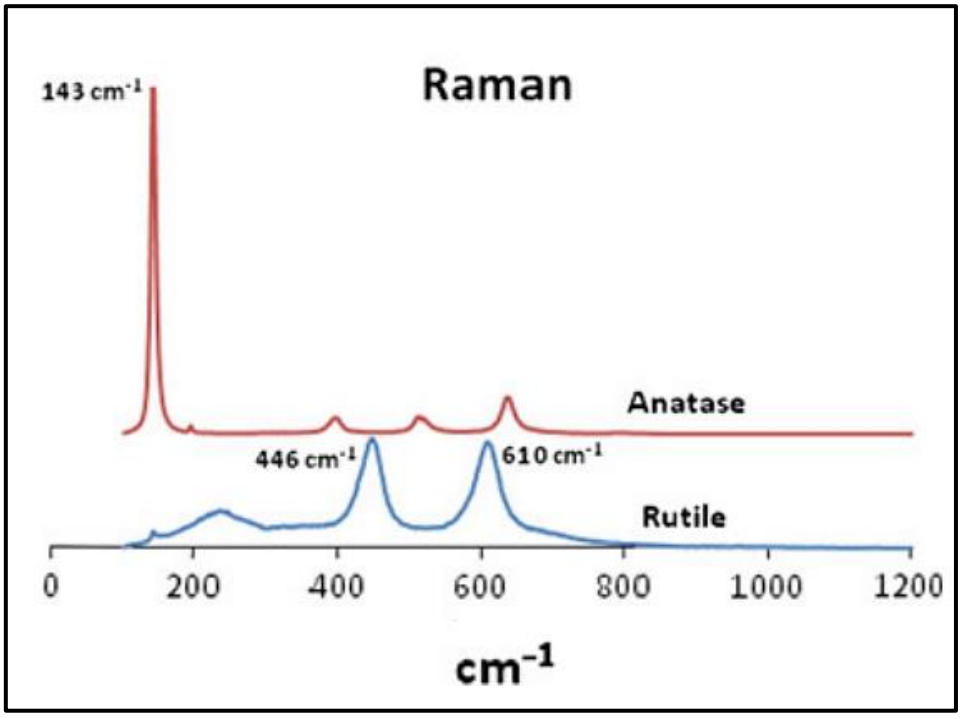

Source: Hanaor *et al.* [9].

3.11 FILM ADHERENCE EVALUATION

The scratch test is one of the methods that has been used to assess thin coating adhesion. In this test a diamond indenter is drawn across the coated surface under an increasing load (either stepwise or continuous) until at some load, a well-defined failure event occurs. The scratch test was developed to determine the adhesion strength and modes of mechanical failure of hard, thin ceramic coatings on metal and ceramic substrates at room temperature [102,103]. This test was not intended to measure the fundamental adhesion strength of the bond between the coating and the substrate, according to the method described in ASTM C1624-05, but to provide an engineering measure of the adhesion strength of the coating-substrate system. This measure of

adhesion is related to the interaction of the test device (tip geometry, loading rate, displacement rate, hardness, etc.) with the properties of the coating/substrate, such as hardness, fracture resistance, elastic modulus, and so forth [102].

Modes of failure are classified into two types: cohesive and adhesive. The cohesive mode is characterized by the film remaining intact along the entire scratch path without exposing the substrate, indicating good adhesion to the substrate. In the second case, when adhesion is poor, the substrate is exposed, and delamination failures occur in the perimeter regions of the scratch [104].

After conducting the tests, the loads required to initiate damage and cause the failure of the film were recorded, as well as the types of brittle failures and their classifications. However, it is not always easy to determine when this has occurred, and quantification of the failure mode may be difficult. For a hard coating on a softer substrate, spallation and buckling failure modes resulting from interfacial detachment were the most common, but a range of other cracks and deformed regions may also be observed. For hard coatings on hard substrates, the chipping observed in the scratch test is almost identical to the lateral fracture observed in the scratch testing of bulk ceramics [105].

There exists a specific range of coating and substrate properties where adhesion-related failures can be observed during scratch testing, which limits the applicability of this test for adhesion assessment across different coating-substrate systems. Generally, the scratch test is most effective for hard coatings on either soft or hard substrates where minimal plastic deformation of the coating occurs. However, when both the substrate and coating are hard, there is a tendency for the diamond stylus to wear during the test. Consequently, this method has been most widely applied to systems involving hard coatings on soft substrates[105].

3.12 FILM HARDNESS EVALUATION

Nanoindentation has been widely used to investigate mechanical properties of materials in sub-micro and nano-scale volumes, based on the analytical method proposed by Oliver and Pharr [106,107]. The two mechanical properties measured most frequently using load and depth sensing indentation techniques are the elastic modulus (E), and the

hardness (H). In a commonly used method, data is obtained from one complete cycle of loading and unloading. The unloading data is then analyzed according to a model for the deformation of an elastic half space by an elastic punch which relates the contact area at peak load to the elastic modulus. Methods for independently estimating the contact area from the indenter shape function are then used to provide separate measurements of E and H [106].

Estimations of bulk hardness from nanoindentation are frequently subject to considerable uncertainties due to indentation size effects (ISE), pileup effects, and potential influence of surface quality or test methods [107].

A primary challenge in nanoindentation studies is to bridge the gap between nano-scale and macro-scale hardness by developing accurate quantitative correlations between nanoindentation hardness and both Vickers hardness and tensile strength [107]. Experiments using a Berkovich indenter often show a pronounced depth dependence. This effect complicates the accurate estimation of bulk hardness.

In accordance with G. Pharr *et al* [108] the ISE is one of several size-dependent phenomena where smaller dimensions correlate with increased strength. Using geometrically self-similar indenters like cones and pyramids, this effect is evidenced by an increase in hardness as the depth of penetration decreases, becoming significant at depths less than approximately 1 μm. For spherical indenters, the sphere's diameter is the critical length scale; spheres with diameters smaller than approximately 100 μm yield measurably higher hardness values.

To enhance the quantitative correlation between nanoindentation hardness and macroscopic Vickers hardness and tensile strength, it is essential to investigate the impact of various experimental parameters and refine models. Although numerous mechanistic models for the ISE have been proposed, the most widely used model to explain experimental observations is that developed by Nix-Gao [109]. The Nix-Gao model, which accounts for the role of geometrically necessary dislocations (GNDs) in measured hardness, is frequently used to correct for the ISE and estimate the bulk equivalent hardness (H_o) from raw nanoindentation data using the classic equation below:

$$\frac{H}{H_0} = \sqrt{1 + \frac{h^*}{h}} \quad (1)$$

where H is the measured hardness, defined as the ratio of the load on the indenter normalized with respect to the projected contact area of the hardness impression, h is the indentation depth, and h* is the characteristic ISE length scale [107].

The Nix-Gao model improves the accuracy of hardness measurements by addressing the depth-dependence of hardness. This model is particularly useful for materials where the indentation depth is less than 1 μm, and it helps in quantifying the hardness by considering the contribution of GNDs, which become significant at small scales. By correcting for the ISE, the Nix-Gao model enables a more reliable estimation of bulk hardness from nanoindentation data [109].

In contrast, the Oliver-Pharr method focuses on analyzing the load-displacement curves obtained during indentation to derive both hardness and elastic modulus. This method involves calculating the contact area at peak load using an elastic punch model, which relates the indentation load and displacement to the mechanical properties of the material[106,108].

The method begins with the indentation process, where an indenter of known geometry (typically Berkovich or Vickers) is pressed into the material with a controlled load. The load and resulting displacement are continuously recorded, creating a load-displacement curve. This curve has two main parts: loading, where the indenter penetrates the material, and unloading, where it is withdrawn. The peak of this curve corresponds to the maximum load and penetration depth.

In accordance with Oliver-Pharr [106], the unloading portion of the curve is critical for determining the material's elastic properties. This segment is modeled using an elastic contact mechanics approach, fitting the unloading data to a power-law relationship to find stiffness (S) at the initial unloading point. This stiffness is used to calculate the contact depth (h_c), which is the depth of the indenter in contact with the material at peak load. The contact depth is determined using the formula $h_c = h_{max} - \epsilon \frac{P_{max}}{S}$, where h_{max} *is* the maximum displacement, P_{max} is the maximum load, and ϵ is a constant depending on the

indenter geometry. The projected contact area (A) at peak load is calculated based on the indenter's geometry and the contact depth. Hardness (H) is then calculated as $H = \frac{P_{max}}{A}$.

Finally, the reduced modulus (E_r) is derived from the contact stiffness and the projected contact area using the formula $E_r = \frac{\sqrt{\pi}}{2}\frac{S}{\sqrt{A}}$. The actual elastic modulus (E) of the material is then calculated by considering the elastic properties of both the indenter and the material through the relationship $\frac{1}{E_r} = \frac{1-\nu^2}{E} + \frac{1-\nu_i^2}{E_i}$, where ν and E are the Poisson's ratio and elastic modulus of the material, and ν_i and E_i are the Poisson's ratio and elastic modulus of the indenter.

This method is particularly advantageous for its ability to separately measure hardness and elastic modulus by using the shape function of the indenter to independently estimate the contact area. Furthermore, the Oliver-Pharr method is applicable to a wide range of materials, including both hard coatings on soft substrates and hard coatings on hard substrates. Its robustness and accuracy in determining mechanical properties from indentation data have led to its widespread adoption. However, challenges such as the potential wear of the diamond stylus during testing, especially for hard coatings on hard substrates, must be addressed. Despite these challenges, the Oliver-Pharr method remains a cornerstone in the field of nanoindentation due to its comprehensive approach to analyzing indentation data and deriving material properties.

In summary, while the Nix-Gao model provides a refined approach to account for size effects in hardness measurements by considering the role of geometrically necessary dislocations (GNDs), the Oliver-Pharr method offers a robust framework for determining hardness and elastic modulus from indentation data. Both methods complement each other and contribute significantly to the accurate characterization of mechanical properties at the nanoscale.

3.13 PASSIVE FILM AND CORROSION RESISTANCE

Passivity refers to the reduction in chemical reactivity exhibited by certain metals and alloys under specific conditions in certain environments. When this occurs, they behave like essentially inert metals and act as if they were noble metals such as platinum

and gold. This phenomenon is observed in commonly used engineering metals like iron, nickel, chromium, titanium, and alloys containing these materials.

The passivity of a metal can be disrupted by reducing agents, cathodic polarization, and halide ions, particularly chloride ions, which can penetrate the oxide layer or disperse it in a colloidal form, increasing its permeability. Metals or alloys containing chromium, aluminum, or stainless steel, which are typically passive in air, can have their passivity compromised by chloride ions at localized spots or areas. In the active-passive cell that forms, the anodic area is located at points where passivity has been breached. Since these areas are much smaller compared to the cathodic area, accelerated corrosion occurs at these points [110].

The main types of corrosion in stainless steels are intergranular corrosion, pitting corrosion, and stress corrosion. Specifically, 316 stainless steel tends to suffer from pitting corrosion in environments containing NaCl. Pitting corrosion in materials that form passive oxide films is one of the most concerning types of corrosion. This may occurs due to small surface defects, gaps, concentration differences, mechanical discontinuities, or microstructural phase heterogeneities, which make small regions of the metal surface more vulnerable and directly exposed to a reducing agent [111]. This type of corrosion is electrochemical in nature and causes localized severe attacks in the affected regions. Identifying corrosion points is not always possible through visual inspections. In such cases, the exposed region acts as the anode, the protected region as the cathode, and the corrosive medium as the electrolyte [112].

The corrosion rate and penetration rate of pitting corrosion tend to decrease with increasing pH, meaning that the corrosion rate and pitting penetration rate are proportional to the -log [H+] or pH value of the solution [113]. The more acidic the pH, the more pronounced the corrosion process.

According to Craig [114], one of the most commonly used parameters to describe a metal's resistance to pitting corrosion is the pitting potential (Ep). When the potential is more negative than Ep, the metal surface exhibits passivation, while more positive potentials than Ep result in pitting. Therefore, the more positive the pitting potential, the more resistant the metal is to this type of corrosion.

Figure 9 (a) illustrates the difference in Ep for various metals in a 3% NaCl solution at 30°C, and (b) shows a generic polarization curve for metals subject to passivation and pitting corrosion.

Figure 9 – Polarization Curves for Metals.

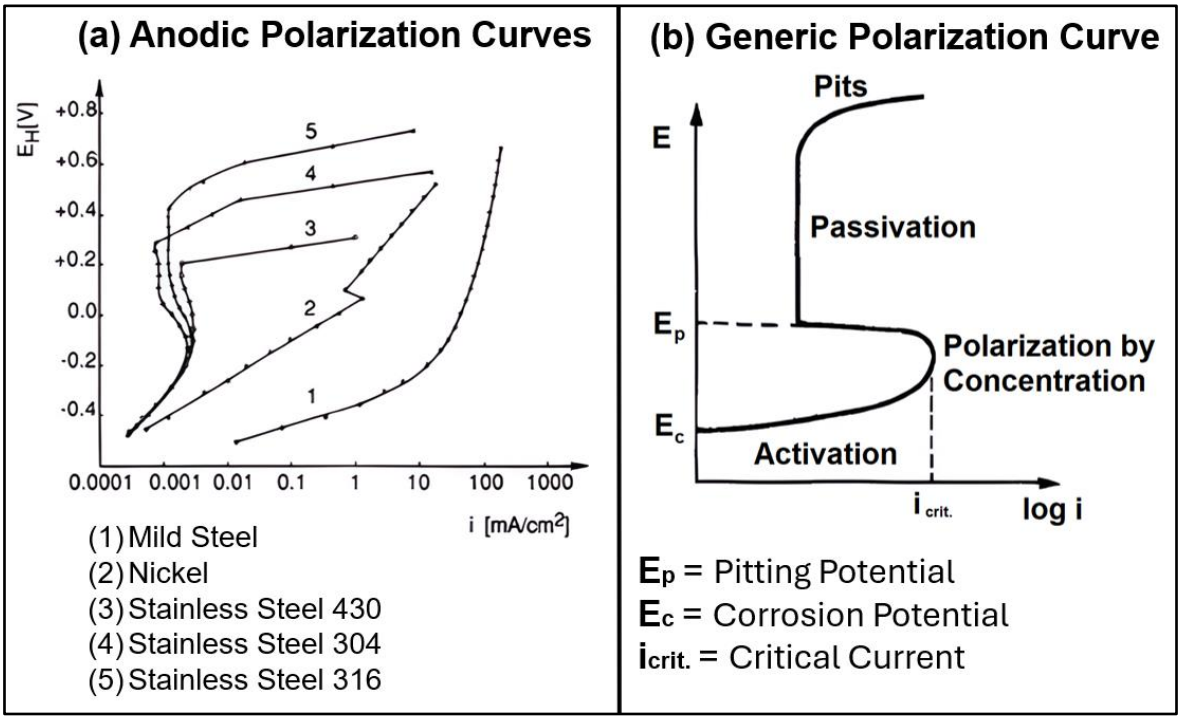

Source: Adapted from Craig [114] e Gentil [111]

It is important to note that the main difference between 316 and 316L stainless steel is the carbon content. 316L contains a lower amount of carbon compared to 316 (maximum of 0.03% versus 0.08% in 316), which makes it more resistant to sensitization, stress corrosion cracking, and intergranular corrosion, especially in corrosive environments [115]. Sensitization occurs when chromium carbides precipitate at grain boundaries during thermal exposure (typically between 450°C and 850°C), depleting the surrounding areas of chromium and thus reducing corrosion resistance. By having a lower carbon content, 316L stainless steel minimizes the formation of these carbides, maintaining its corrosion resistance [110].

This characteristic makes 316L a better choice for applications in marine environments, where resistance to chloride-induced corrosion is crucial. Chloride ions,

commonly found in seawater, can penetrate the passive oxide layer of stainless steel, leading to pitting and crevice corrosion. The lower carbon content in 316L helps preserve the integrity of the passive layer, providing better performance in these harsh conditions.

The chemical corrosion reaction between the solution of salt spray (typically a solution of sodium chloride, NaCl) and 316L stainless steel primarily involves the formation of iron oxides and other corrosion products.

The chloride ions (Cl^-) from the salt spray solution can penetrate the passive oxide layer (primarily chromium oxide, Cr_2O_3) that protects the stainless steel because they can concentrate in small pits and crevices. They disrupt the stability of the passive chromium oxide layer. Chloride ions can interact with the chromium oxide, leading to localized dissolution or breakdown of the protective layer, initiating pitting corrosion. These chloride ions can break down this passive layer, initiating localized corrosion. Once the passive layer is compromised, the underlying iron (Fe) in the steel can react with oxygen (O_2) and water (H_2O) in the environment. The general corrosion reaction for iron can be represented as $Fe + \frac{1}{2}O_2 + H_2O \rightarrow Fe(OH)_2$ [111]. This ferrous hydroxide ($Fe(OH)_2$) can further oxidize to form ferric hydroxide ($Fe(OH)_3$), which eventually dehydrates to form various iron oxides such as hematite (Fe_2O_3) or magnetite (Fe_3O_4).

According to Craig [114], the transition from pit nucleation to propagation is gradual, with several theories describing pit growth. One theory suggests that metal ion dissolution and hydrolysis in the pit depend on potential and pH, with a threshold potential below which passivation occurs and above which repassivation does not. Another theory posits that pit growth is mass-transfer-controlled, with ion diffusion rates dictating the growth rate. Additionally, there is significant support for pit growth via salt film formation, where the precipitation of a metallic salt film within the pit controls growth. The rate of metal cation transport through the salt film or its hydrated layer determines pit development, and repassivation can occur if enough water molecules reach the metal surface.

There is also susceptibility to stress corrosion cracking (SCC), which depends on the type of stainless steel. Ferritic stainless steels, for example, are significantly more resistant to SCC than austenitic stainless steels. The metallurgical conditions of the

material, such as hardness, work hardening, and the phases present, are often decisive factors. Cracks resulting from SCC can be intergranular or transgranular [114].

For this type of corrosion to occur, three basic conditions must coexist: tensile stresses, either from service or residual stresses resulting from work hardening, welding operations, or heat treatment; temperature, as SCC rarely occurs at temperatures below 60ºC; and the environment, specifically the presence of halide ions, with chloride (Cl^-) being the most common. Additionally, the presence of sodium hydroxide (NaOH) or hydrogen sulfide (H_2S) can cause SCC under conditions of high temperature and concentration.

Additionally, austenitic stainless steels can become susceptible to intergranular corrosion due to the precipitation of chromium-rich carbides. Among the materials most susceptible to this type of corrosion are stainless steels and aluminum alloys. Intergranular corrosion is a type of localized electrochemical corrosion that occurs at the grain boundaries of a metallic alloy. Its occurrence is often only detected when the component fails.

The precipitation process depletes the chromium content in the regions adjacent to the carbide, potentially reducing chromium levels to below 12%, thus losing its stainless characteristics. The formation of this chromium-depleted zone is known as sensitization, as it makes the material sensitive to intergranular corrosion. Because there is a significant difference in chromium content between the grain areas and the grain boundaries, an electrochemical cell is formed: grains act as the cathodic area (large area), and grain boundaries act as the anodic area (small area).

3.14 CORROSION RESISTANCE BY TIO_2

Titanium dioxide coatings, particularly when applied as a thin film, have shown significant promise in enhancing the corrosion resistance of metallic substrates. Research has consistently demonstrated that TiO_2 coatings act as an effective protective barrier against corrosive environments. For instance, Krishna *et al.* [116] showed that stainless steel exhibited significantly improved corrosion resistance when coated with TiO_2, highlighting the coating's effectiveness in industrial applications. Similarly, Shen *et*

al.[117,118] reported that TiO_2 nanoparticulate coatings applied via the sol-gel method on 316L stainless steel provided excellent corrosion protection by forming a uniform, stable layer that shields the steel surface from aggressive agents. Furthermore, Ohko *et al.* [119] demonstrated that TiO_2-coated stainless steel exhibited a cathodic photo-protection effect, reducing the corrosion rate under UV light exposure.

In addition, studies by Mohamoud *et al.* [120] revealed that weathering steel coated with TiO_2 exhibited higher resistance to sodium chloride (NaCl) aqueous solutions under UV illumination compared to uncoated steel. This photoprotective behavior is attributed to the semiconducting properties of TiO_2, which enable it to generate electron-hole pairs upon exposure to light, thereby reducing the electrochemical reactions responsible for corrosion.

These findings predominantly focus on rutile and anatase phases of TiO_2, which are known for their crystalline structures and stability. However, the potential of amorphous TiO_2 as a corrosion-resistant coating remains largely unexplored, representing an avenue for further research. Nevertheless, the ability of TiO_2 coatings, regardless of crystalline phase, to improve corrosion resistance through mechanisms such as barrier protection and photo-induced electron interactions underscores their relevance for applications in harsh environments, particularly where long-term durability and resistance to degradation are essential.

3.15 CORROSION RESISTANCE BY DLC

A Diamond-Like Carbon (DLC) coatings offer notable advantages in enhancing corrosion resistance [113,121,122], especially in harsh marine environments. The primary strength of DLC coatings lies in their ability to serve as an effective barrier, preventing corrosive agents such as saltwater, oxygen, and chloride ions from reaching the underlying substrate. The dense, amorphous carbon structure of DLC films creates a nearly impermeable layer that significantly reduces the penetration of moisture and corrosive substances, which are primary contributors to corrosion in marine settings [18,122].

In addition to their barrier properties, DLC coatings exhibit a high level of chemical inertness [30]. This chemical stability is crucial for protecting the underlying material from the aggressive chemical reactions typically found in marine environments. The inert nature of DLC ensures minimal interaction with the corrosive chemicals present in saltwater, thereby preserving the integrity of the substrate [30].

One of the defining characteristics of DLC coatings is their low permeability to gases and liquids. This trait is particularly important in marine applications, where limiting the ingress of water and oxygen is essential for minimizing corrosion. The amorphous structure of DLC contributes to this low permeability, effectively shielding the substrate from corrosive elements.

The hardness and wear resistance of DLC coatings further enhance their effectiveness in corrosive environments. The coatings' high hardness helps them withstand mechanical wear and abrasion, which can otherwise lead to localized corrosion. By maintaining the coating's integrity and protecting the underlying substrate, DLC coatings help ensure long-term durability and performance.

Moreover, DLC coatings can possess anti-fouling properties, reducing the accumulation of marine organisms on the coated surfaces. While this is not a direct form of corrosion resistance, minimizing biological fouling helps prevent the formation of corrosive biofilms and biological degradation, contributing to overall corrosion protection [123,124].

DLC can also be engineered to have hydrophobic properties, which repel water and reduce the formation of a water layer on the coated surface [125]. This helps to further limit the contact between corrosive agents and the substrate, enhances the coating's ability to resist corrosion environments.

In addition to their protective properties, DLC coatings exhibit a very good adhesion to a range of substrates, including metals frequently used in marine applications such as stainless steel, aluminum, and titanium. Strong adhesion is essential for preserving the integrity of the coating and ensuring its durability over extended periods [126], thus maintaining effective protection against corrosion.

While DLC coatings provide substantial corrosion resistance, they are not without challenges. Long-term exposure to ultraviolet radiation, temperature fluctuations, and

mechanical stresses can potentially affect the coating's performance [2,39,41,127]. Additionally, achieving uniform coverage and strong adhesion on large or complex surfaces can present technical difficulties.

Overall, DLC coatings offer significant benefits in terms of corrosion resistance, particularly in aggressive marine environments. Their combination of barrier protection, chemical inertness, low permeability, and mechanical durability makes them highly effective for extending the service life of materials exposed to harsh conditions.

4 MATERIALS AND METHODS

This section encompasses the executed work plan, the methods and tests employed, the equipment utilized, the sample preparation procedures, and the conducted characterizations.

4.1 SUBSTRATE PREPARATION

Samples of AISI 316L stainless steel were employed for the analyses and studies conducted. The selection of this alloy is justified by its excellent balance of corrosion resistance, cost-effectiveness, and ease of fabrication. AISI 316L is often used in aerospace structures and engine parts due to its reliable performance under demanding conditions, making it a practical choice for this study. While other alloys like AISI 904L and super duplex offer higher resistance in extreme environments, 316L provides effective protection against chloride-induced corrosion in marine environments at a more economical cost. Its low carbon content minimizes the risk of sensitization and intergranular corrosion, ensuring long-term durability. Additionally, 316L's good weldability and oxidation resistance further support its suitability for the analyses and studies conducted. Table 3 outlines the key characteristics and properties of the substrate material used.

Table 3 - Properties and characteristics of stainless steel 316L as provided by the supplier.

Series 300	**Type**	**Chemical composition**	**Specific weight [g/cm³]**	**Elasticity module [N/mm²]**	**Structure**	**Brinell hardness**
ASTM (AISI) 316 L	Chrome Nickel Molybdenum Steel	C% 0.03 max. Mn%2.00max. Si% 1.00 max. Cr% 16.00 Ni% 10.00 Mo% 2.00	7.95	193.000	Austenitic	Annealed HRB 120-170

Source: Irestal *Group* [128]

The substrate material was cut into cylindrical-shaped specimens with diameters of 20 mm and a thickness of 2 mm. Subsequently, a grinding process was carried out to equalize and level the surface, followed by cleaning to remove residues, salts, and oils, among other contaminants, ensuring the optimal adhesion of the films to the substrate material surface.

The specimens then underwent a meticulous sanding process, progressing through grit sizes #280, #400, #600, #1200, #1500, and #2000, followed by a final polishing step utilizing 0.5 μm aluminium oxide particles.

For thorough cleaning, the material underwent ultrasonic sonication while immersed in a solution of distilled water and enzymatic detergent (B4184Brij® L23 solution - Sigma Aldrich, São Paulo, Brazil) for 15 minutes. Subsequent rinsing with distilled water was followed by an additional 15-minute sonication in acetone. Subsequently, the samples were carefully shielded, securely placed in sample holders, and stored for further use.

4.2 DLC DEPOSITION PROCESS

For the deposition of DLC, a PECVD reactor was employed, comprising a vacuum chamber, voltage source, mechanical and turbo-molecular pump, and flow controllers. The power supply utilized operated at a pulsed DC voltage of 1500 VA. The mechanical vacuum pump (Edwards E2M18 - Barueri, São Paulo, Brazil) possessed an operational capacity of 24 m^3/h, working in tandem with the high-vacuum turbo-molecular pump (Avaco-Pfeiffer Hipace 300 - São Paulo, Brazil), enabling the achievement of an ultimate pressure inside the reactor in the order of $1.3x10^{-2}$ Pa.

Internally, a primary cathode cage with a diameter of 42.5 cm and a height of 43.5 cm was utilized, along with an additional cathode cage measuring 22 cm in diameter and 25 cm in height. This additional cage, constructed from a woven steel profile, featured 70% transparency and an upper opening of 6 cm in diameter. It was employed to confine ions and densify the plasma over the samples, aiming to achieve enhanced homogeneity and quality of the DLC films. At the reactor base, there was an 8 cm diameter hole for connecting the chamber to the vacuum pump, along with a pressure sensor and a voltage

source connector. Gases were introduced through an electronic controller's panel (Avaco-Cole-Parmer-São Paulo, Brazil), calibrated individually for each gas mass flow controller, to manage and control the flow of the injected gases, with a full-scale range of 100 sccm for argon gas, 20 sccm for silane gas (SiH_4), and 50 sccm for acetylene gas. Figure 10 illustrates the schematic representation of the utilized reactor.

Figure 10 – Representation of PECVD reactor system.

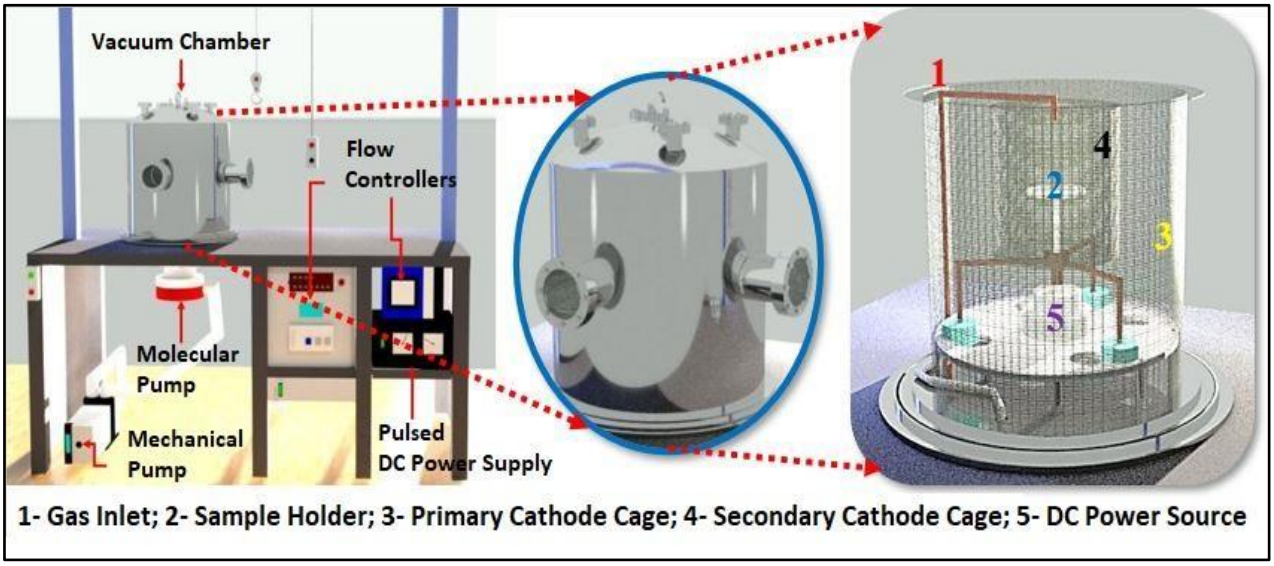

Source: Author.

Before deposition, the specimens underwent a 20-minutes cleaning process employing argon plasma. In this study, silicon (Si) is used as an intermediate layer between the metal substrate and the DLC coating.

This interlayer improves adhesion, as previous described by Bonetti *et al.*[69], by forming a strong bond between the metal and carbon layers, thereby enhancing the overall durability and performance of the coating system. This approach ensures that the DLC coating remains securely attached to the metal substrate, even under challenging conditions [69,129]. Acetylene gas (C_2H_2) was employed as the carbon precursor for the DLC layer. To ensure plasma stability, the transition between gases in different stages was performed gradually. After the deposition stages were completed, the samples were cooled for at least 5 hours under high vacuum before being removed from the chamber, properly protected in a Ziplock plastic bag, and stored for future use.

Table 4 outlines the parameters for the DLC coating deposition process stages.

Table 4 - DLC film deposition parameters.

Stage	Gas	Work pressure [Pa]	Voltage [V]	Current [A]	Gas Flow [sccm]	Time [min]
Cleaning	Argon	0.4	600	0.10	10	20
Transition	Argon Silane	2.26	700	0.05	5 5	5
Interlayer	Silane	2.66	700	0.05	5	15
Transition	Silane Acetylene	1.06	700	0.07	5 15	5
Deposition	Acetylene	0.8 to 0.93	700	0.07	15	120

Source: Author.

4.3 TIO_2 LAYER DEPOSITION PROCESS

The deposition of the titanium dioxide (TiO_2) film onto the DLC was achieved using the Beneq TFS-200 ALD reactor (Beneq Oy, Espoo, Finland). The reactor was set to operate in thermal mode at 200 °C, completing a total of 1500 reaction cycles. Titanium tetrachloride ($TiCl_4$) was chosen as the precursor, boasting a purity level of 99.94%, while ultrapure water (H_2O) served as the oxidizing agent. For the purging process, high-purity nitrogen gas (N_2) at 99.99% was employed.

The deposition parameters were carefully configured to minimize the impact of temperature on DLC film properties. The reaction cycle initiates with a 250 ms pulse of $TiCl_4$, followed by a 2-second purging phase, then another 250 ms pulse of H_2O succeeded by an additional 2-second purging phase. The total deposition process lasts approximately one hour, and 30 minutes followed by 3 hours of gradual cooling. Figure 11 provides a visual representation of the reaction cycle employed for the deposition of titanium dioxide through the ALD technique.

Figure 11 – Representation of TiO_2 layer deposition cycle through the ALD technique.

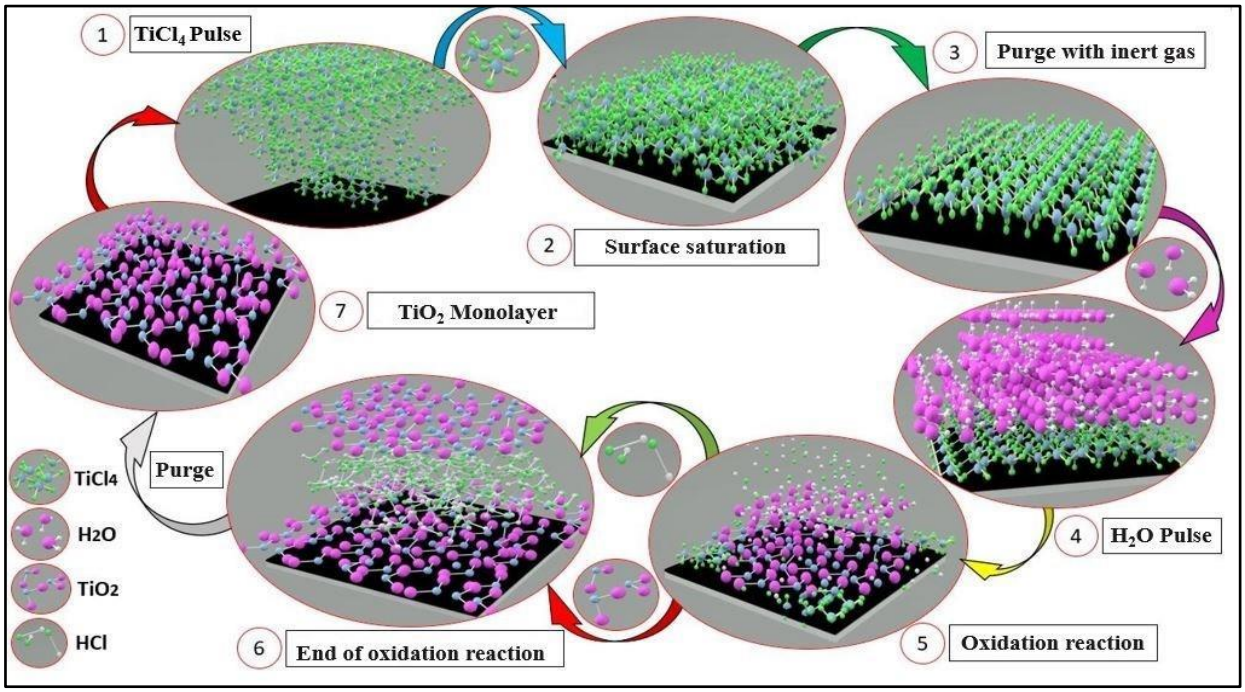

Source: Author.

4.4 FILMS CHARACTERIZATION

The characteristics of the obtained films were analyzed using Scanning Electron Microscopy (SEM) for morphology, Energy Dispersive Spectroscopy (EDS) for elemental analysis, Raman Spectroscopy for chemical structure analysis, optical and contact profilometry for roughness and thickness evaluation, scratch testing for adhesion assessment, nanoindentation for hardness, Salt Spray testing for behavior in saline environments, and evaluation of degradation due to ultraviolet radiation exposure. Figure 12 provides an overview of the work plan.

Figure 12 – Workflow of the executed plan.

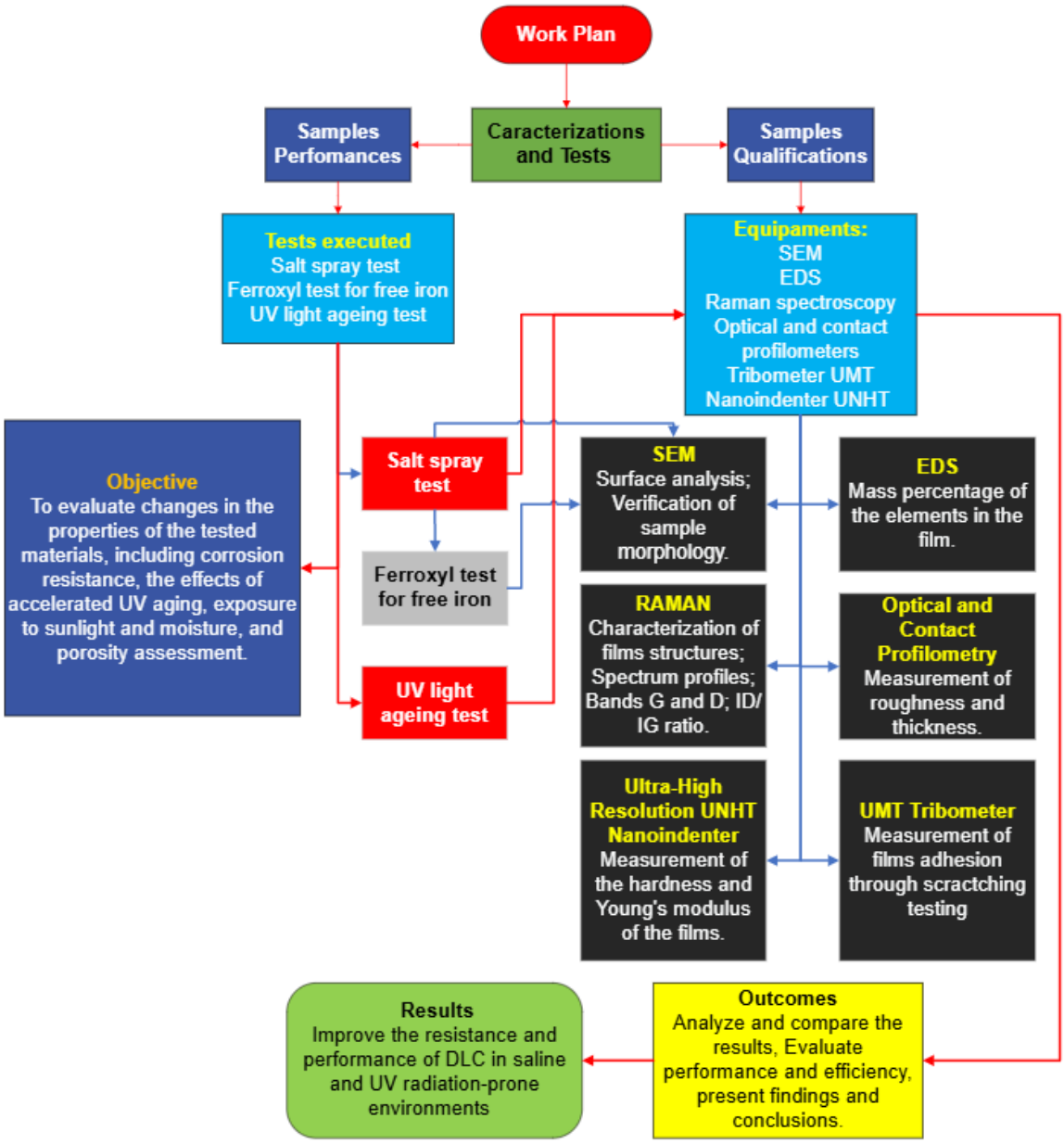

Source: Author.

4.5 SURFACE EVALUATION

The surfaces of the samples, when necessary, were analyzed using scanning electron microscopy (SEM) with the ZEISS EVO MA 10 system, located in São Paulo, SP, Brazil. The examination was performed to evaluate the surface conditions of the samples

both before and after testing. Additionally, energy-dispersive spectroscopy (EDS), integrated with the SEM system, was utilized to quantify the elemental composition within the film. Figure 13 illustrates the equipment utilized for these analyses.

Figure 13 – Scanning Electron Microscope - EVO MA 10 from IP&D - UNIVAP.

Source: Author.

4.6 RAMAN SPECTROSCOPY

The obtained films underwent examination using Raman spectroscopy, which was employed to identify carbon phase bands, analyze the displacement and width of characteristic bands, and determine the I_D/I_G ratio in the tested samples. The Raman spectra of the studied films were analyzed by fitting with a Gaussian function, followed by deconvolution of the curves for the D and G bands. To estimate the sp^3 hybridization ratio qualitatively, the I_D/I_G value was calculated from the areas under the D and G bands [35,36,130,131,132,133,134].

The analysis was conducted utilizing a Renishaw 2000 system equipped with an argon ion laser (λ = 514 nm) in a backscattering configuration. The laser beam, with a diameter of 2.5 μm, delivered approximately 0.6 mW of power to the sample. Raman shift

calibration was performed using the diamond band at 1332 cm^{-1}. The measured range varied between 80 cm^{-1} and 4000 cm^{-1}, with an acquisition time set to 30 seconds, 3 accumulations, and three points measured per sample. All assessments were carried out under ambient conditions at room temperature. Figure 14 shows the equipment used, which consists of a laser radiation source, a sample insertion system, a monochromator, a scattered radiation detector, a signal amplifier, an optical microscope, and a computer.

Figure 14 – Raman spectrometer – LABRAM from LAS laboratory – INPE.

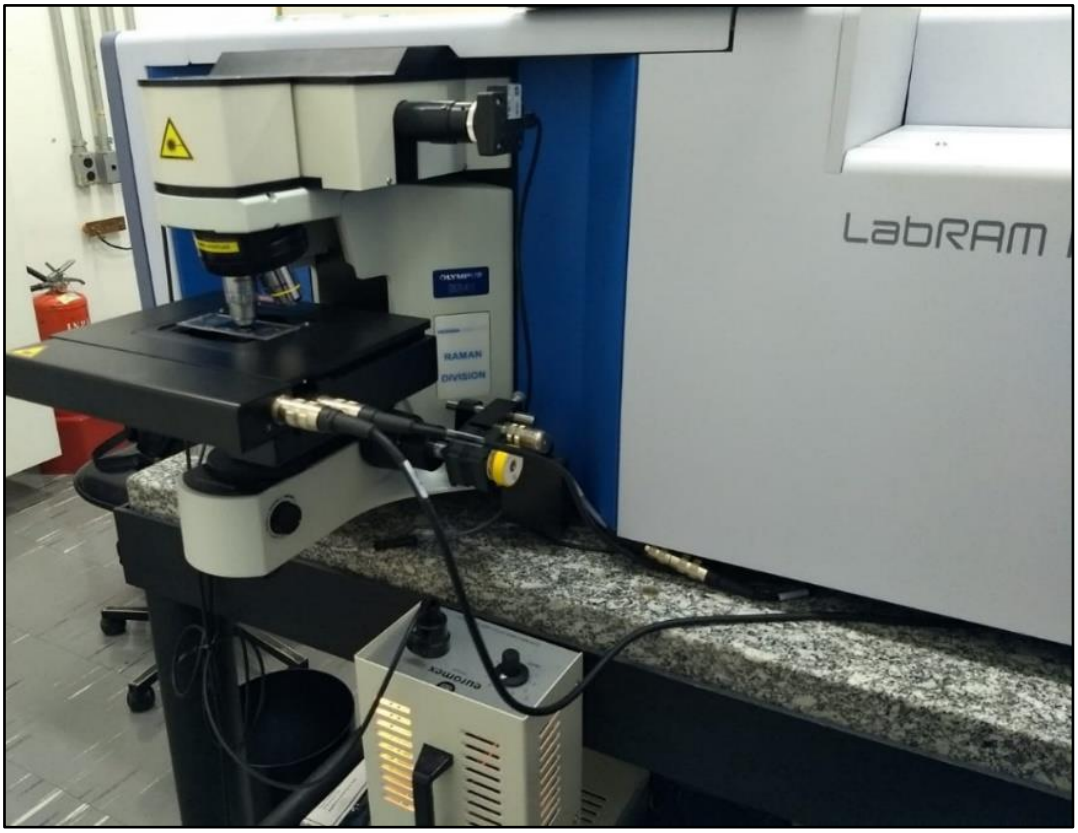

Source: Author.

4.7 ROUGHNESS AND THICKNESS

Both optical and contact profilometers were employed to measure the roughness and thickness of the samples. The optical profilometer, a Wyko NT1100 (Bruker) model integrated with Vision 32 software, from Bruker, São Paulo, Brazil, was utilized to measure the thickness of DLC-coated samples and the roughness of all samples. Figure 15 shows

the optical profilometry equipment used. The VSI (Vertical Scanning Interferometry) mode was employed to measure both arithmetic roughness (Ra) and quadratic roughness (Rq). Each sample was measured at three distinct points, with the average roughness values calculated for subsequent comparison of the films deposited.

The roughness was assessed using Ra and Rq parameters. The comparison between Rq and Ra was important to detecting surfaces with random peaks or valleys, as Rq highlights these features more than Ra by squaring the error in Y direction, due to this the Rq results give extra weight to high values and are about 11% higher than Ra. On the other hand, the Ra value over a sampling length represents the average roughness. Therefore, if an atypical peak or valley appears on the surface, the average value will not undergo significant alteration, potentially concealing such a defect.

Figure 15 – Optical profilometry equipment from LAS laboratory – INPE.

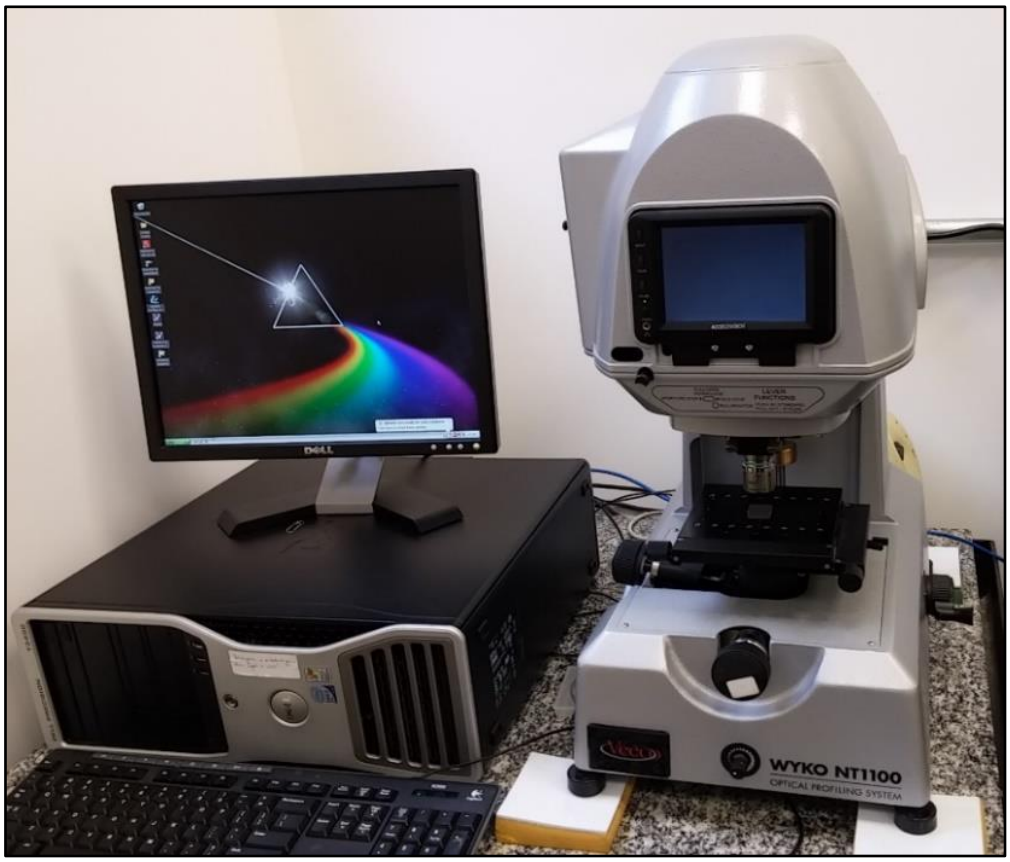

Source: Author.

$$Ra = \frac{1}{L}\int_0^L |y|\,dx \tag{2}$$

$$Rq = \sqrt{\frac{1}{L}\int_0^L (y^2)dx} \tag{3}$$

The thickness of the DLC/TiO_2 film was measured using a contact profilometer with nanoscale resolution, specifically the Dektak 150 Veeco model. Figure 16 shows the contact profilometry equipment used.

This method was selected due to several challenges associated with using an optical profilometer for such thin films. The transparency of the TiO_2 layer posed a significant issue, as the optical profilometer relies on the reflection of light from the surface to detect height differences. Since TiO_2 is a transparent material in the visible spectrum, the light passes through the film, resulting in weak reflections from the surface of the film and the substrate [78]. This weak reflection makes it difficult for the optical system to accurately detect the boundary between the film and the substrate.

Figure 16 – Contact profilometer from Lamult laboratory – UNICAMP.

Source: UNICAMP [135].

Additionally, multiple reflections occur when light reflects from both the top surface of the TiO_2 film and the underlying substrate. These reflections can interfere with each other, causing optical interference patterns that obscure the true thickness of the film. This phenomenon, known as optical interference, results in the formation of constructive or destructive interference patterns, which can further distort the measurement of the film's thickness [136].

Given these limitations, a contact profilometer was employed, as it physically traces the surface without relying on light reflections. This ensures precise and reliable thickness measurements, especially for thin, transparent films like TiO_2. The thickness measurements were conducted on a silicon sample partially coated with the film to provide an accurate baseline.

4.8 ADHERENCE ASSESSMENT

The film's adhesion was assessed following the ASTM C1624 standard for the scratching test. This method outlines how to assess the practical adhesion strength and identify mechanical failure modes of hard ceramic coatings, applied to both metal and ceramic substrates, under ambient temperature conditions [102].

This test involved producing controlled damage to the hard ceramic coating by scratching it with a Rockwell C diamond indenter with a conical geometry of 120°, a tip radius of 200 µm, and a height of 299.78 µm. The indenter was applied across the flat surface of the sample at a constant speed, with the normal force measured and controlled throughout the process. The method provided a quantitative measure of the practical adhesion strength and damage resistance of the coating-substrate system. The progressive loading (PL) mode was employed for the film scratching test. A preload force of 0.5 N was applied, and the load force ranged from 0 to 20 N during the test. The horizontal displacement rate was set at 6 mm/min, with a force application rate of 12 N/min, covering a total scratch length of 10 mm. The test was conducted three times on each type of sample tested using a Tribometer UMT Bruker Model, São Paulo, SP, Brazil, under a relative humidity of 50% and a temperature of 21°C. Post-test, the critical scratch load and the type of cracks formed were examined on the scratched track using an optical

microscope and, in some cases, SEM. The first critical load (Lc1), is marked by the initial signs of damage or cracks in the coating and the second critical load (Lc2) is associated with the start of chipping failure extending from the arc tensile cracks, indicating adhesive failure between the film and the substrate, with a continuous substrate exposure [102,137]. The results were then compared with literature. Figure 17 shows the tribometer used.

Figure 17 – Tribometer UMT from IP&D - UNIVAP.

Source: Author.

4.9 HARDNESS ASSESSMENT

The ultra-high resolution Nanoindenter UNHT with real force and displacement sensors was used to evaluate the mechanical properties of the tested materials at the nanoscale. Linear loading mode was employed, using a diamond Berkovich indenter (a three-sided pyramid with an area-to-depth function that is the same as that of a Vickers indenter), with a loading and unloading rate of 5 mN/min, a pause of 5 s, and a maximum

depth of 100 nm (approximately 10% of the coating thickness). The tests were conducted on six samples in total: two DLC samples as controls, two DLC samples exposed to UV radiation for 204 and 408 hours, and two DLC/TiO_2 samples exposed to UV radiation for 204 and 408 hours. For each sample, ten (10) hardness measurements were taken, and the average value was computed. For calculating the hardness and Young's modulus, Oliver and Pharr's method was adopted [97,111], and the Poisson's ratio for a-C:H films was assumed to be 0.3. Figure 18 shows the equipment utilized for hardness measurements.

Figure 18 – Nanoindenter UNHT from LAS laboratory – INPE.

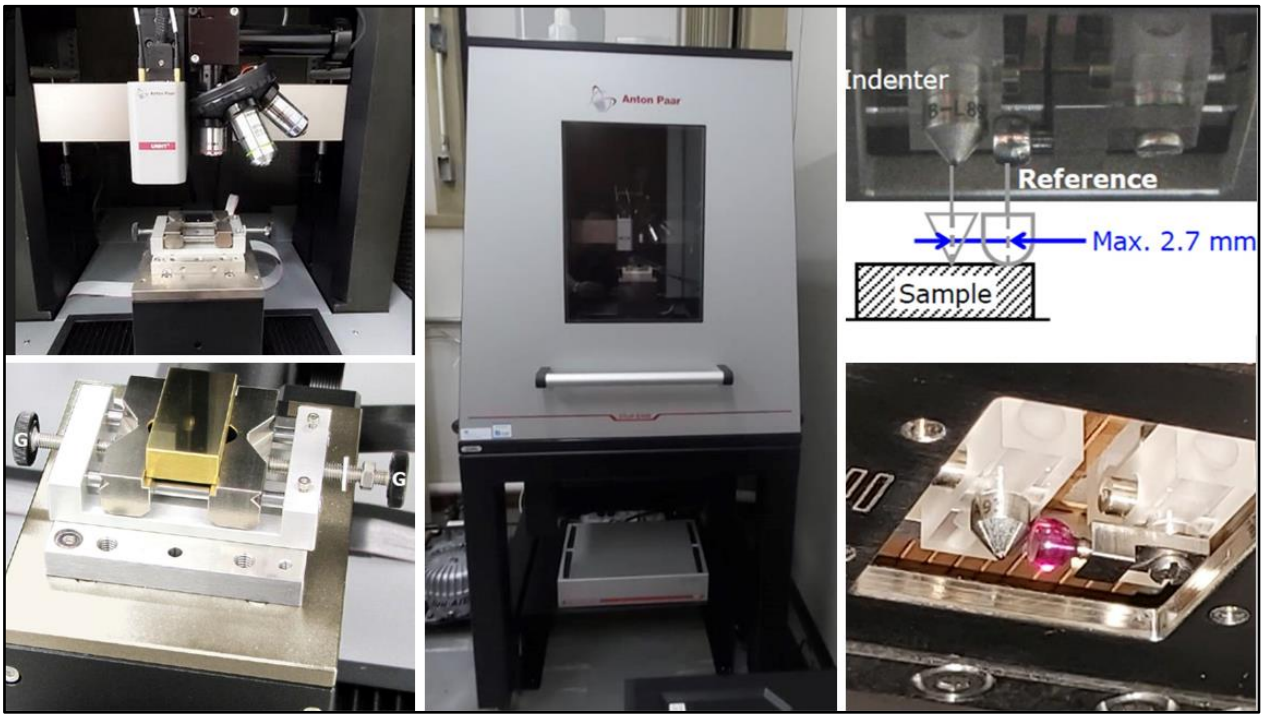

Source: Author.

4.10 SALT SPRAY TEST AND POROSITY ASSESSMENT

The coatings underwent an environmental salt spray test following ASTM-B-117 and D-1735 standards to assess their corrosion resistance when exposed to a saline atmosphere under humid conditions.

The equipment utilized was the Bass USC chamber model, enabling Salt Spray, Humidity, and Corrodkote tests. For these evaluations, two samples of 316L stainless

steel coated with DLC and DLC/TiO_2, along with one untreated 316L stainless-steel sample, were subjected to the test for a duration of 648 hours. The chamber temperature was maintained at 34.7 ºC, while the saturator temperature was set to 46.9 ºC. The salt solution was prepared by dissolving 5 ± 1 parts by mass of sodium chloride in 95 parts of water, conforming to Type IV water in Specification ASTM D 1193. The surface conditions were examined before and after the tests using SEM. Figure 19 presents the equipment used.

Figure 19 – Bass USC chamber from ELEB.

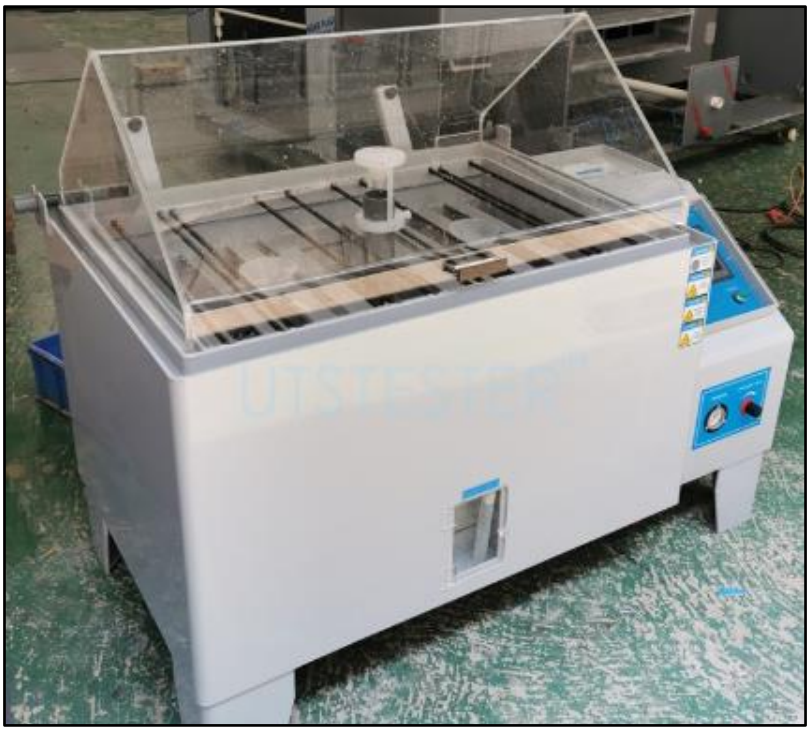

Source: Author.

Furthermore, the porosity of the films on the stainless-steel substrate were assessed both before and after the tests. This evaluation adhered to the Ferroxyl Test for Free Iron, as detailed in section 7.4 of the ASTM A 380 standard [138]. The objective was to determine whether, at any point in the films, the substrate had been exposed to the environment due to corrosion by identifying iron contamination originating from various sources, including residual-iron salts from pickling solutions, iron dust, atmospheric exposure, iron deposits, and iron oxide. The test solution is prepared by first adding nitric

acid to distilled water and then adding potassium ferricyanide, in the proportions as presented in Table 5.

Table 5 – Ferroxyl Test for Free Iron solution proportions

Composition	Weight %	Quantities
Distilled water	94	1000 mL
Nitric acid (60–67 %)	3	20 mL
Potassium ferricyanide	3	30 g

Source: ASTM A 380 [138]

4.11 UV LIGHT AGEING TEST

The QUV Accelerated Weathering Tester was employed to evaluate the effects of accelerated ageing through UV exposure on DLC and DLC/TiO_2 films deposited onto a 316L stainless steel substrate. The tests followed ASTM G154 practices [139], where each coating type was placed in the UV test chamber equipped with fluorescent lamps (Irradiance: 0.89 W/m^2/nm, wavelength: 320 to 400 nm, and temperature of 60 °C). The chamber operated on an 8-hour on and 4-hour off cycle with condensation.

Two sets of five samples each underwent testing, accumulating a total of 408 hours of exposure. These conditions aimed to assess changes in the properties of the tested materials when exposed to sunlight and moisture, such as rain or dew, in real-world conditions. Subsequently, a thorough inspection and analysis of the samples were conducted to identify any visible changes in color, chalking, cracking, peeling, blistering, fading, and loss of physical properties.

SEM and Raman spectroscopy were also employed on the samples before and after the test to compare the surface conditions and changes in film Raman spectra. Figure 20 shows the equipment used for the UV ageing test.

Figure 20 – QUV Accelerated Weathering Tester from Mackenzie.

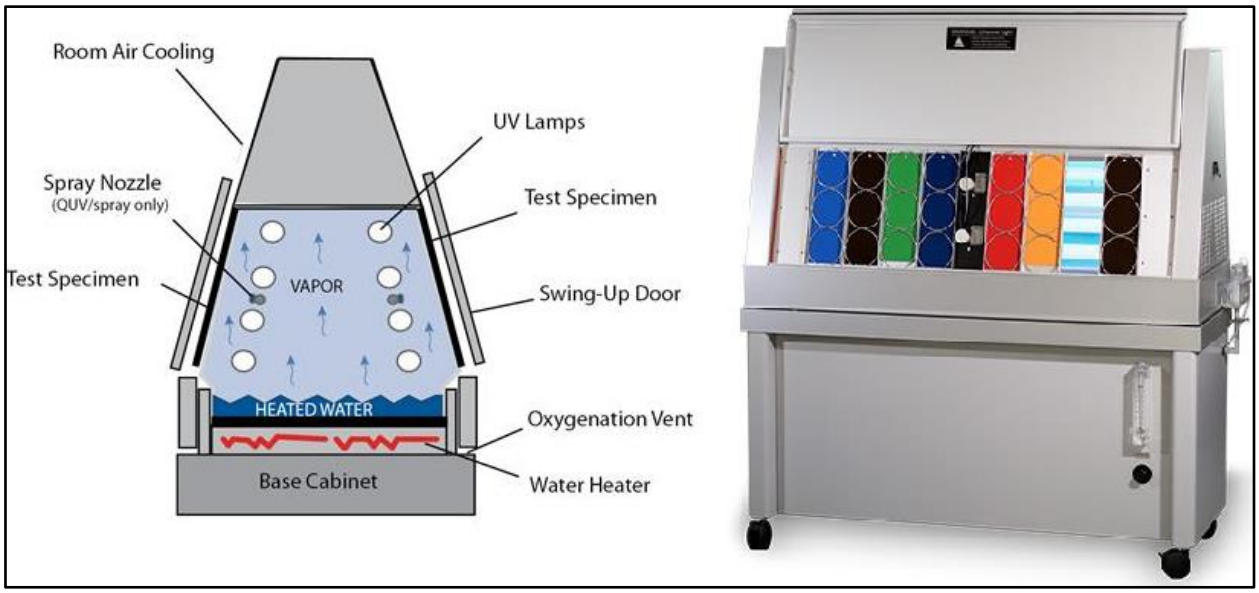

Source: Adapted from manufacturer website [140].

5 RESULTS AND DISCUSSION

This chapter presents and discusses the results of the characterizations and tests conducted on DLC and DLC/TiO_2 coatings on 316L stainless steel to evaluate their resistance to degradation from UVA radiation and exposure to a saline environment.

5.1 DLC AND TIO_2 CHEMICAL STRUCTURE

The properties of DLC coatings are intricately tied to the I_D/I_G ratio, H content, and the shift of the bands D and G [1]. The D band, associated with the disorder, encompasses vibrational modes linked to sp, sp^2, and sp^3 hybridizations, while the G band indicates a tangential elongation of the sp^2 hybridization mode [141], and its intensity exhibits a direct correlation with the content of sp^2 bonds [126]. The ratio of sp^3 to sp^2 varies considerably as a function of the hydrogen content, which is one of the key factors in increasing the sp^3 fraction in hydrogenated DLC (a-C: H) [20,22].

Considering these known correlations, a detailed Raman analysis was carried out for the samples under study to assess the specific characteristics of the DLC coatings. The data were fitted using a Gaussian function, followed by deconvolution of the plotted curves for the D and G bands. Each film was analyzed before and after the test to verify the variation in D and G bands, I_D/I_G ratio, and full width at half maximum of the G band ($FWHM_G$).

The bands D and G vary from 1346 to 1375 and 1539 to 1549 cm^{-1}, respectively and the I_D/I_G ratio varies from 0.52 to 0.73 for DLC and 0.68 to 0.71 for DLC/TiO_2 specimens, as presented in Table 6.

Table 6 – I_D/I_G ratio, D and G band positions, and FWHM of G bands were measured before testing for DLC and DLC/TiO_2 coating surface.

Sample Type	Band D	Band G		
	Band Position [cm^{-1}]	**Band Position [cm^{-1}]**	**$FWHM_G$ [cm^{-1}]**	**I_D/I_G**
DLC	1346 - 1365	1539 - 1544	195 - 203	0.52 – 0.73
DLC/TiO_2	1369 - 1375	1547 - 1549	186 - 188	0.68 – 0.71

Source: Author.

The incorporation of the TiO_2 layer via the ALD process resulted in a slight rightward shift in the D band of the DLC films, with no significant change observed in the G band or the I_D/I_G ratio. The $FWHM_G$, a measure of the disorder [98,99], showed some minor effects due to the ALD deposition process.

The I_D/I_G ratio, which is directly related to the sp^2/sp^3 ratio, suggests a higher prevalence of sp^2 bonding over sp^3 [98]. Additionally, the photoluminescence slope of the DLC Raman spectrum, along with the I_D/I_G ratio and G band positions, aligns with those of a low-hydrogenated film (<20%), collectively categorizing the DLC films as a-C: H [142]. Moreover, the slight rightward shift in the D band suggests the presence of clusters containing aromatic carbon rings and open-chain carbon bonds within the coatings.

5.2 Results of UV ageing test

Figure 21 presents a comparative analysis of Raman spectra for DLC/TiO_2 and DLC films on an AISI 316L substrate before and after UV exposure.

Figure 21(a) illustrates the characteristics of the DLC/TiO_2 film, highlighting the active Raman modes of the anatase phase deposited on DLC samples. Since the TiO_2 film is very thin (see section 5.3. Film thickness and roughness measurements), the laser penetrates the film and detects both the DLC and TiO_2 interlayers. Figure 21(b) DLC/TiO_2-film sample before UV ageing test. Figures 21(c) and 21(d) present the spectrum of the DLC/TiO_2 film after 204 and 408 hours of UV ageing, respectively. Figure 21(e) shows the spectrum of the DLC film before UV ageing. Figures 21(f) and 21(g) present the spectrum of the DLC film after 204 and 408 hours of UV ageing, respectively.

The Raman spectra of the studied films were analyzed to identify the D and G bands, estimate the sp^3 hybridization ratio qualitatively, and calculate the I_D/I_G value based on the areas under these bands. When examining the Raman spectra of the DLC/TiO_2 film after 204 hours of UV exposure, as shown in Figure 21(c), several bands were observed at 143, 399, 519, and 639 cm^{-1}, corresponding to the active Raman modes characteristic of the anatase phase of TiO_2 [9], as previously described in section 3.10. Additionally, discernible bands at 1374 and 1544 cm^{-1} correspond to the D and G bands of the DLC film [99,142].

Figure 21 – Comparative Raman spectra analysis of DLC/TiO_2-film and DLC samples on the AISI 316L substrate before and after UV exposition. (a) DLC/TiO_2-film sample characteristic with active Raman modes of the thin anatase phase of TiO_2 film deposited on DLC samples; (b) DLC/TiO_2-film sample before UV ageing test; (c) DLC/TiO_2-film sample after 204 hours of UV ageing test; (d) DLC/TiO_2-film sample after 408 hours of UV ageing test; (e) DLC sample before UV ageing test; (f) DLC sample after 204 hours of UV ageing test; (g) DLC sample after 408 hours of UV ageing test.

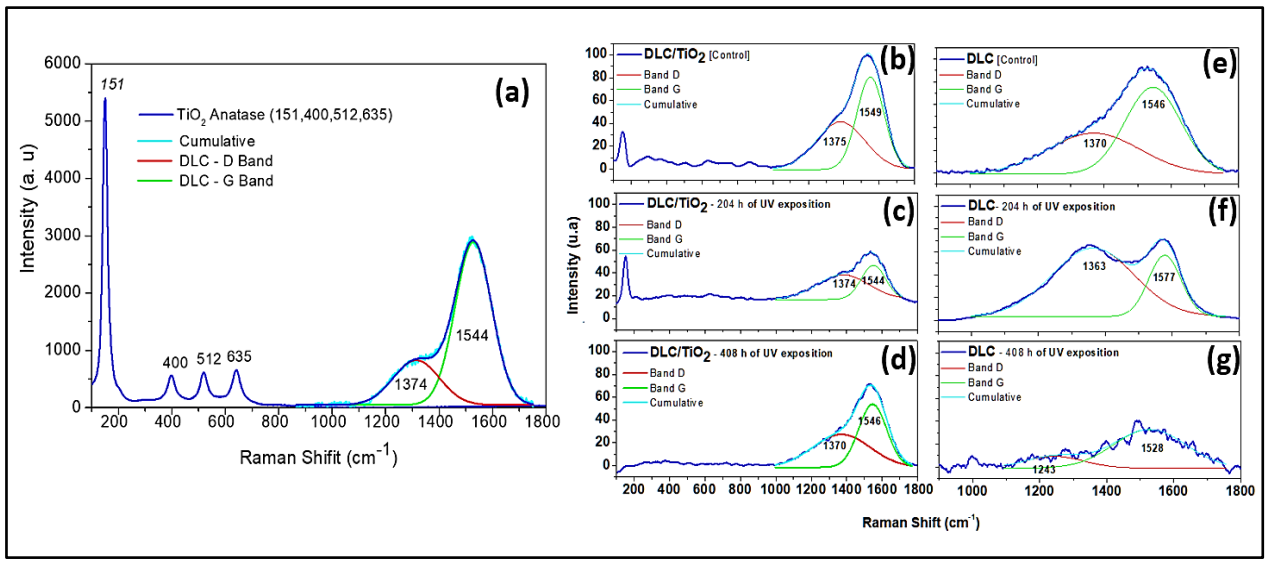

Source: Author.

After completing the 408-hour UV test cycle, the bands related to the anatase phase of TiO_2 are no longer discernible, as shown in Figure 21(d). Only the distinctive signature of the DLC film remains, represented by the D and G bands, closely resembling those of the DLC control sample, as shown in Figure 21(e). Samples containing only the DLC film exposed to UV radiation exhibited significant variations in their Raman spectra compared to the control sample and those films with the TiO_2 layer, indicating continued degradation of the film, as illustrated in Figures 21(f) and 21(g). Upon closer examination of the DLC film samples after 408 hours of UV ageing, substantial changes were observed in the DLC Raman spectrum signature, making the identification of the D and G bands challenging.

The values of I_D/I_G in samples subjected to UV testing, as displayed in Table 7, show significant changes compared to the reference samples in Table 6, accompanied by

notable alterations in band shape. During the first 204 hours of UV exposure, the values of the I_D/I_G ratio increased, $FWHM_G$ decreased, and band G position had a rightward shift tendency. At the end of the 408-hour test period, the I_D/I_G ratio for DLC films decreased to a lower value compared to the initial and those obtained after 204 hours of testing. Additionally, the $FWHM_G$ increased, which means that the band is broader, indicating a greater range of frequencies contributing to the band [99]. This broadening can be caused by various factors, such as disorder or defects in the carbon structure [99,143]. There was also a tendency for a leftward shift in the band G position, which indicates a decrease in the wavenumber value at which the band reaches its maximum intensity [99]. This shift can also be associated with changes in the carbon structure, such as an increase in disorder or a shift towards sp^2 hybridization [143]. Together, an increased FWHM and a leftward shift in the position of the G band may suggest changes in the carbon structure of the DLC film, potentially indicating a decrease in the diamond-like character and an increase in disorder or defects [29,98,133,143].

Table 7 – I_D/I_G ratio, D and G band positions, and FWHM of G bands measured after 204 and 408 hours of UV ageing testing for DLC and DLC/TiO_2 coating surface.

Sample Type	Band D	Band G		
	Band Position [cm^{-1}]	**Band Position [cm^{-1}]**	**FWHM [cm^{-1}]**	**I_D/I_G**
DLC [204 hours]	1363 - 1412	1546 - 1577	114 - 170	2.4 - 2.8
DLC [408 hours]	1243 - 1336	1528 - 1541	190 - 255	0.3 - 0.5
DLC/TiO_2 [204 hours]	1368 - 1370	1544 - 1546	179 – 181	1.08 – 1.15
DLC/TiO_2 [408 hours]	1374 - 1388	1545 - 1546	182 - 188	1.2 - 1.3

Source: Author.

Figure 22 compares the average width of the $FWHM_G$ band and the I_D/I_G ratio variations among the different film samples studied. These variations are summarized in Table 8.

Comparing the DLC sample before and after 204 hours of UV exposure were observed a 28.64% reduction in $FWHM_G$ after 204 hours and a 4.52% reduction after 408

hours. Conversely, for DLC/TiO_2 film, the reductions were 2.15% after 204 hours and 0.53% after 408 hours of exposure. This suggests that after 204 hours, DLC exhibited a narrower band, indicating an enhancement in the graphite phase. Additionally, the increase in I_D/I_G to 371% after 204 hours reveals a transition from amorphous carbon to graphite phase, with a progressive reduction in amorphous phase and the promotion of ordered graphite layers while retaining aromatic small graphite rings.

This indicates a transition from sp^3 to sp^2 bonding due to hydrogen desorption and graphitization of the DLC structure [144], resulting in a decrease in the sp^3 fraction and a reduction in the disorder band [2]. After 408 hours, the I_D/I_G ratio decreased significantly from 2.6 to 0.4, primarily due to the intense degradation of the D band in the DLC film, as shown in Figure 21(g). This transition or alteration in the DLC film could potentially lead to complete degradation or mischaracterization, as UV irradiation can cause the breakage of sp^3 C-H bonds in a-C:H film. This, in turn, increases the number of dangling bonds in the films and decreases their wear life [145].

Table 8 – Percentage variations of I_D/I_G ratios and $FWHM_G$ for DLC and DLC TiO_2 after UV exposition.

		$FWHM_G$	**$FWHM_G$ %Comp.**	**I_D/I_G**	**I_D/I_G %Comp.**
DLC	Control	199	28.64%	0.7	371.4%
	[204 hours]	142		2.6	
	[408 hours]	190	4.52%	0.4	42.8%
DLC/TiO_2	Control	186	2.15%	0.71	42.0%
	[204 hours]	182		1.01	
	[408 hours]	187	0.53%	1.19	67.60

Source: Author.

In contrast, DLC/TiO_2 film showed lower percentage reductions in $FWHM_G$, indicating a minimal reduction in the width of the G band and a low percentage of graphitization. Moreover, the I_D/I_G ratio remained around 0.7-1.19, characteristic of amorphous DLC.

Figure 22 – Comparison of the average $FWHM_G$ and I_D/I_G ratio variation of each studied film sample.

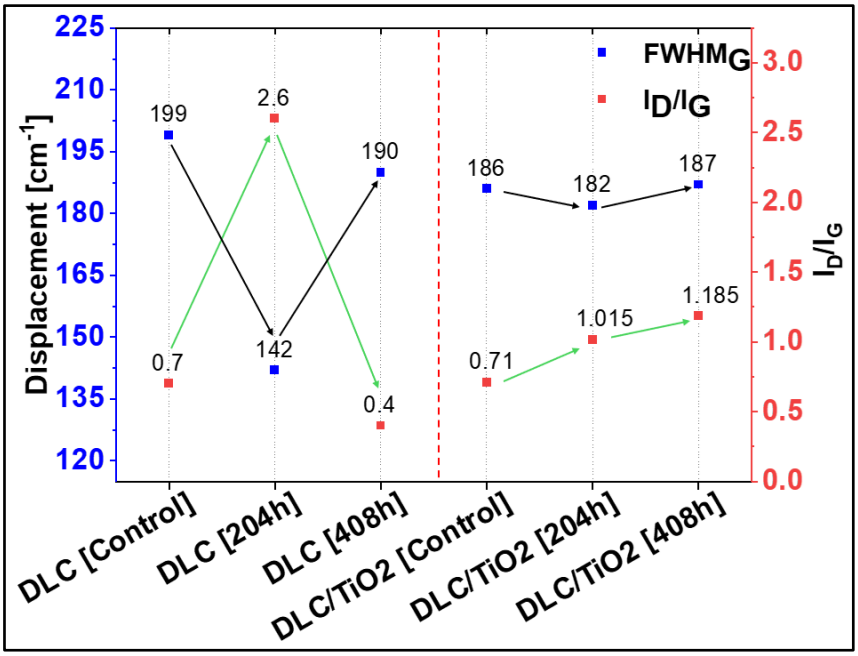

Source: Author.

Comparing the film morphology and Raman spectra, it was observed that in the samples with DLC/TiO_2 film, there was notable preservation of the DLC structure after 408 hours of testing. Only minor changes in the Raman spectra were observed compared to the control sample. However, comparing the Raman spectra after 204 and 408 hours of testing revealed the disappearance of bands associated with the anatase phase present at 204 hours, indicating some changes occurring in the TiO_2 film structure.

SEM and EDS analyses were also conducted on the samples after 204 and 408 hours of UV ageing tests for DLC and DLC/TiO_2 coating surfaces. Figure 23 displays six SEM images comparing DLC and DLC/TiO_2 film samples on an AISI 316L substrate. (a) shows the DLC film before UV ageing, (b) after 204 hours of UV exposure, (c) after 408 hours of UV exposure, (d) depicts DLC/TiO_2 before the UV ageing test, (e) DLC/TiO_2 after 204 hours of UV exposure, and (f) after 408 hours of UV exposure. Despite progressive changes in film color, no cracking or delamination of the films was observed through optical microscopy.

Figure 23 – SEM comparative analyses were conducted on DLC and DLC/TiO_2-film samples on the AISI 316L substrate. (a) DLC before UV ageing test; (b) DLC after 204 hours of UV exposure; (c) DLC after 408 hours of UV exposure; (d) DLC/TiO_2 before UV ageing test; (e) DLC/TiO_2 after 204 hours of UV exposure; and (f) DLC/TiO_2 after 408 hours of UV exposure.

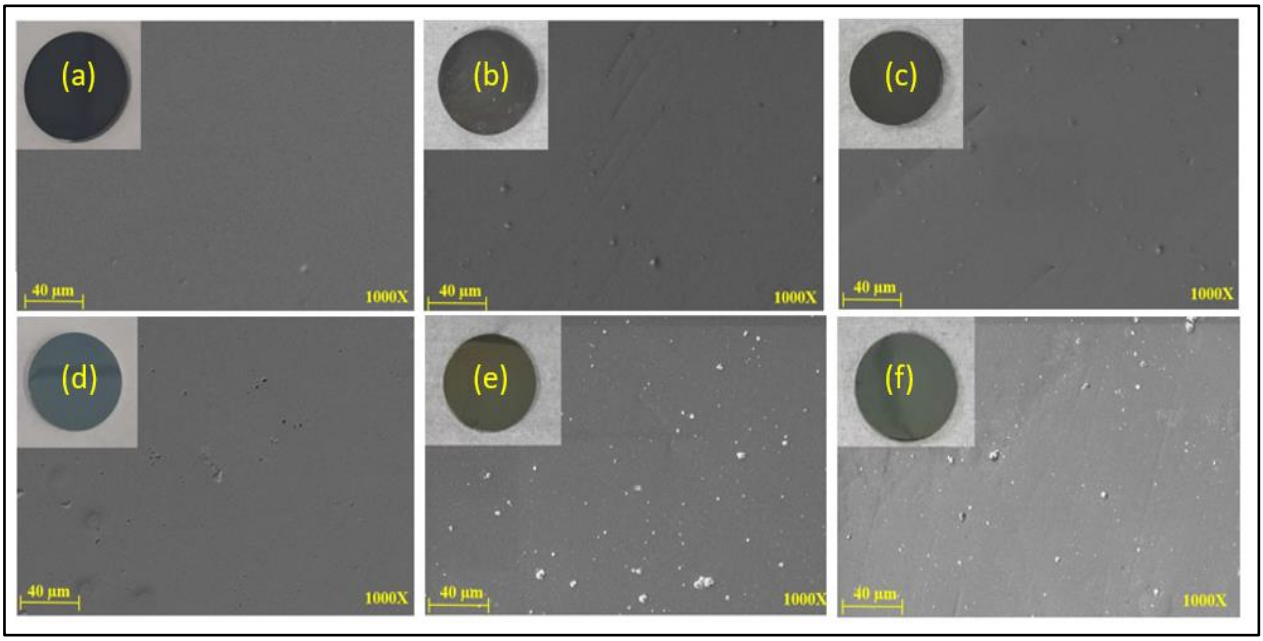

Source: Author.

Figure 24 illustrates the comparative EDS analyses: (a) after 204 hours of UV exposure and (b) after 408 hours of UV exposure. Elemental analysis was conducted using Energy Dispersive Spectroscopy (EDS), providing a semi-quantitative assessment of elemental composition. The results revealed the presence of titanium and oxygen in all samples subjected to UV testing for 204 and 408 hours. A noticeable decrease in the weight percentage of both elements was observed from 204 to 408 hours, using the same analysis area and electron beam intensity for both measurements.

Figure 24 – Comparative EDS analysis on DLC/TiO_2-film sample on the AISI 316L substrate. (a) after 204 hours of UV exposure; and (b) after 408 hours of UV exposure.

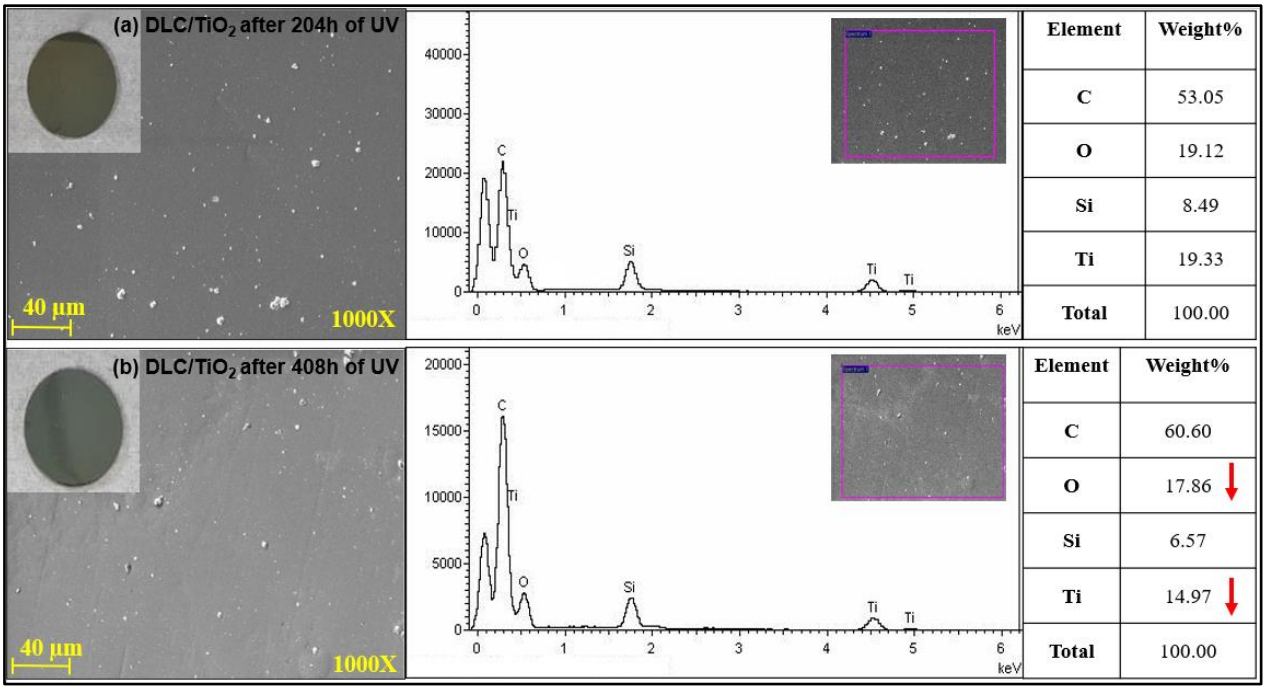

Element	Weight%
C	53.05
O	19.12
Si	8.49
Ti	19.33
Total	100.00

Element	Weight%
C	60.60
O	17.86 ↓
Si	6.57
Ti	14.97 ↓
Total	100.00

Source: Author.

5.3 FILM THICKNESS AND ROUGHNESS MEASUREMENTS

Figures 25 and 26 show the results of profilometry measurements for the thickness and roughness of DLC-film samples on the AISI 316L substrate, respectively. Using the optical profilometer, the measurements were determined from the step heights observed in the line profiles, and the thickness yielded a mean value of 1 µm. The highest roughness values, Ra and Rq, measured from the control sample were 63.77 nm and 79.87 nm, respectively, for a film of 1.1369 µm of thickness, showing a very smooth film.

The thickness of the TiO_2 layer on the DLC film was measured solely using a contact profilometer on samples with a silicon substrate due to its nanoscale dimensions. The TiO_2 thickness ranged from 85 to 100 nm (850 to 1000 Å), with an average thickness of 90 nm, as illustrated in Figure 27 (a), and the roughness is illustrated in Figure 27 (b). The highest roughness values observed for DLC/TiO_2-film samples on the AISI 316L substrate were 78.16 nm (Ra) and 93.01 nm (Rq). The increased roughness observed in

the DLC/TiO_2-film samples on the AISI 316L substrate may be attributed to several factors influencing the deposition process.

Figure 25 – Thickness measurement of DLC-film samples on AISI 316L substrate.

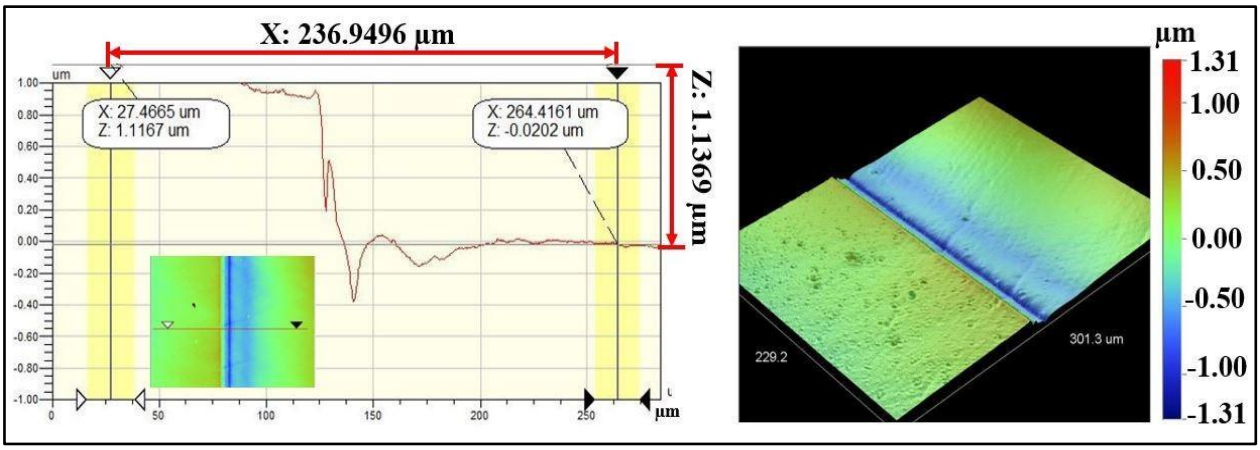

Source: Author.

Figure 26 – Roughness values (Ra and Rq) of DLC-film samples on AISI 316L substrate.

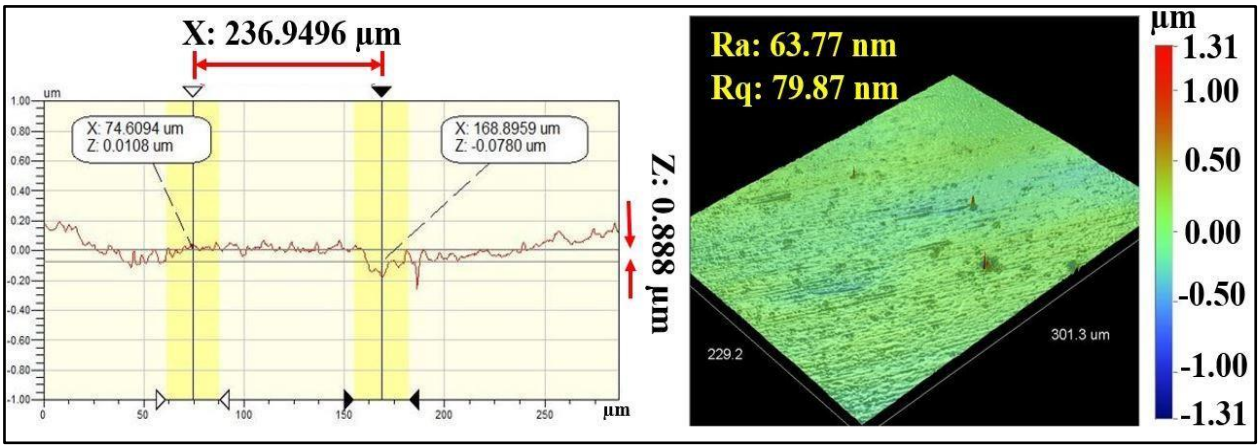

Source: Author.

Variations in deposition conditions, such as temperature, pressure, and precursor concentrations, can lead to non-uniform growth of the TiO_2 layer, resulting in surface irregularities [146,147,148,149]. Additionally, interactions between the TiO_2 molecules and the substrate surface may contribute to the formation of rough surface features during the nucleation and growth stages [147,148]. Contaminants or impurities present in the

deposition environment can also impact the surface morphology, leading to increased roughness.

Figure 27 – (a) Thickness measurement of the TiO_2 layer on DLC film using a contact profilometer on a silicon substrate, (b) Roughness values (Ra and Rq) of DLC/TiO_2-film samples on AISI 316L substrate.

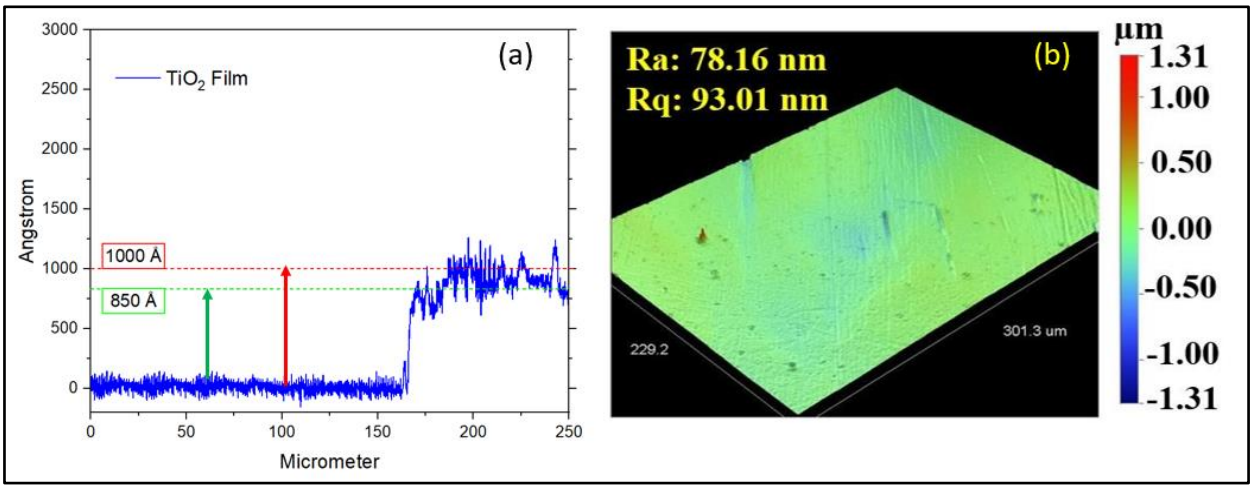

Source: Author.

It's worth noting that, on average, the roughness of the DLC/TiO_2-film samples was lower than that of those films only with DLC. However, these factors may have contributed to an increase in the dispersion in roughness measurements across the samples. Therefore, careful control of deposition parameters and thorough monitoring of the coating process are essential to minimize roughness variations and ensure consistent film quality.

Comparing Ra and Rq values between both films before the test suggests more pronounced peaks and valleys on the surface of the DLC film, contributing to a higher Rq than Ra. In practical terms, this means that while Ra gives us an average measure of surface roughness, Rq considers the dispersion of all individual peak and valley heights across the surface [150,151]. Therefore, a higher Rq indicates a broader and more varied distribution of surface irregularities in the DLC film compared to the DLC/TiO_2 film [151]. This difference in surface morphology may have significant implications for various surface-related properties, such as adhesion, friction, and optical properties, highlighting the

potential benefits of incorporating TiO_2 to achieve a more uniform and homogeneous surface characteristic.

Figure 28 illustrates the Ra and Rq roughness average values measured from five distinct samples for DLC and DLC/TiO_2 coatings before and after UV ageing tests. In the case of DLC control samples, the average Ra value obtained was 53.89 nm, with an Rq value of 70.50 nm. Notably, following UV ageing tests, the roughness of DLC samples decreased by a factor of approximately 2. The same did not occur for the DLC/TiO_2-film samples. The roughness values of the control and test samples remained relatively stable, with variation close to the standard deviation.

Figure 28 – Roughness comparison among DLC and DLC/TiO_2-film samples on the AISI 316L substrate before and after the UV ageing test.

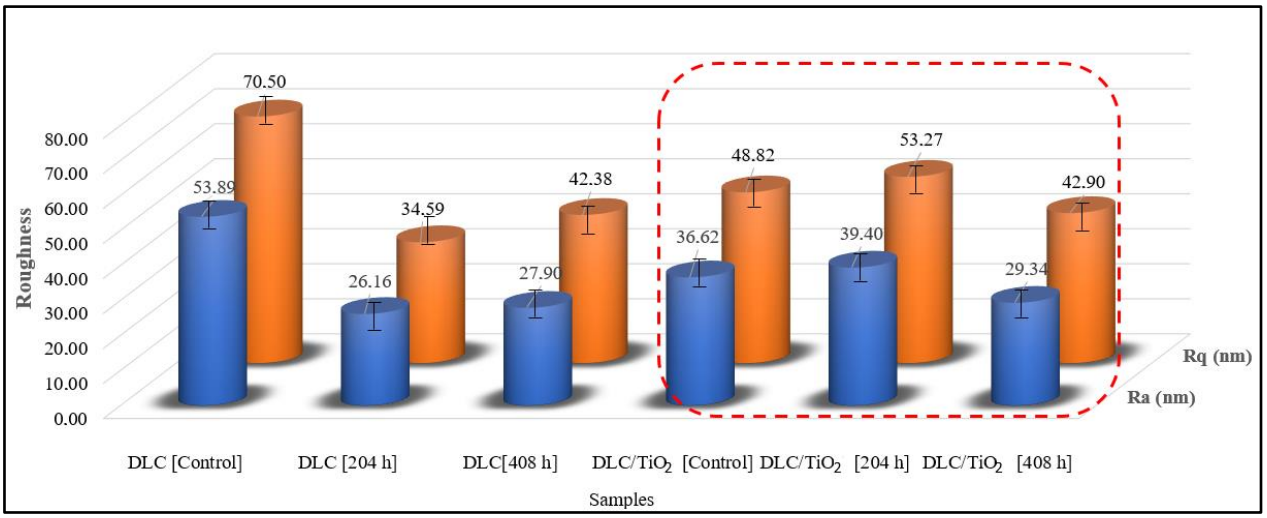

Source: Author.

5.4 ADHESION STRENGTH

Stress is a crucial inherent factor in DLC deposition, influencing adhesion quality [20]. Furthermore, stress is a measurable mechanical property. Like bulk materials, the resolution of interference-induced cracks is largely determined by mechanical properties [1].

The method used for evaluating films' cohesive and interfacial adhesive strength was the Scratch Test, following the procedures described in ASTM C1624-05. The images

of the scratch tracks on the 316L substrate film with DLC and DLC/TiO_2 before UV ageing testing were presented in Figure 29 and 30, respectively.

Figure 29 – SEM images of scratch test results for DLC film sample on AISI 316L substrate using a Rockwell C indenter before UV ageing testing. The friction coefficient (COF), in the blue line, rises from 0.10 to 0.14 and the normal force (0 to 20 N) is in the red line.

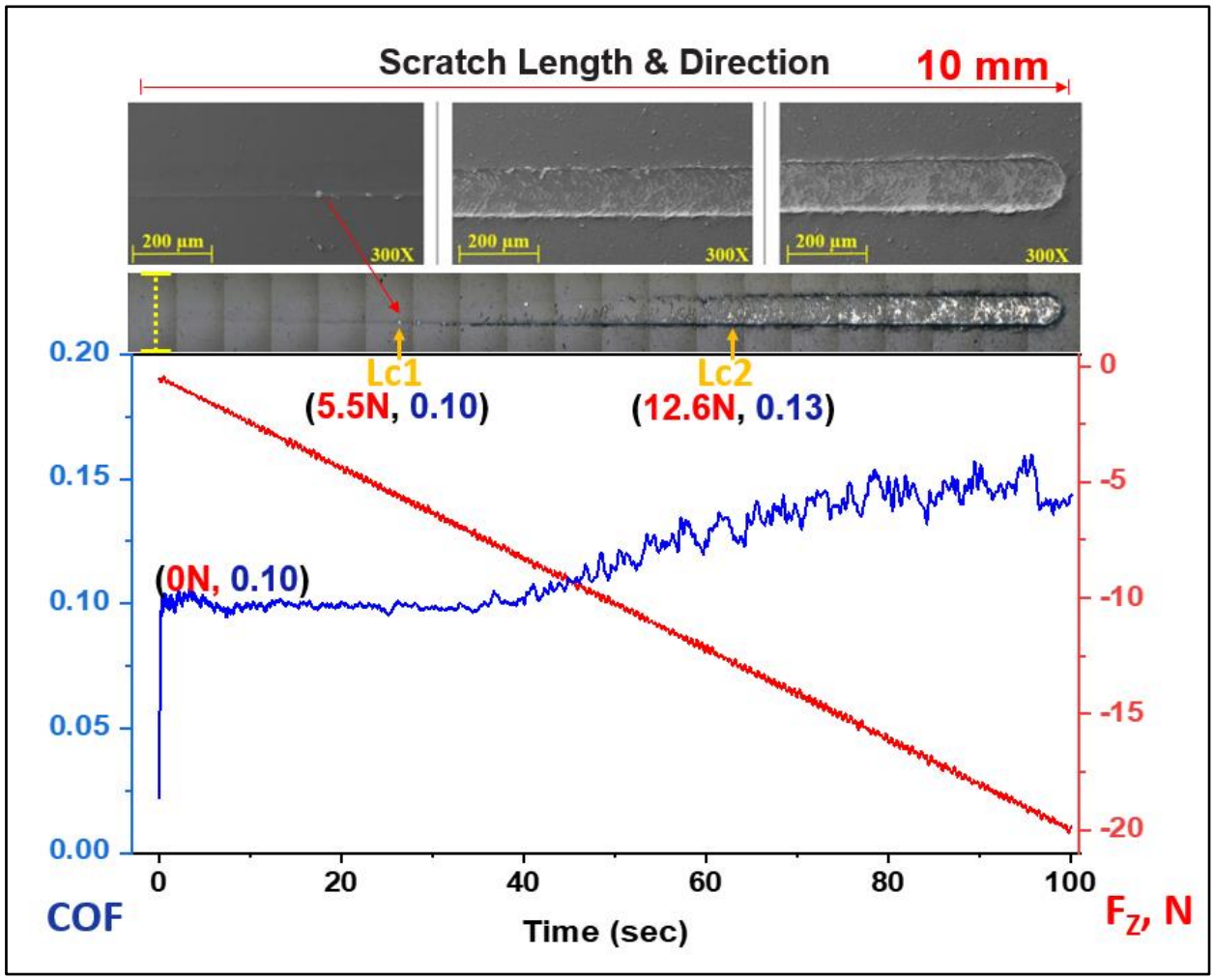

Source: Author.

The sample film with DLC exhibited the initial crack after a displacement of 2.7 mm, reaching a critical load (Lc1) of 5.5 N. The image depicts progressive failures resembling waves in that region. The adhesive failure between the film and the substrate was observed in the DLC sample after a displacement of 6.8 mm, up to a load force (Lc2) of 12.6 N. The concave curvature of the crack about the sliding direction led to cracks

forming ahead of the tip during scratching, a damage mode commonly referred to as conformal cracking [102,105,152,153].

Figure 30 – SEM images of scratch test results for DLC/TiO_2 film sample on AISI 316L substrate using a Rockwell C indenter before UV ageing testing. The friction coefficient (COF), in the blue line, rises from 0.9 to 0.18 and the normal force (0 to 20 N) is in the red line.

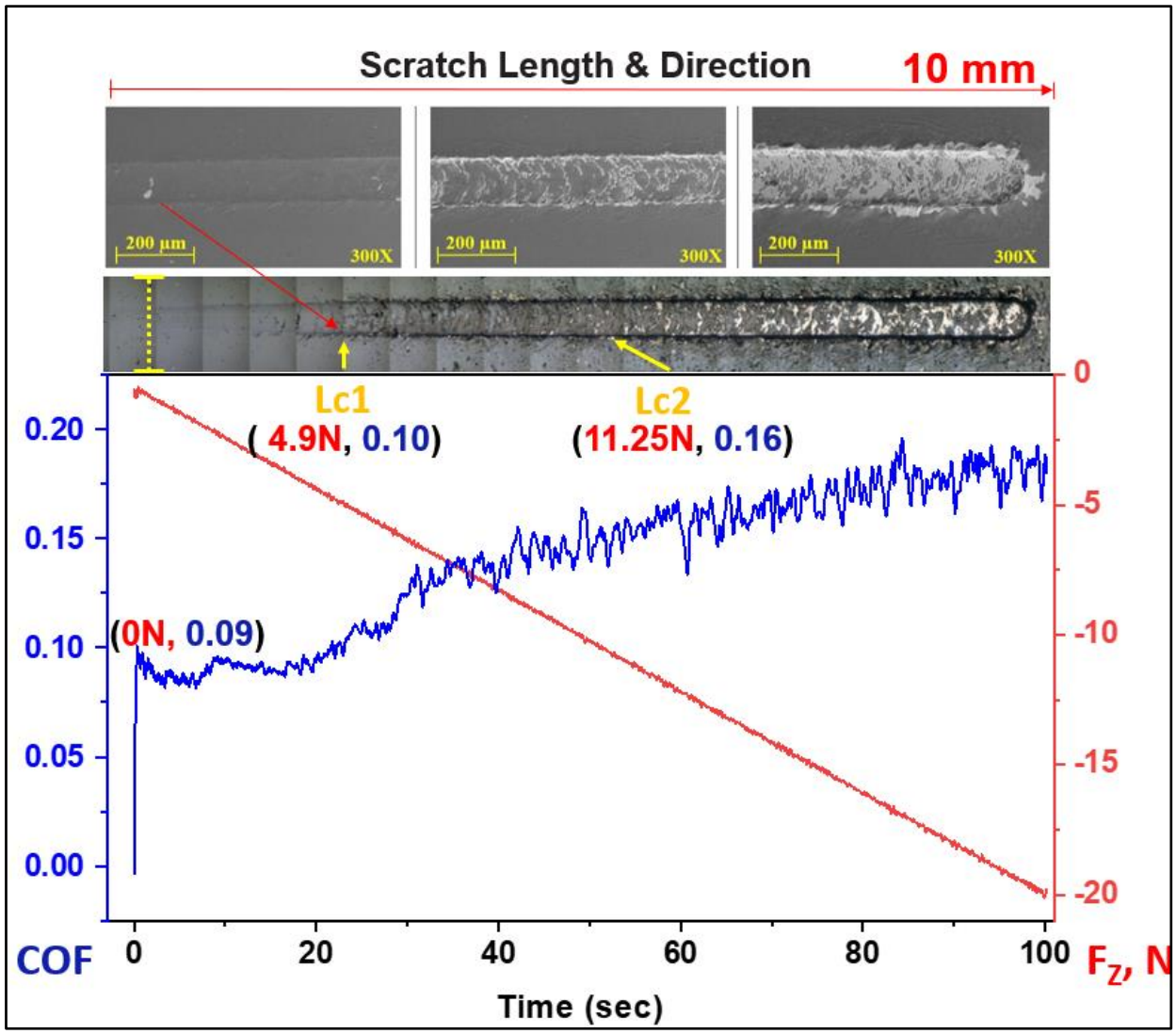

Source: Author.

Similarly, the DLC/TiO_2-film sample showed no adhesive failure with substrate exposure (Lc2) up to 11.25 N and 4.75 mm of displacement, although Lc1 occurred at 4.9 N and 2.7 mm of the beginning of scratch length. The film failures were correlated with the increase in friction forces, as indicated by a gradual rise in the friction coefficient

(COF). In this case, the crack damage was characterized by a combination of buckling cracks along the scratch track due to the compressive stress field preceding the moving stylus and bucking spallation at the end of the scratch length [102].

DLC and DLC/TiO_2 films remained partially adhered to the AISI 316L substrate up to a load of 20 N, corresponding to a scratch distance of 10 mm. It still provides some lubrication between the tip and film/substrate, where the COF rises from 0.10 to 0.14 for DLC and 0.9 to 0.18 for DLC/TiO_2.

Figure 31, 32 and 33 shows micrographs of scratch tests that were conducted on DLC and DLC/TiO_2-film samples on AISI 316L substrate using a Rockwell C indenter, in conjunction with the analysis of the friction coefficient (COF) and normal force curves.

Figure 31 depicts the results for DLC after 204 hours; Figure 32 shows the results for DLC after 408 hours; Figure 33 shows the results for DLC/TiO_2 after 408 hours; and Figure 34 presents the comparison of average friction coefficient (COF) curves before and after UV exposure. Both films had a satisfactory performance in the Scratch Test, showing good adhesion to the substrate even though the DLC had a better performance when compared to DLC/TiO_2 film.

After 204 hours of the UV ageing test, the sample film with DLC exhibited the first critical load after a displacement of 2.4 mm, reaching a load force (Lc1) of 4.8 N. The adhesive failure between the film and the substrate was observed after a displacement of 3.5 mm, up to a load force (Lc2) of 7.4 N, and the COF rose from 0.08 to 0.26. As UV testing progressed, after 408 hours, the first critical load occurred after a displacement of 0.4 mm, and Lc1 decreased to 1.25 N.

The second critical load (Lc2) appeared after 2.2 mm of displacement with a load of 5 N, and the COF increased from 0.15 to 0.24. For DLC/TiO_2-film samples, after 408 hours of UV testing exposure, the first critical load occurred after a displacement of 2.0 mm, reaching a critical load (Lc1) of 4.9 N. The second critical load appeared after 3.9 mm of displacement, up to a load of 7.5 N, and the COF varied from 0.10 to 0.21. It became evident that all films experienced degradation in wear resistance and lubrication capacity.

Table 9 presents a summary of friction coefficient (COF) for the control samples and those coated with DLC and DLC/TiO_2 after 408 hours of UV exposure. When

comparing the COF for each type of sample with its respective control, an increase in the coefficient of friction is observed. However, this increase is significantly more pronounced for the sample with the DLC film, which shows a maximum COF, rising from 0.14 to 0.24. In contrast, the DLC/TiO_2 sample exhibits a more modest increase with a maximum COF value increasing from 0.18 to 0.19.

Figure 31 – Micrograph of scratch test conducted on DLC-film sample on AISI 316L substrate after 204 hours of UV ageing testing using a Rockwell C indenter in conjunction with the analysis of the friction coefficient (COF) and normal force curves.

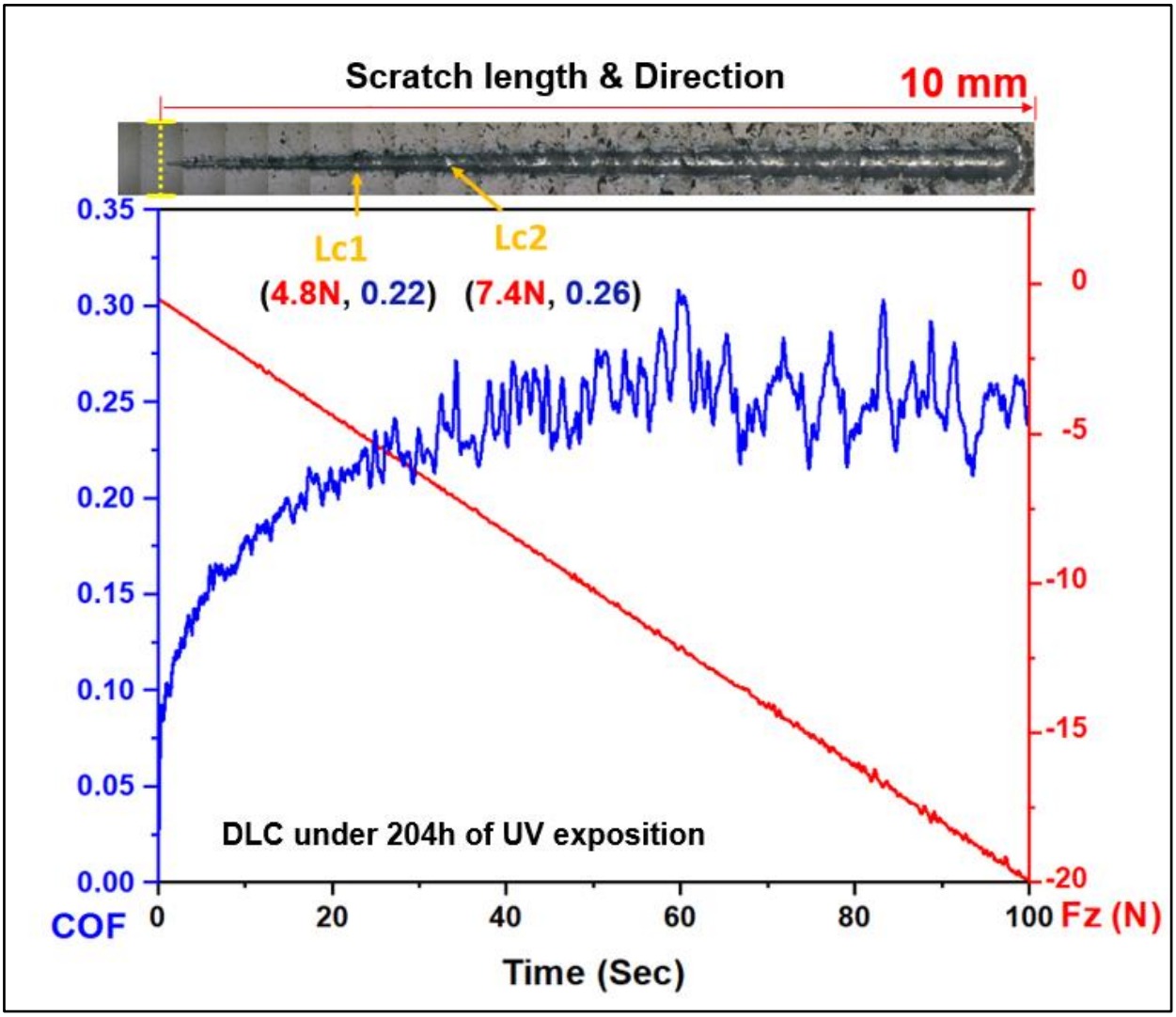

Source: Author.

Figure 32 – Micrograph of scratch test conducted on DLC-film sample on AISI 316L substrate after 408 hours of UV ageing testing using a Rockwell C indenter in conjunction with the analysis of the friction coefficient (COF) and normal force curves.

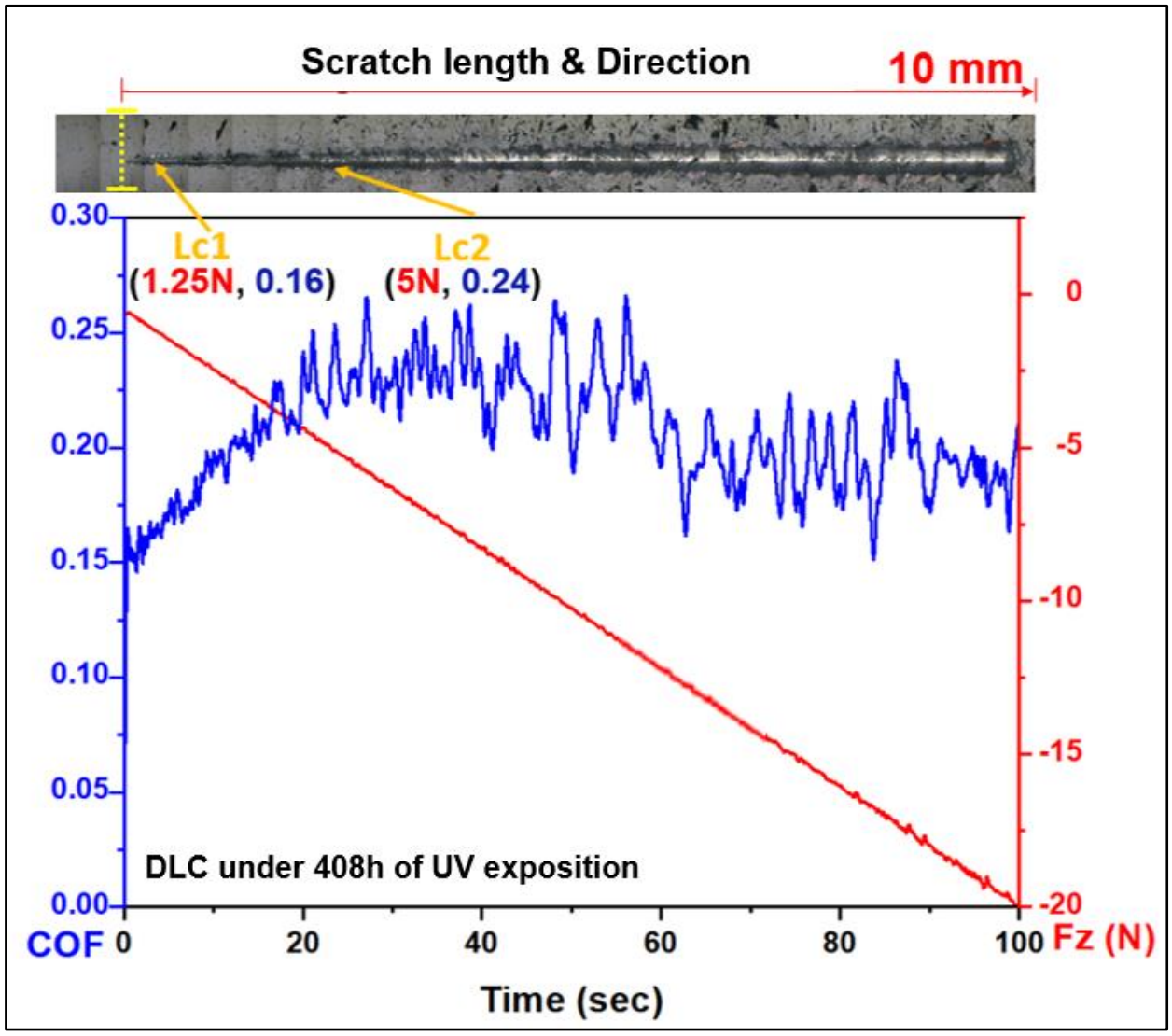

Source: Author.

The scratch test revealed a reduction in both displacement and force required to initiate failure modes, leading to a faster depletion of the lubrication capacity of the coatings. This effect was especially pronounced in the DLC-film specimens, potentially indicating the graphitization of the DLC layer due to UV radiation exposure. Graphitization reduces wear resistance and accelerates the peeling off the coating, resulting in an increased coefficient of friction (COF). However, the presence of the TiO_2 layer in the

DLC/TiO_2 films provided additional protection, helping to mitigate these effects by enhancing UV resistance and wear performance, as evidenced by the improved durability of these coatings under testing conditions.

Figure 33 – Micrograph of scratch test conducted on DLC/TiO_2-film sample on AISI 316L substrate after 408 hours of UV ageing testing using a Rockwell C indenter in conjunction with the analysis of the friction coefficient (COF) and normal force curves.

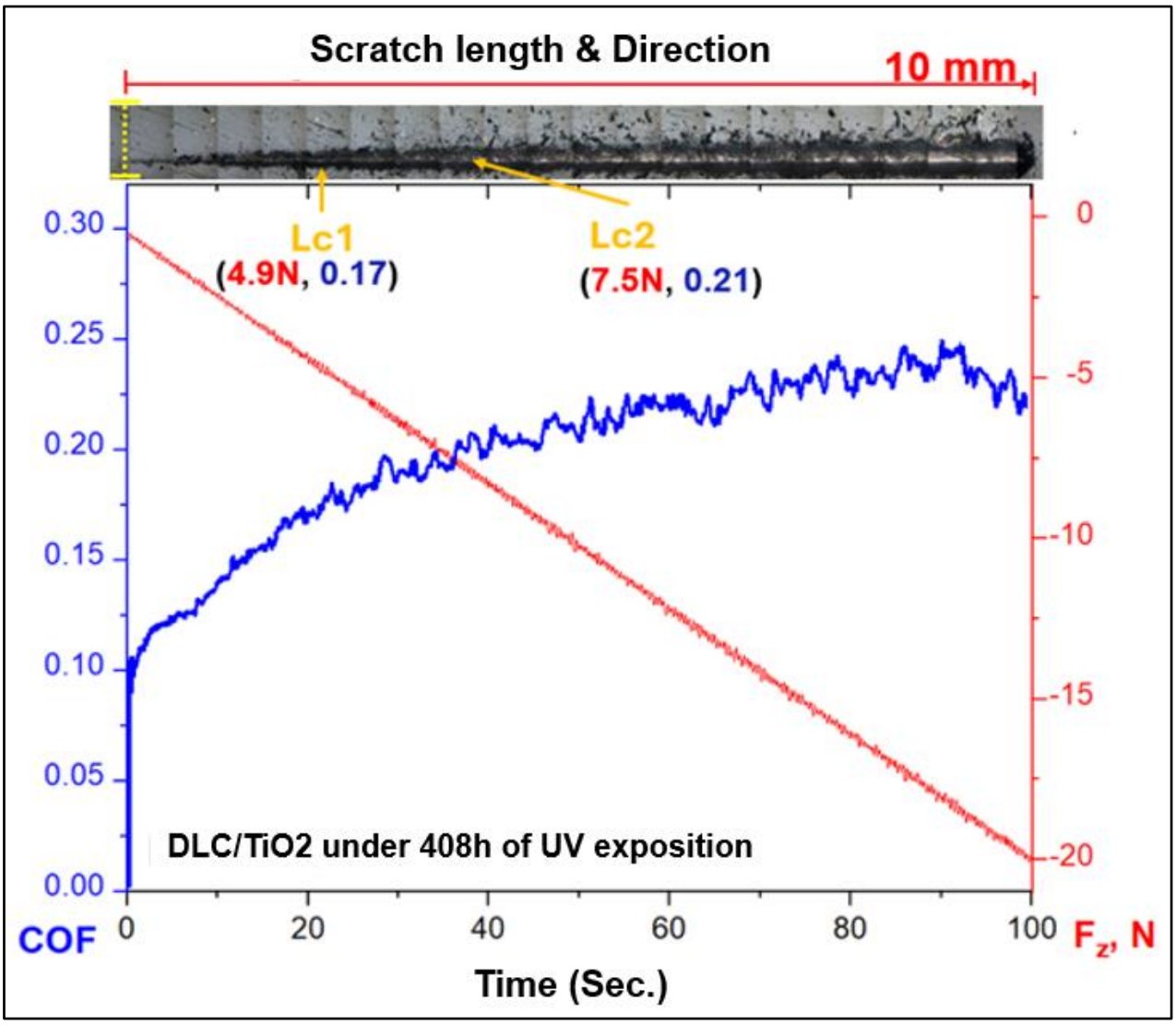

Source: Author.

Table 9 – Summary of friction coefficient [COF] among samples before and after UV ageing test.

	Friction coefficient [COF]				
Sample Type	**Mean**	**Minimum**	**Median**	**Maximum**	**Standard Deviation**
DLC/TiO_2 [408h]	0.15	0.022	0.16	0.19	0.030
DLC/TiO_2 [control]	0.14	0.016	0.14	0.18	0.032
DLC [408h]	0.19	0.042	0.20	0.24	0.034
DLC [control]	0.11	0.024	0.10	0.14	0.022

Source: Author.

Figure 34 – Comparison of average friction coefficient (COF) curves following UV ageing testing.

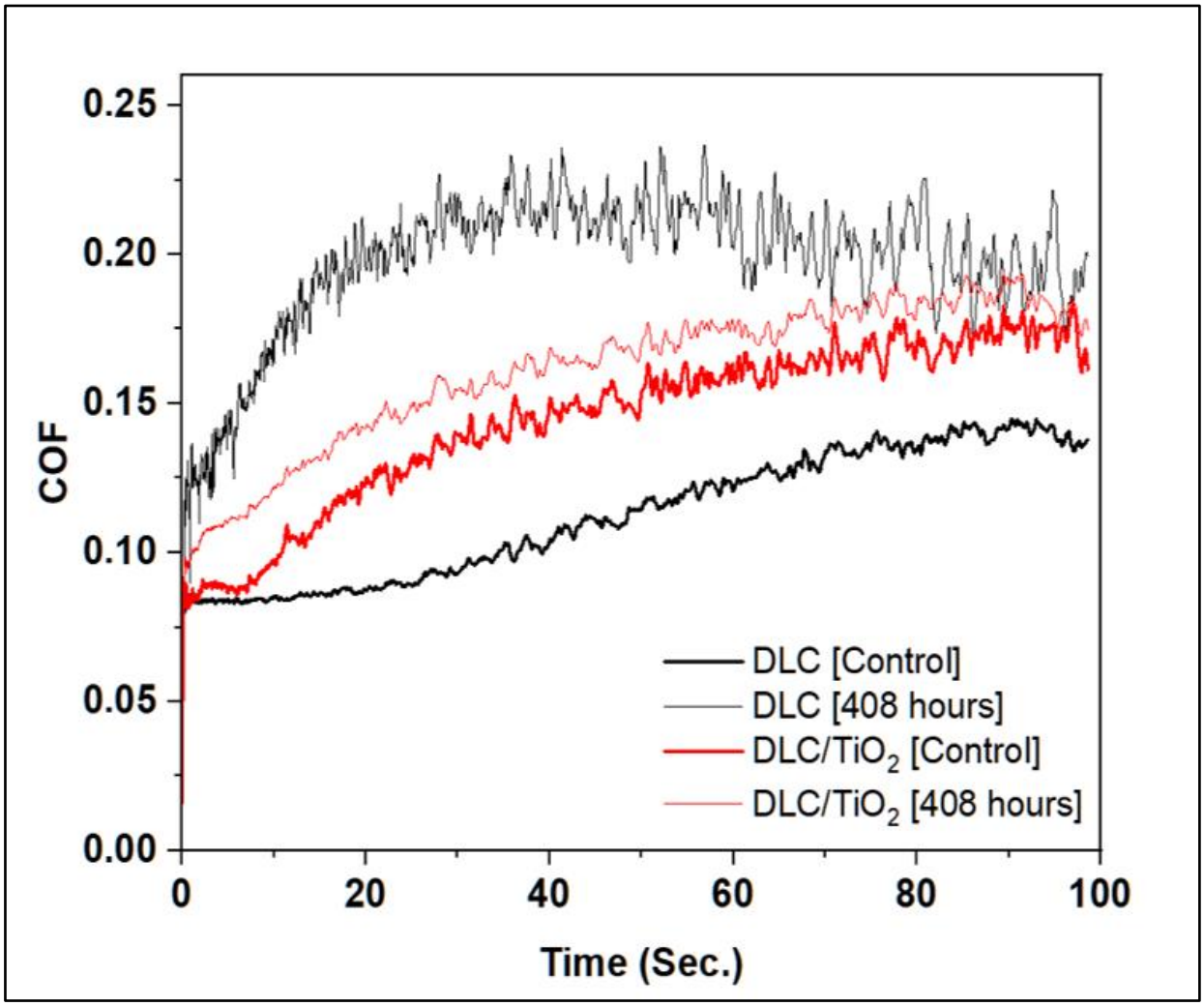

Source: Author.

5.5 HARDNESS AND ELASTIC MODULUS

Nanometer-scale resolution indentation experiments were conducted on DLC and DLC/TiO_2 specimens both before and after the UV ageing test. This test is essential for determining the mechanical properties of DLC films, given that hardness and elastic modulus significantly influence friction and wear [126]. Therefore, a comprehensive understanding of these properties is crucial for gaining insights into tribological behavior and UV film degradation.

Hardness is quantified as the maximum load applied during indentation divided by the projected contact area, while Young's modulus is derived from the slope of the unloading P-h curves [154,155]. To mitigate substrate influences, both hardness and Young's modulus were assessed at an indenter penetration depth constituting less than 10% of the film's thickness [154]. The Figure 35 shows the indenter penetration representation on DLC/TiO_2-coated film.

Figure 35 – Indenter Penetration representation on DLC/TiO_2-coated film.

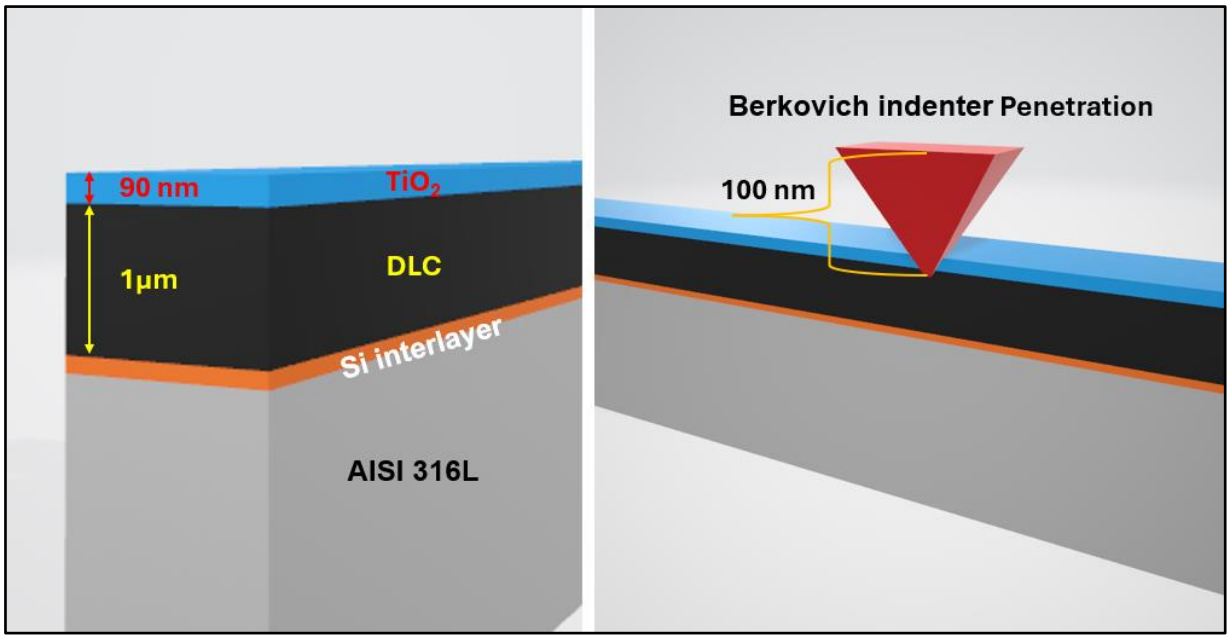

Source: Author.

The measurements were taken at 10 different points, and the average value obtained was computed. The test results summary and literature references are displayed in Table 10 and Figure 36 show the Force-displacement and Pd/FN curves for DLC and DLC/TiO_2-coated samples on AISI 316L substrate before UV aging test and Figure 37 shows the curves after 408 hours of UV exposition.

Table 10 – Average hardness and elastic modulus of DLC and DLC/TiO_2-film samples on AISI 316L substrate.

	DLC [Control]	**DLC [204 hours]**	**DLC [408 hours]**	**DLC/TiO_2 [Control]**	**DLC/TiO_2 [204 hours]**	**DLC/TiO_2 [408 hours]**	**Literature a-C:H**
Hardness (GPa)	26.29	18.10	19.38	12.80	10.58	9.9	7 - 30
Standard Deviation	1.5	2.3	1.6	2.1	0.8	1.3	
Elastic Modulus (GPa)	204.21	183.17	189.54	191.93	198.82	229.08	60 - 210
Standard Deviation	10.1	13.4	12.9	26.9	16	36.5	
H/E ratio	0.13	0.1	0.1	0.07	0.053	0.043	0.1 - 0.16
References							[126,154,155,156,157]

Hardness (H), Young's modulus (E), and H/E ratio of DLC films, a = amorphous.
Very soft DLC: Below 5 GPa; Soft DLC: 5 - 10 GPa; Moderate DLC: 10 - 20 GPa;
Hard DLC:20 - 40 GPa; Very hard DLC: Above 40 GPa

Source: Author.

A notable distinction in hardness is observed between the DLC and DLC/TiO_2 controlled samples. Specifically, the DLC/TiO_2 sample exhibits a significant reduction in hardness compared to its DLC counterpart, with the reduction in hardness being approximately 50%. This phenomenon may be attributed to the TiO_2 deposition process, which requires the use of pure water as a precursor and operates under thermal conditions (at 200°C) within the ALD reactor cycle.

The deposition process, lasting approximately one hour and 30 minutes, is followed by 3 hours of gradual cooling, which likely contributes to the decrease in hardness. During this process, the presence of hydrogen, coupled with the elevated temperature of 200°C,

facilitates hydrogen diffusion within the film structure. Consequently, this increase in hydrogen content contributes to the diminished hardness and Young's modulus [126].

The hardness discrepancy between DLC and DLC/TiO_2 samples underscores the importance of considering deposition parameters and their effects on the resulting material characteristics.

Figure 36 – Force-displacement and Pd/FN curves for control samples prior to UV exposure. (a) Force-displacement curves for DLC samples; (b) Pd/FN curves for DLC samples; (c) Force-displacement curves for DLC/TiO_2 samples; (d) Pd/FN curves for DLC/TiO_2 samples.

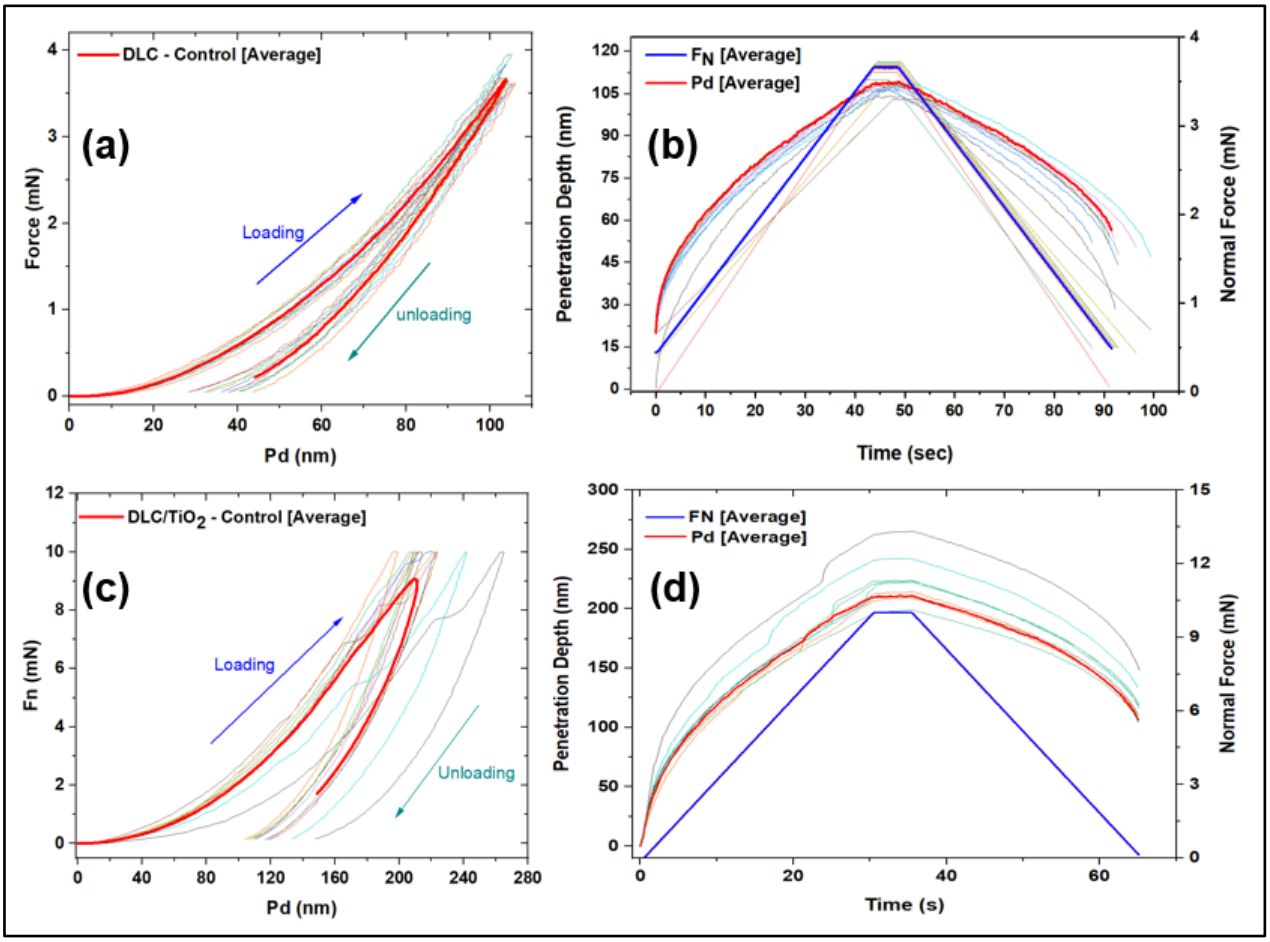

Source: Author.

Figure 37 – Force-displacement and Pd/FN curves for DLC and DLC/TiO2 samples after 408 hours of UV exposure. (a) Force-displacement curves for DLC samples; (b) Pd/FN curves for DLC samples; (c) Force-displacement curves for DLC/TiO_2 samples; (d) Pd/FN curves for DLC/TiO_2 samples.

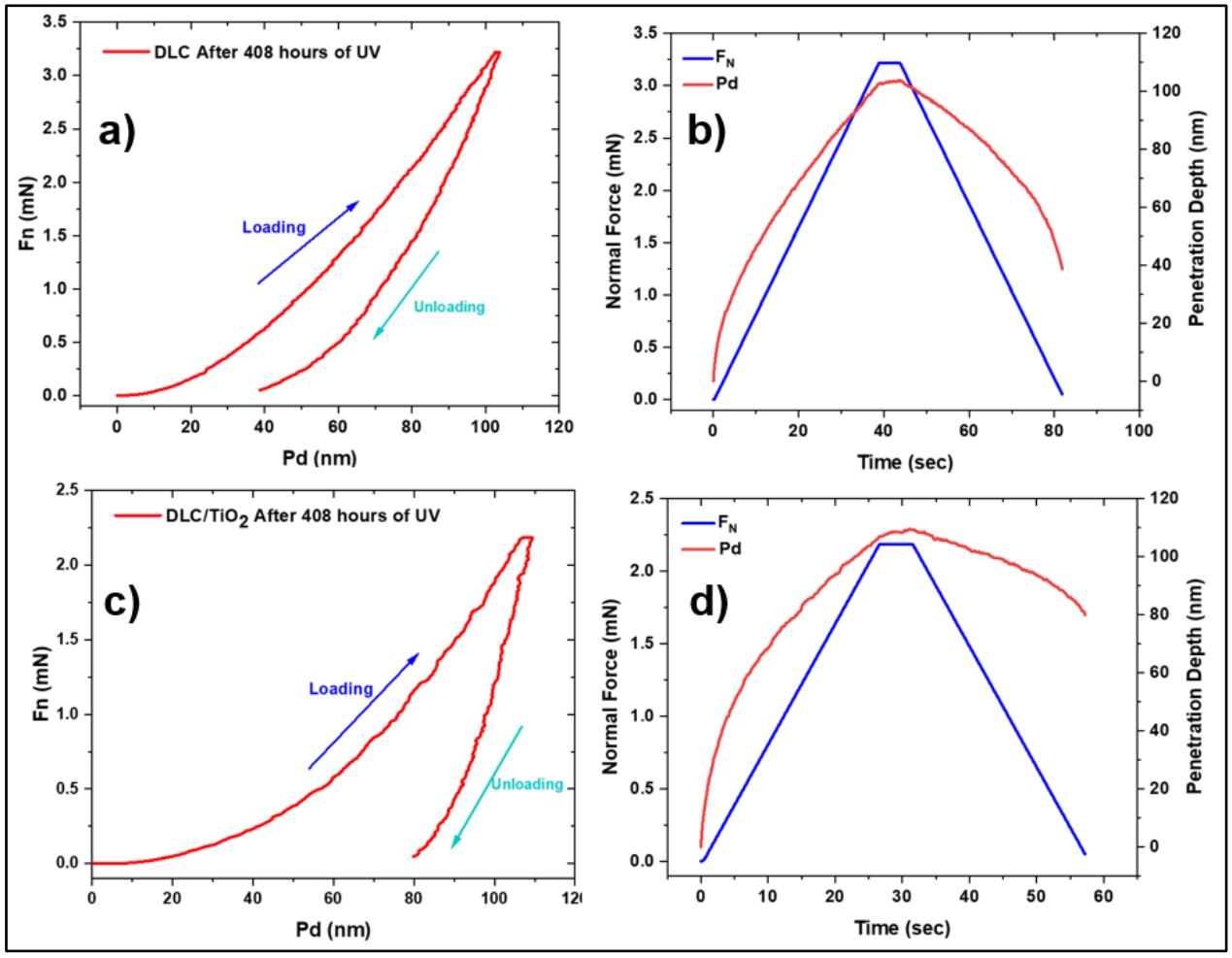

Source: Author.

5.6 SALT SPRAY TEST AND POROSITY ASSESSMENT RESULTS

The porosity test was conducted on the samples both before and after the salt spray test to check for any pre-existing flaws or defects in the film and to determine if there was exposure of the substrate to the saline solution after the test. This would indicate a breach or penetration of the protective film by the corrosive agent.

It was identified through the porosity test on one of the DLC samples, during the pre-test evaluation, that there was a defect/flaw in the film at the edge of the sample. As shown in Figure 38, the sample exhibited a blue mark where it came into contact with the substrate.

Figure 38 – Identification of film defects and substrate exposure via porosity test on samples before Salt Spray Test.

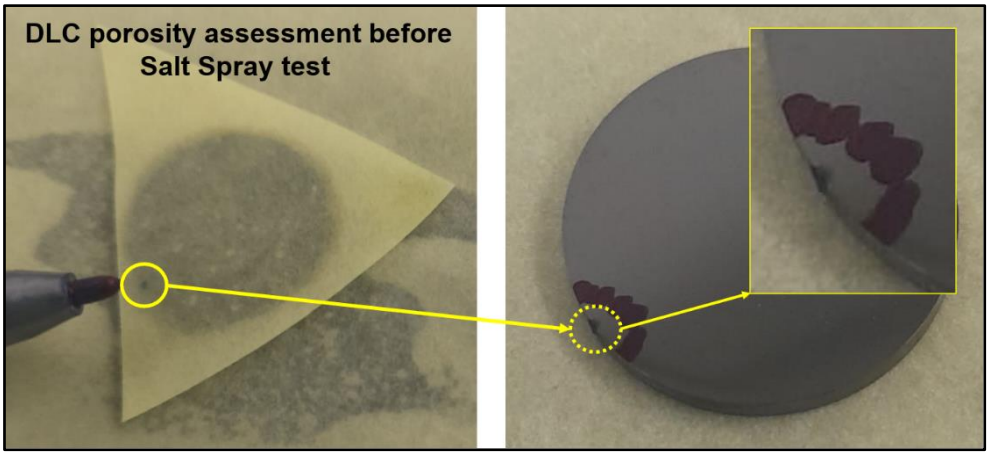

Source: Author.

Figure 39 shows the SEM analysis of the 316L stainless steel samples coated with a DLC and a DLC/TiO_2 films before the salt spray test and porosity analysis. As can be seen, the DLC sample exhibited a smooth and defect-free surface. Conversely, the sample with the DLC/TiO_2 film showed the presence of some pores and defects.

Figure 40 presents the SEM surface analysis of tested samples after 648 hours of the Salt Spray test at magnifications of 1000x and 5000x. Figure 40(1) shows the results for DLC-coated samples, where no signs of corrosion were identified in the investigated areas. Figure 40(2) displays the results for DLC/TiO_2-coated samples, where a few points of delamination of TiO_2 layer over the film were observed due adhesive and cohesive failure without apparent corrosion points.

Some of the possible causes for the presence of delamination spots on the surfaces of DLC/TiO_2-coated samples after testing are: (1) pre-existing spots of non-uniform growth of the TiO2 layer, resulting in surface irregularities between the DLC and TiO_2 layers, may have caused poor adhesion of the coating at these points, contributing to the appearance

of these failures; (2) dust residues, debris, and pores in the films may have promoted the formation of corrosion nuclei or delamination [158,159]; (3) attack of the solution/environment through cavities, cracks, holes, and fissures due to the TiO_2 thin film thickness [160].

Figure 39 – SEM images (1000× and 5000× magnification) from the surface of DLC and DLC/TiO_2-coated 316L stainless steel before porosity evaluation and salt spray test.

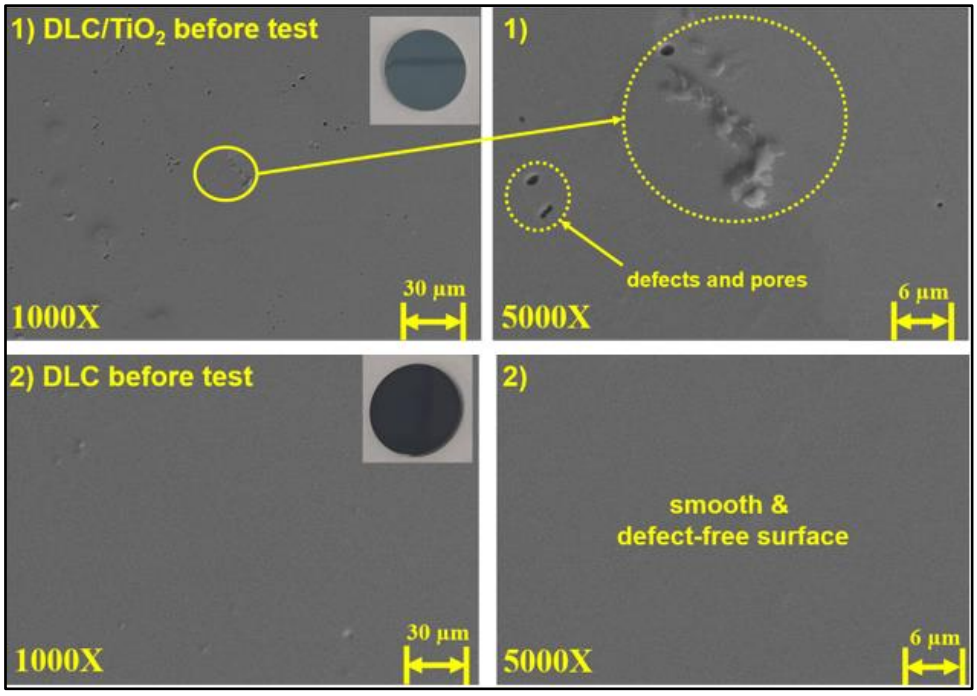

Source: Author.

Figure 40(3) shows the test result for the bare 316L stainless steel specimen. As can be observed, there is extensive corrosion formation throughout the sample area. The corroded surface exhibits several tiny pits combine with spalling corrosion [110]. It is important to note that the first signs of corrosion formation on bare samples began to appear after 24 hours of the salt spray test.

Figure 40 – Comparison of test results after 648 hours of salt spray testing, with the chamber temperature maintained at 34.7 ºC. (1) DLC-coated 316L stainless steel; (2) DLC/TiO_2-coated 316L stainless steel; (3) Bare 316L stainless steel.

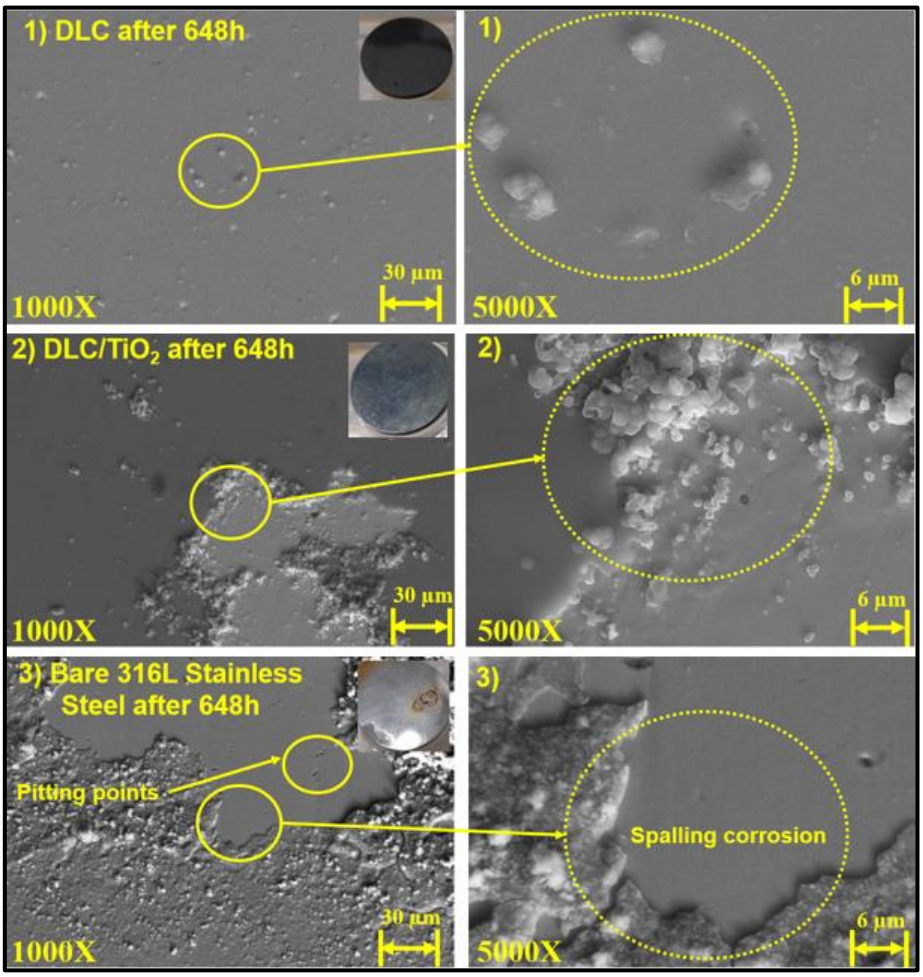

Source: Author.

Figure 41 presents the results of the porosity assessment for both DLC and DLC/TiO_2-coated samples before the salt spray test. Neither coating exhibited blue marks or signs of substrate exposure to the corrosive environment. Despite the identification by SEM analysis of few points of delamination in the TiO_2 layer over the DLC/TiO_2 film, due to adhesive and cohesive failure, no evidence of iron contamination from corrosion products—such as iron dust, deposits, or oxides—was detected, confirming that the substrate was not exposed to corrosion.

Figure 41 – Porosity assessment using the Ferroxyl test for free iron on DLC and DLC/TiO_2-coated 316L stainless steel substrates after the salt spray test.

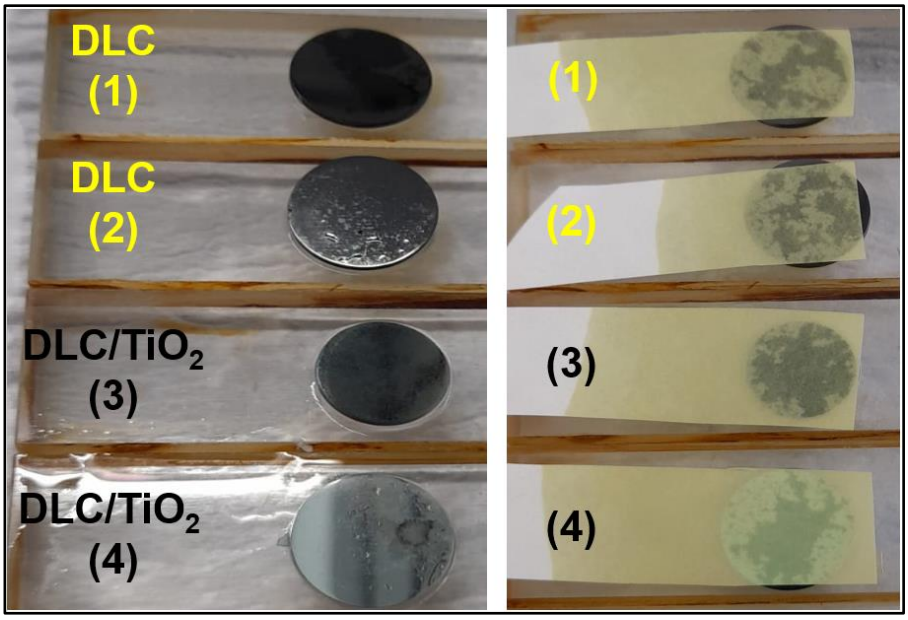

Source: Author.

Qualitatively, both coatings demonstrated excellent resilience to corrosion in the saline environment. While the DLC/TiO_2 film did not perform as well as the pure DLC coating in terms of corrosion resistance, the additional TiO_2 layer still enhanced the system's overall durability by providing an extra protective barrier to DLC. In contrast, the untreated 316L stainless steel samples exhibited localized pitting and spalling corrosion.

6 CONCLUSIONS

In this study, DLC and DLC/TiO_2 thin films were deposited onto a 316L stainless steel substrate using a combination of PECVD and ALD techniques. The effects of accelerated ageing, induced by UV exposure, on the properties of the films, were evaluated using an Accelerated Weathering Tester, following ASTM G154 practices. This assessment aimed to simulate the impact of sunlight and moisture (rain or dew) on the films under real-world conditions. Raman spectra analysis was conducted to determine and compare film characteristics before and after 204 and 408 hours of testing, including carbon phase bands, D and G band displacement, characteristic bandwidths, and the I_D/I_G ratio analyses.

UV ageing tests significantly impact the Raman spectrum of DLC films, leading to structural deterioration in the specimens. However, in samples with DLC/TiO_2 film, there was notable preservation of the Raman spectra signature after 204 and 408 hours of testing when compared to the control sample. SEM analysis revealed no signs of cracking or delamination in the samples, although slight alterations in the color pattern were observed.

The adhesion of the films was evaluated using a scratching test following ASTM C1624 standards. Both DLC and DLC/TiO_2 films exhibited satisfactory performance both before and after the test, indicating good adhesion to the substrate. However, it's noteworthy that a progressive degradation in resistance to wear and lubrication capacity was observed in both types of films after the UV ageing test. The scratch test revealed a reduction in scratch length and the force required to initiate failure modes and an increase in COF, suggesting a quicker depletion of the film. This depletion was particularly notable in DLC-film specimens, potentially indicating the graphitization of the DLC layer due to UV radiation exposure. Graphitization reduces wear resistance and accelerates the peeling off the coating, resulting in an increased coefficient of friction (COF). However, the presence of the TiO_2 layer in the DLC/TiO_2 films provided additional protection, helping to mitigate these effects by enhancing UV resistance and wear performance, as evidenced by the improved durability of these coatings under the same testing conditions.

The hardness of DLC specimens was found to decrease after UV ageing tests (approximately 30% for DLC and 22% for DLC/TiO_2-coated films). Furthermore, it was noted that the TiO_2 coating process significantly diminishes the hardness of the DLC film compared to DLC samples without TiO_2 (reduction of approximately 50%). This reduction was more pronounced than the decrease resulting from UV ageing tests on DLC samples without the TiO_2 layer. These findings emphasize the importance of thoroughly evaluating the effects of deposition processes and parameters on material characteristics.

Therefore, in applications where hardness is crucial, careful consideration should be given to utilizing this process, or alternative TiO_2 deposition methods that do not compromise this property should be explored. Nonetheless, despite the hardness effect caused by the TiO_2 deposition process, the TiO_2 layer demonstrated its effectiveness in mitigating potential UV-induced damage in the DLC film structure.

Additionally, the results of assessments of the films' behavior in marine atmospheric conditions showed that the DLC and DLC/TiO_2-coated films exhibited significantly enhanced corrosion resistance compared to the bare 316L stainless steel, maintaining the integrity of the coating even under prolonged exposure to corrosive environments. This is crucial for applications in marine and coastal environments where exposure to saltwater can severely compromise material performance. The results underscore the potential of PECVD and ALD techniques in producing high-performance coatings for demanding environments, particularly when combined with protective layers like TiO_2. This study contributes significantly to the advancement of durable protective coatings for aerospace and other industries, highlighting the importance of tailored deposition techniques and thorough material characterization.

7 FUTURE WORK

Future research will focus on several key areas to further understand and enhance the performance of the DLC/TiO_2 films in advanced applications. One important direction is to investigate the behavior of the DLC/TiO_2 films in environments rich in atomic oxygen, which will simulate conditions like those found in low Earth orbit. Additionally, studying the film's response to thermal cycling will provide insights into its durability under fluctuating temperatures, a critical factor for aerospace applications.

To further simulate aerospace environmental conditions, vibration testing will be conducted to evaluate the mechanical stability of the films under dynamic stresses. Another critical avenue of exploration will be the combined effect of UV radiation on the corrosion resistance of DLC/TiO_2 films in marine environments, aiming to understand how UV exposure influences long-term performance.

Finally, ongoing efforts will explore methods to mitigate the reduction in hardness observed in DLC/TiO_2 films, seeking to maintain or enhance their mechanical properties without compromising other functional characteristics. These investigations will contribute to optimizing the films for more demanding operational conditions, expanding their potential applications in both terrestrial and space environments.

REFERENCES

[1] RAJAK, D. K. *et al.* Diamond-Like Carbon (DLC) Coatings : Classification , Properties , and Applications. **Applied Sciences**, v. 11, n. 10, p. 4445, 2021a.

[2] LIU, X. *et al.* Surface composition variation and high-vacuum performance of DLC/ILs solid-liquid lubricating coatings: Influence of space irradiation. **Applied Surface Science**, v. 258, n. 20, p. 8289–8297, 2012b.

[3] WU, Y. *et al.* Effect of vacuum annealing on the microstructure and tribological behavior of hydrogenated amorphous carbon films prepared by magnetron sputtering. **Proceedings of the Institution of Mechanical Engineers, Part J: Journal of Engineering Tribology**, v. 227, n. 7, p. 729–737, 2013c.

[4] RAO, J.; LAWSON, K. J.; NICHOLLS, J. R. The characterisation of e-beam evaporated and magnetron sputtered carbon films fabricated for atomic oxygen sensors. **Surface and Coatings Technology**, v. 197, n. 2–3, p. 154–160, 2005d.

[5] ADLIENE, D.; LAURIKAITIENE, J.; TAMULEVIČIUS, S. Modification of amorphous DLC films induced by MeV photon irradiation. **Nuclear Instruments and Methods in Physics Research, Section B: Beam Interactions with Materials and Atoms**, v. 266, n. 12–13, p. 2788–2792, 2008e.

[6] VANKAR, V. D.; DILAWAR, N. Ion irradiation effects in diamond and diamond like carbon thin films. **Vacuum**, v. 47, n. 11, p. 1275–1280, 1996f.

[7] SHAN, C. X.; HOU, X.; CHOY, K. L. Corrosion resistance of TiO2 films grown on stainless steel by atomic layer deposition. **Surface and Coatings Technology**, v. 202, n. 11, p. 2399–2402, 2008g.

[8] MOHR, L. C. *et al.* Titanium dioxide nanoparticles applied as ultraviolet radiation blocker in the polylactic acid bidegradable polymer. **Polymer Testing**, v. 77, n. April, p. 105867, 2019h.

[9] HANAOR, D. A. H.; SORRELL, C. C. Review of the anatase to rutile phase transformation. **Journal of Materials Science**, v. 46, n. 4, p. 855–874, 2011i.

[10] WENG, K. W.; HUANG, Y. P. Preparation of TiO2 thin films on glass surfaces with self-cleaning characteristics for solar concentrators. **Surface and Coatings Technology**, v. 231, p. 201–204, 2013j.

[11] MATĚJOVÁ, L. *et al.* Microstructure, optical and photocatalytic properties of TiO2 thin films prepared by chelating-agent assisted sol-gel method. **Journal of Nanoscience and Nanotechnology**, v. 16, n. 1, p. 504–514, 2016k.

[12] COLMENARES, J. C. *et al.* Nanostructured photocatalysts and their applications in the photocatalytic transformation of lignocellulosic biomass: An overview. **Materials**, v. 2, n. 4, p. 2228–2258, 2009l.

[13] CAPOTE, A. *et al.* Effect of low-pressure deposition on the mechanical and tribological properties of a-C:H films deposited via modified pulsed-DC PECVD with active screen as an additional cathode. **Surface and Coatings Technology**, v. 445, n. April, p. 128716, 2022m.

[14] ZHENG, J.; LIU, Q.; LI, Z. Effect of negative bias voltage on properties of hydrogenated diamond-like carbon films. **Guangxue Jingmi Gongcheng/Optics and Precision Engineering**, v. 30, n. 4, p. 411–420, 2022n.

[15] LIU, Z. *et al.* Simultaneous deposition of DLC film on the internal surface of multiple pipes. **Diamond and Related Materials**, v. 127, n. March, p. 109187, 2022o.

[16] **Zephyr HAPS**. Disponível em: <https://www.aaltohaps.com/Zephyr-HAPS>. Acesso em: 27 set. 2024p.

[17] PAN, J. *et al.* Effect of UV Irradiation on the Alternating Wet and Dry Corrosion Behavior of Galvanized Steel in Sodium Chloride Solution. **Crystals**, v. 13, n. 8, 2023q.

[18] SHEN, Y. *et al.* Enhanced Anti-Tribocorrosion Performance of Ti-DLC Coatings Deposited by Filtered Cathodic Vacuum Arc with the Optimization of Bias Voltage. **Coatings**, v. 12, n. 5, 2022r.

[19] SWISSDRONES. **Long-range VTOL capabilityfor critical unmanned missions**. Zurich: SwissDrones, 2023. Disponível em: https://www.swissdrones.com/. Acesso em: 27 set. 2024s.

[20] ROBERTSON, J. Diamond-like amorphous carbon. **Materials Science and Engineering: R: Reports**, v. 37, n. 4–6, p. 129–281, 2002t.

[21] SENGUPTA, R. *et al.* A review on the mechanical and electrical properties of graphite and modified graphite reinforced polymer composites. **Progress in Polymer Science (Oxford)**, v. 36, n. 5, p. 638–670, 2011u.

[22] PIERSON, H. O. Handbook of Carbon, Graphite, Diamonds and Fullerenes. **Noyes Publications**, p. 43–69, 1993v.

[23] GRILL, A. Electrical and optical properties of diamond-like carbon. **Thin Solid Films**, v. 355–356, p. 189–193, nov. 1999w.

[24] GRILL, A. Tribology of diamondlike carbon and related materials: An updated review. **Surface and Coatings Technology**, 1997x.

[25] YU, Q. *et al.* Influence Factors on Mechanisms of Superlubricity in DLC Films: A Review. **Frontiers in Mechanical Engineering**, v. 6, n. August, p. 1–17, 2020y.

[26] SPAHR, M. E. *et al.* Development of carbon conductive additives for advanced lithium ion batteries. **Journal of Power Sources**, v. 196, n. 7, p. 3404–3413, 2011z.

[27] HOLMBERG, K.; MATTHEWS, A.; RONKAINEN, H. Coatings tribology - Contact mechanisms and surface design. **Tribology International**, v. 31, n. 1–3, p. 107–120, 1998aa.

[28] ERDEMIR, A.; DONNET, C. **Tribology of diamond-like carbon films: Recent progress and future prospectsJournal of Physics D: Applied Physics**, 2006ab.

[29] RODRIGUEZ, B. J. *et al.* An alternative approach to the tribological analysis of Si-doped DLC coatings deposited with different bias voltages using Raman spectroscopy mapping. **Emergent Materials**, v. 4, n. 6, p. 1595–1604, 2021ac.

[30] OHTAKE, N. *et al.* Properties and classification of diamond-like carbon films. **Materials**, v. 14, n. 2, p. 1–26, 2021ad.

[31] ROBERTSON, J. Hard amorphous (diamond-like) carbons. **Progress in Solid State Chemistry**, v. 21, n. 4, p. 199–333, 1991ae.

[32] YANG, W. J. *et al.* Thermal stability evaluation of diamond-like nanocomposite coatings. **Thin Solid Films**, v. 434, n. 1–2, p. 49–54, 2003af.

[33] CAPOTE, G. *et al.* Adherent amorphous hydrogenated carbon films on metals deposited by plasma enhanced chemical vapor deposition. **Thin Solid Films**, v. 516, n. 12, p. 4011–4017, 2008ag.

[34] CLAUSING, R. E. *et al.* **Diamond and diamond-like films and coatings**. New

York: Plenum Press, 1991ah.

[35] FAYED, S. M. *et al.* Corrosion behavior and passive stability of multilayer DLC-Si coatings. **Surface and Coatings Technology**, v. 431, p. 128001, 2022ai.

[36] FERRARI, A. C.; ROBERTSON, J. Interpretation of Raman spectra of disordrred and amorphous carbon. **Surface and Coatings Technology**, v. 61, n. 4, p. 1–13, 2000aj.

[37] LIU, Y.; ERDEMIR, A.; MELETIS, E. I. An investigation of the relationship between graphitization and frictional behavior of DLC coatings. **Surface and Coatings Technology**, v. 86–87, n. PART 2, p. 564–568, 1996ak.

[38] ERDEMIR, A. The role of hydrogen in tribological properties of diamond-like carbon films. **Surface and Coatings Technology**, v. 146–147, p. 292–297, 2001al.

[39] KUMAR, D. D. *et al.* Tribological Properties of Carbon-Based Coatings. In: **Tribology and Characterization of Surface Coatings**. [s.l: s.n.]. p. 115–137.

[40] MOBARAK, H. M. *et al.* Tribological properties of amorphous hydrogenated (a-C:H) and hydrogen-free tetrahedral (ta-C) diamond-like carbon coatings under jatropha biodegradable lubricating oil at different temperatures. **Applied Surface Science**, v. 317, p. 581–592, 2014an.

[41] AL MAHMUD, K. A. H. *et al.* An updated overview of diamond-like carbon coating in tribology. **Critical Reviews in Solid State and Materials Sciences**, v. 40, n. 2, p. 90–118, 2015ao.

[42] SHARIFAHMADIAN, O. *et al.* Doping effects on the tribological performance of diamond-like carbon coatings: A review. **Journal of Materials Research and Technology**, v. 27, n. September, p. 7748–7765, 2023ap.

[43] GUO, C. Q. *et al.* Residual stress and tribological behavior of hydrogen-free Al-DLC films prepared by HiPIMS under different bias voltages. **Surface and Coatings Technology**, v. 445, n. February, p. 128713, 2022aq.

[44] CAPOTE, G. *et al.* Adherent diamond-like carbon coatings on metals via PECVD and IBAD. **Brazilian Journal of Physics**, v. 36, n. 3 B, p. 986–989, 2006ar.

[45] SÁNCHEZ-LÓPEZ, J. C.; FERNÁNDEZ, A. Doping and alloying effects on DLC coatings. **Tribology of Diamond-Like Carbon Films: Fundamentals and Applications**, n. Dlc, p. 311–328, 2008as.

[46] HILBERT, J. *et al.* Si doping enhances the thermal stability of diamond-like carbon through reductions in carbon-carbon bond length disorder. **Carbon**, v. 131, p. 72–78, 2018at.

[47] ZHANG, T. F. *et al.* Microstructure and high-temperature tribological properties of Si-doped hydrogenated diamond-like carbon films. **Applied Surface Science**, v. 435, p. 963–973, 2018au.

[48] PAPAKONSTANTINOU, P. *et al.* The effects of Si incorporation on the electrochemical and nanomechanical properties of DLC thin films. **Diamond and Related Materials**, v. 11, n. 3–6, p. 1074–1080, 2002av.

[49] LI, X. W. *et al.* Stress reduction of diamond-like carbon by Si incorporation: A molecular dynamics study. **Surface and Coatings Technology**, v. 228, n. SUPPL.1, p. S190–S193, 2013aw.

[50] HAN, Z. *et al.* Influence of Nitrogen Flow Rate on the Microstructure and Properties of N and Me (Me=Cr, Zr) Co-doped Diamond-like Carbon Films. **Journal of Materials Science and Technology**, v. 26, n. 11, p. 967–972, 2010ax.

[51] LEAL, G. *et al.* Impact of high N2 flow ratio on the chemical and morphological characteristics of sputtered N-DLC films. **Surface and Interface Analysis**, v. 49, n. 2, p. 99–106, 2017ay.

[52] HSUEH, H. C.; WANG, Y. K.; LEE, S. The effect of ammonia/acetylene ratio on characteristics of amorphous carbon films prepared by plasma enhanced chemical vapor deposition. **Surface and Coatings Technology**, v. 231, p. 353–356, 2013az.

[53] MABUCHI, Y.; HIGUCHI, T.; WEIHNACHT, V. Effect of sp2/sp3 bonding ratio and nitrogen content on friction properties of hydrogen-free DLC coatings. **Tribology International**, v. 62, p. 130–140, 2013ba.

[54] SARRA-BOURNET, C. *et al.* Effect of C 2H 4/N 2 ratio in an atmospheric pressure dielectric barrier discharge on the plasma deposition of hydrogenated amorphous carbon-nitride films (a-C:N:H). **Plasma Chemistry and Plasma Processing**, v. 30, n. 2, p. 213–239, 2010bb.

[55] CHEN, T. *et al.* Achieving low friction and wear under various humidity conditions by co-doping nitrogen and silicon into diamond-like carbon films. **Thin Solid Films**, v. 638, p. 375–382, 2017bc.

[56] ZHOU, B. *et al.* Structure and optical properties of Cu-DLC composite films deposited by cathode arc with double-excitation source. **Diamond and Related Materials**, v. 69, p. 191–197, 2016bd.

[57] JASTRZĘBSKI, K. *et al.* Induced Biological Response in Contact with Ag-and Cu-Doped Carbon Coatings for Potential Orthopedic Applications. **Materials**, v. 14, n. 8, p. 1861, 9 abr. 2021be.

[58] BALESTRA, R. M. *et al.* Carbon-based coatings doped by copper: Tribological and mechanical behavior in olive oil lubrication. **Surface and Coatings Technology**, v. 205, n. SUPPL. 2, p. S79–S83, 2011bf.

[59] WANG, J. *et al.* Influence of structure evolution on tribological properties of fluorine-containing diamond-like carbon films: From fullerene-like to amorphous structures. **Applied Surface Science**, v. 457, p. 388–395, 2018bg.

[60] DONNET, C. Recent progress on the tribology of doped diamond-like and carbon alloy coatings: A review. **Surface and Coatings Technology**, v. 100–101, n. 1–3, p. 180–186, 1998bh.

[61] ZIA, A. W.; BIRKETT, M. Deposition of diamond-like carbon coatings: Conventional to non-conventional approaches for emerging markets. **Ceramics International**, v. 47, n. 20, p. 28075–28085, 2021bi.

[62] SCHLEBROWSKI, T. *et al.* Refinement of sustainable polybutylene adipate terephthalate (PBAT) with amorphous hydrogenated carbon films (a-C:H) Revealing Film Instabilities Influenced by a thickness-dependent change of sp2/sp3 ratio. **Materials**, v. 13, n. 5, p. 1–15, 2020bj.

[63] FAYED, S. M. *et al.* Effect of Bias Voltage on Characteristics of Multilayer Si-DLC Film Coated on AA6061 Aluminum Alloy. **Journal of Materials Engineering and Performance**, v. 30, n. 1, p. 743–759, 2021bk.

[64] VITELARU, C. *et al.* A strategy for alleviating micro arcing during HiPIMS deposition of DLC coatings. **Materials**, v. 13, n. 5, 2020bl.

[65] MALISZ, K.; ŚWIECZKO-ŻUREK, B.; SIONKOWSKA, A. Preparation and Characterization of Diamond-like Carbon Coatings for Biomedical Applications—A Review. **Materials**, v. 16, n. 9, p. 1–16, 2023bm.

[66] GHADAI, R. K. *et al.* PECVD process parameter optimization: towards increased hardness of diamond-like carbon thin films. **Materials and Manufacturing Processes**, v. 33, n. 16, p. 1905–1913, 2018bn.

[67] ROBERTSON, J. Amorphous carbon. **Current Opinion in Solid State and Materials Science**, v. 1, n. 4, p. 557–561, 1996bo.

[68] BORA, J. *et al.* A substrate constituent Na-catalyzed growth of carbon nanotubes on glass substrate by atmospheric pressure PECVD. **Applied Surface Science**, v. 648, p. 158988, 2024bp.

[69] BONETTI, L. F. *et al.* Adhesion studies of diamond-like carbon films deposited on Ti6Al4V substrate with a silicon interlayer. **Thin Solid Films**, v. 515, n. 1, p. 375–379, 2006bq.

[70] BRADLEY, R. M.; HARPER, J. M. E.; SMITH, D. A. Theory of thin-film orientation by ion bombardment during deposition. **Journal of Applied Physics**, v. 60, n. 12, p. 4160–4164, 1986br.

[71] MANOVA, D.; GERLACH, J. W.; MÄNDL, S. Thin film deposition using energetic ions. **Materials**, v. 3, n. 8, p. 4109–4141, 2010bs.

[72] HU, Y.; TSAI, H. L.; HUANG, C. L. Effect of brookite phase on the anatase-rutile transition in titania nanoparticles. **Journal of the European Ceramic Society**, v. 23, n. 5, p. 691–696, 2003bt.

[73] ZEDEK, R. *et al.* Effects of slight Fe (III)-doping on structural and optical properties of TiO2 nanoparticles. **Journal of Sol-Gel Science and Technology**, v. 100, n. 1, p. 44–54, 2021bu.

[74] PELAEZ, M. *et al.* A review on the visible light active titanium dioxide photocatalysts for environmental applications. **Applied Catalysis B: Environmental**, v. 125, p. 331–349, 2012bv.

[75] COSTA, A. C. F. M. *et al.* Síntese e caracterização de nanopartículas de TiO2. **Cerâmica**, v. 52, n. 324, p. 255–259, 2006bw.

[76] MIYOSHI, K. **Solid Lubricants and Coatings for Extreme Environments: State-of-the-Art Survey**. Cleveland: [s.n.]. Disponível em: <http://gltrs.grc.nasa.gov>.

[77] ABBAS, F.; BENSAHA, R. Effect of annealing time on structural and optical proprieties of mercury (Hg+2) doped TiO2 thin films elaborated by sol-gel method for future photo-catalytic application. **Optik**, v. 247, n. August, 2021by.

[78] WANG, Y.-H. *et al.* A Review on the Pathways of the Improved Structural Characteristics and Photocatalytic Performance of Titanium Dioxide (TiO2) Thin

Films Fabricated by the Magnetron-Sputtering Technique. **Catalysts**, v. 10, n. 6, p. 598, 27 maio 2020bz.

[79] EL-HAMSHARY, A. A. **Influence of reactive sputtering process parameters on the structure and properties of TiO2 thin films**. 2011. Dissertação (Meestrado) Rheinisch-Westfaelische Technische Hochschule Aachen (Germany). Fakultaet fuer Mathematik, Informatik und Naturwissenschaften, Germany, 2011ca.

[80] LIAQAT, M. A. *et al.* Effects of Ag doping on compact TiO2 thin films synthesized via one-step sol–gel route and deposited by spin coating technique. **Journal of Materials Science: Materials in Electronics**, v. 31, n. 9, p. 7172–7181, 2020cb.

[81] YANG, B. Applications of Titania Atomic Layer Deposition in the Biomedical Field and Recent Updates. **American Journal of Biomedical Science & Research**, v. 8, n. 6, p. 465–468, 2020cc.

[82] WU, Y. *et al.* Highly compact TiO2 layer for efficient hole-blocking in perovskite solar cells. **Applied Physics Express**, v. 7, n. 5, 2014cd.

[83] AGHAEE, M. *et al.* TiO2 thin film patterns prepared by chemical vapor deposition and atomic layer deposition using an atmospheric pressure microplasma printer. **Plasma Processes and Polymers**, v. 16, n. 12, p. 1–14, 2019ce.

[84] KIM, H.-M. *et al.* Atomic Layer Deposition for Nanoscale Oxide Semiconductor Thin Film Transistors: Review and Outlook. **International Journal of Extreme Manufacturing**, v. 5, n. 1, p. 012006, 2023cf.

[85] VAN DUIJN, J. Enacting atomic layer deposition, 1999-2001. In: **Fortunes of High-Tech: a History of Innovation at ASM International**. 2019. Doctoral Thesis, Maastricht University], Wilco, 2019cg.

[86] DE MEURECHY, N. *et al.* Surface wear in a custom manufactured temporomandibular joint prosthesis. **Journal of Biomedical Materials Research - Part B Applied Biomaterials**, v. 110, n. 6, p. 1425–1438, 2022ch.

[87] JING, P. P. *et al.* Mechanism of protein biofilm formation on Ag-DLC films prepared for application in joint implants. **Surface and Coatings Technology**, v. 422, n. June, 2021ci.

[88] RAMÍREZ, G. *et al.* Super-Hard DLC Coatings as an Alternative to Polycrystalline Diamond for Cutting Tools: Predictive Analysis of Aluminium Alloy Surface Quality. **Lubricants**, v. 10, n. 7, 2022cj.

[89] LEAL, G. *et al.* An Approach on the Use of Co-sputtered W-DLC Thin Films as Piezoresistive Sensing Materials. **Current Materials Science**, v. 15, n. 1, p. 3 – 9, 2022ck.

[90] LI, C. *et al.* Effects of Substrate Bias Voltage on Friction and Corrosion Behavior of Multilayer Ti-DLC Film on the Surface of 316L Stainless Steel. **Zhongguo Biaomian Gongcheng/China Surface Engineering**, v. 36, n. 1, p. 189 – 199, 2023cl.

[91] WICHER, B. *et al.* Design of thin DLC/TiO2 film interference coatings on glass screen protector using a neon–argon-based gas injection magnetron sputtering technique. **Diamond and Related Materials**, v. 123, n. September 2021, 2022cm.

[92] KRUSE, R.; HAGER, C.; EVANS, R. D. **Tribological coating wear and durability performance guideline for gear applications**. American Gear Manufacturers Association Fall Technical Meeting 2015, AGMA FTM 2015. **Anais**...2015cn. Disponível em: https://www.scopus.com/inward/record.uri?eid=2-s2.0-84978695271&partnerID=40&md5=c55993b60068d5e8265eabe59a6efa59

[93] MIYOSHI, K. Lubrication by Diamond and Diamondlike Carbon Coatings. **Tribology Transactions**, v. 120, p. 379–384, 1998co.

[94] ERDEMIR, A.; ERYILMAZ, O. L.; FENSKE, G. Synthesis of diamondlike carbon films with superlow friction and wear properties. **Journal of Vacuum Science & Technology A: Vacuum, Surfaces, and Films**, v. 18, n. 4, p. 1987–1992, 2000cp.

[95] HAUERT, R. DLC Films in Biomedical Applications. In: **Tribology of Diamond-Like Carbon Films**. Boston, MA: Springer US, 2008cq. p. 494–509.

[96] GARDINER, D. J. *et al.* Introduction to Raman Scattering. In: **Practical Raman Spectroscopy**. NewYork: Springer-Verlag, 1989cr. p. 1–160.

[97] HOLLER, F. J. **Princípios de análise instrumental**. Porto Alegre: Bookman, 2009cs.

[98] FERRARI, A. C.; ROBERTSON, J. Resonant Raman spectroscopy of disordered, amorphous, and diamondlike carbon. **Physical Review B**, v. 64, n. 7, p. 1–13, 26 jul. 2001ct.

[99] FERRARI, A. C.; ROBERTSON, J. Raman spectroscopy of amorphous, nanostructured, diamond{\textendash}like carbon, and nanodiamond. **Philos. Trans. R. Soc., A**, v. 362, n. 1824, p. 2477–2512, 2004cu.

[100] CHANG, H.; HUANG, P. J. Thermo-Raman Studies on Anatase and Rutile. **Journal of Raman Spectroscopy**, v. 29, n. 2, p. 97–102, 1998cv.

[101] FERRARI, A. C.; ROBERTSON, J. Interpretation of Raman spectra of disordered and amorphous carbon. v. 61, n. 20, p. 95–107, 2000cw.

[102] ASTM-INTERNATIONAL. Astm C1624-05 - Standard Test Method for Adhesion Strength and Mechanical Failure Modes of Ceramic Coatings by Quantitative Single Point Scratch Testing. [*S. l.*]: ASTM International, 2005cx.

[103] VIEIRA, L. *et al.* Surface & Coatings Technology Scratch testing for micro- and nanoscale evaluation of tribocharging in DLC fi lms containing silver nanoparticles using AFM and KPFM techniques. **Surface and Coatings Technology**, v. 260, p. 205–213, dez. 2014cy.

[104] ANTUNES, R. A. **Caracterização do comportamento frente à corrosão de um aço inoxidável austenítico para aplicações biomédicas com revestimentos PVD de TiN, TiCN e DLC.** 2006. Tese (Doutorado em Tecnologia Nuclear - Materiais) - Instituto de Pesquisas Energéticas e Nucleares, University of São Paulo, São Paulo, 2006cz. doi:10.11606/T.85.2006.tde-30052007-161859**.**

[105] BULL, S. J. Failure mode maps in the thin film scratch adhesion test. **Tribology International**, v. 30, n. 7, p. 491-498, 1997da.

[106] OLIVER, W. C.; PHARR, G. M. An improved technique for determining hardness and elastic modulus using load and displacement sensing indentation experiments. **Journal of Materials Research**, v. 7, n. 6, p. 1564–1583, jun. 1992db.

[107] ZHU, P. *et al.* Toward accurate evaluation of bulk hardness from nanoindentation testing at low indent depths. **Materials and Design**, v. 213, p. 110317, 2022dc.

[108] PHARR, G. M.; HERBERT, E. G.; GAO, Y. The indentation size effect: A critical examination of experimental observations and mechanistic interpretations. **Annual Review of Materials Research**, v. 40, p. 271–292, 2010dd.

[109] NIX, W. D.; GAO, H. Indentation size effects in crystalline materials: A law for strain gradient plasticity. **Journal of the Mechanics and Physics of Solids**, v. 46, n. 3, p. 411–425, 1998de.

[110] GENTIL, V. **Corrosão**. Rio de Janeiro, RJ: Guanabara Dois, 1982.

[111] GENTIL, V. **Corrosão**. 3ª edição ed. Rio de Janeiro: LTC - Livros Técnicos e

Científicos Editora S.A., 1996dg.

[112] SILVA, Marcelo José Gomes da; CARDOSO, Jorge Luiz; CAVALCANTE, Alfredo Leão Silva Nunes; LIMA NETO, Pedro de; ABREU, Hamilton Ferreira Gomes de; BELO, Jardel de Souza. Avaliação e comparação da resistência à corrosão por pites do aço super austenítico al 6XN PLUSTM e de um aço inoxidável austenítico AISI 317L. *In:* CONGRESSO DA ABM – INTERNACIONAL, 67º.; ENCONTRO NACIONAL DE ESTUDANTES DE ENGENHARIA METALÚRGICA, DE MATERIAIS E DE MINAS - ENEMET, 12º., 31 jul. a 3 ago. 2012, Rio de Janeiro. **Anais ABM International Congress**; 12th ENEMET, Rio de Janeiro, v.67, n.67, p. 481-493, 2012dh.

[113] WANG, L. *et al.* Investigation of hydrophobic and anti-corrosive behavior of Cr-DLC film on stainless steel bipolar plate. **Diamond and Related Materials**, v. 129, n. June, p. 109352, 2022di.

[114] CRAIG, B. D. **Fundamental Aspects of Corrosion Films in Corrosion Science**. New York: Springer US, 1991dj. v. 21

[115] BATTELLE MEMORIAL INSTITUTE. **Handbook of Metallic Materials Properties Development and Standardization (MMPDS)-12**. Columbus: Battelle Memorial Institute, 2017dk.

[116] KRISHNA, D. S. R.; SUN, Y. Thermally oxidised rutile-TiO 2 coating on stainless steel for tribological properties and corrosion resistance enhancement. **Applied Surface Science**, v. 252, n. 4, p. 1107–1116, 2005dl.

[117] SHEN, G. X.; CHEN, Y. C.; LIN, C. J. Corrosion protection of 316 L stainless steel by a TiO2 nanoparticle coating prepared by sol-gel method. **Thin Solid Films**, v. 489, n. 1–2, p. 130–136, 2005dm.

[118] SHEN, G. X. *et al.* Study on a hydrophobic nano-TiO2 coating and its properties for corrosion protection of metals. **Electrochimica Acta**, v. 50, n. 25- 26 SPEC. ISS., p. 5083–5089, 2005dn.

[119] OHKO, Y. *et al.* Photoelectrochemical Anticorrosion and Self-Cleaning Effects of a TiO[sub 2] Coating for Type 304 Stainless Steel. **Journal of The Electrochemical Society**, v. 148, n. 1, p. B24, 2001do.

[120] MAHMOUD, M. G. *et al.* Influence of ultraviolet light irradiation on corrosion behavior of weathering steel with and without TiO2-coating in 3 mass% NaCl solution. **Scripta Materialia**, v. 53, n. 11, p. 1303–1308, 2005dp.

[121] GOU, C. *et al.* Probing the friction and wear behaviors of diamond-like carbon film in HCl and H2SO4 media. **Materials Research Express**, v. 6, n. 10, p. 0–14, 2019dq.

[122] NAGAI, T. *et al.* Anticorrosion of DLC coating in acid solutions. **Applied Surface Science**, v. 552, n. March, p. 149373, 2021dr.

[123] SENE, A. C. *et al.* Tribocorrosion Susceptibility and Cell Viability Study of 316L Stainless Steel and Ti6Al4V Titanium Alloy with and without DLC Coatings. **Coatings**, v. 13, n. 9, p. 1549, 4 set. 2023ds.

[124] CAZALINI, E. M. *et al.* Antimicrobial and anti-biofilm properties of polypropylene meshes coated with metal-containing DLC thin films. **Journal of Materials Science: Materials in Medicine**, v. 28, n. 6, 2017dt.

[125] PAUL, R. *et al.* Hydrophobicity in DLC films prepared by electrodeposition technique. **Applied Surface Science**, v. 255, n. 5 PART 1, p. 1705–1711, 2008du.

[126] FONTAINE, J.; DONNET, C.; ERDEMIR, A. Fundamentals of the tribology of DLC coatings. **Tribology of Diamond-Like Carbon Films: Fundamentals and Applications**, n. Dlc, p. 139–154, 2008dv.

[127] MACÁRIO, P. F. *et al.* Enhancing UV Radiation Resilience of DLC-Coated Stainless Steel with TiO2: A Dual-Layer Approach. **Coatings**, v. 14, n. 6, p. 777, 20 jun. 2024dw.

[128] IRESTAL GROUP. **Fichas Técnicas do Aço Inoxidável**. Barcelona: Irestal Group, 2024. Disponível em: http://data.irestal.com/files/files/2012030204152715829.pdf. Acesso em: 5 dez. 2022dx.

[129] MACÁRIO, P. F. *et al.* Corrosion behavior of Al2024-T3, Al5052-H32, and Al6061-T6 aluminum alloys coated with DLC films in aviation fuel medium, Jet A-1 and AVGAS 100LL. **Materials and Corrosion**, v. 70, n. 12, p. 2278–2291, 2019dy.

[130] GUO, D. *et al.* Corrosion Properties of DLC Film in Weak Acid and Alkali Solutions. **Coatings**, v. 12, n. 11, 2022dz.

[131] ZAVALEYEV, V. *et al.* Effect of substrate bias on the properties of DLC films created using a combined vacuum arc. **Bulletin of Materials Science**, v. 44, n. 3, 2021ea.

[132] ZHANG, C. Z. *et al.* Adhesion enhancement of diamond-like carbon thin films on Ti alloys by incorporation of nanodiamond particles. **Thin Solid Films**, v. 528, p. 111–115, 2013eb.

[133] SCHWAN, J. *et al.* Raman spectroscopy on amorphous carbon films. **Journal of Applied Physics**, v. 80, n. 1, p. 440–447, 1996ec.

[134] MARCIANO, F. R. *et al.* Oxygen plasma etching of silver-incorporated diamond-like carbon films. **Thin Solid Films**, v. 517, n. 19, p. 5739–5742, 2009ed.

[135] UNICAMP. **Contact Profilometer picture**. CAmpinas: IFGW, 2024. Disponível em: https://portal.ifi.unicamp.br/servicos/laboratorio-multiusuarios-lamult/perfilometro-rugosimetro-dektak-150-veeco. Acesso em: 30 jun. 2024ee.

[136] BIRD, J. **Newnes Engineering Science Pocket Book**. [s.l.] Routledge, 2012ef.

[137] SVEEN, S. *et al.* Scratch adhesion characteristics of PVD TiAlN deposited on high speed steel, cemented carbide and PCBN substrates. **Wear**, v. 308, n. 1–2, p. 133–141, 2013eg.

[138] ASTM STANDARD. **ASTM A380/A380M-17 - Standard Practice for Cleaning, Descaling, and Passivation of Stainless Steel Parts, Equipment, and Systems**. West Conshohocken: ASTM International, 2017eh.

[139] ASTM-INTERNATIONAL. **ASTM-G154 -Standard Practice for Operating Fluorescent Light Apparatus for UV Exposure of Nonmetallic Materials**. West Conshohocken: ASM International, 2000ei.

[140] Q-LAB. **QUV TESTE DE INTEMPERISMO ACELERADO**. [S.l] Q-LAB, 2024. Disponível em: https://www.q-lab.com/pt-br/products/quv-weathering-tester/quv. Acesso em: 30 ago. 2024ej.

[141] OUYANG, Y. *et al.* Raman study on single-walled carbon nanotubes and multi-walled carbon nanotubes with different laser excitation energies. **Physica E: Low-Dimensional Systems and Nanostructures**, v. 40, n. 7, p. 2386–2389, 2008ek.

[142] GRILL, A. Diamond-like carbon: state of the art**. Diamond and Related Materials**, v. 8, n. 2-5, p. 428-434, 1999el.

[143] CAPOTE, G.; SILVA, G. F.; TRAVA-AIROLDI, V. J. Effect of hexane precursor diluted with argon on the adherent diamond-like properties of carbon films on steel surfaces. **Thin Solid Films**, v. 589, p. 286–291, 2015em.

[144] RAO, X. *et al.* Tuning C–C sp2/sp3 ratio of DLC films in FCVA system for biomedical application. **Bioactive Materials**, v. 5, n. 2, p. 192–200, 2020en.

[145] AOBO WEI GUOZHENG MA, G. L. Z. L. C. H. H. Z. W. G. Z. X.; HAIDOU, W. Effect of space UV irradiation on the mechanical and tribological properties of Cr and B doped hydrogen-containing diamond-like films. **Fullerenes, Nanotubes and Carbon Nanostructures**, v. 31, n. 6, p. 513–522, 2023eo.

[146] STASZUK, M. Application of PVD and ALD methods for surface treatment of Al-Si-Cu alloys. **Solid State Phenomena**, v. 293, p. 97–109, 2019ep.

[147] CHIAPPIM, W. *et al.* Effect of Process Temperature and Reaction Cycle Number on Atomic Layer Deposition of TiO2 Thin Films Using TiCl4 and H2O Precursors: Correlation Between Material Properties and Process Environment. **Brazilian Journal of Physics**, v. 46, n. 1, p. 56–69, 2016eq.

[148] AARIK, L. *et al.* Atomic layer deposition of TiO2 from TiCl4 and O 3. **Thin Solid Films**, v. 542, p. 100–107, 2013er.

[149] WADULLAH, H. M.; AJEEL, S. A.; ABBASS, M. K. Synthesis and Characterization of Nanocoatings Thin films by Atomic Layer Deposition for Medical Applications. **IOP Conference Series: Materials Science and Engineering**, v. 518, n. 3, p. 0–8, 2019es.

[150] ABAS, M. *et al.* Analyzing Surface Roughness Variations in Material Extrusion Additive Manufacturing of Nylon Carbon Fiber Composites. **Polymers**, v. 15, n. 17, 2023et.

[151] KADHIM, H. K.; ALYOUNIS, M. Effect of surface roughness on the interface behavior of clayey soils. **Open Engineering**, v. 14, n. 1, 2024eu.

[152] LIGOT, J.; BENAYOUN, S.; HANTZPERGUE, J. J. **A**nalysis of cracking induced by scratching of tungsten coatings on polyimide substrate**. Wear**, v. 243, n. 1-2, p. 85-91, 2000ev.

[153] BURNETT, P. J.; RICKERBY, D. S. The relationship between hardness and scratch adhesion. **Thin Solid Films**, v. 154, n. 1–2, p. 403–416, nov. 1987ew.

[154] FANG, T. H.; CHANG, W. J. Nanomechanical characterization of amorphous hydrogenated carbon thin films. **Applied Surface Science**, v. 252, n. 18, p. 6243–6248, 2006ex.

[155] SAVVIDES, N.; BELL, T. J. Microhardness and Young's modulus of diamond and

diamondlike carbon films. **Journal of Applied Physics**, v. 72, n. 7, p. 2791–2796, 1992ey.

[156] BEC, S.; TONCK, A.; FONTAINE, J. Nanoindentation and nanofriction on DLC films. **Philosophical Magazine**, v. 86, n. 33- 35 SPEC. ISSUE, p. 5465–5476, 2006ez.

[157] BEWILOGUA, K.; HOFMANN, D. History of diamond-like carbon films - From first experiments to worldwide applications. **Surface and Coatings Technology**, v. 242, p. 214–225, 2014fa.

[158] PAULA, L. O. *et al.* Tribo-Corrosion and Corrosion Behaviour of Titanium Alloys with and Without DLC Films Immersed in Synthetic Urine. **Journal of Bio- and Tribo-Corrosion**, v. 4, n. 3, p. 51, 21 set. 2018fb.

[159] THORWARTH, G. *et al.* Tribological behavior of DLC-coated articulating joint implants. **Acta Biomaterialia**, v. 6, n. 6, p. 2335–2341, jun. 2010fc.

[160] HAUERT, R. *et al.* Analysis of the in-vivo failure of the adhesive interlayer for a DLC coated articulating metatarsophalangeal joint. **Diamond and Related Materials**, v. 25, p. 34–39, 2012fd.